SIMULATED FLOW ANALYSIS OF GEOMETRIC EFFECTS ON DIRECT CONTACT CONDENSATION

by

Christian C. Thorpe

A thesis submitted in partial fulfillment of

the requirements for the degree of

Master of Science

(Mechanical Engineering)

at the

UNIVERSITY OF WISCONSIN-MADISON

2023

Table of Contents

Acknowledgments

I would like to dedicate this thesis to Kristofer Dressler. He was the one of the best teachers I ever had at UW Madison and is the reason I continued to study in the amazing UW master's program. He always pushed me every week to be a better and better engineer with my social skills and how I view the problems before me. He taught me more about being an engineer than any book or video could. He always showed enthusiasm towards his students asking questions to which he would usually tell me he's been to a lot of rock concerts and that I need to speak up. I am forever grateful for the guidance and time he has given me.

I would like to thank my three advisors Greg Nellis, Allison Mahvi, and Arganthael Berson. They have always been a great help giving me direction during our weekly meetings and pushing me to accomplish more and more. Their knowledge and experience has been invaluable to what I have learned and explored with my research. Without them I would not have been able to put this work together and am thankful for all their time and effort.

In addition, I would like show my gratitude Jim Zaiser, Mark Kliewer, and Shawn Berg from Hydro-Thermal Corp for providing support and encouragement for the research I have done at UW Madison. I could not have accomplished what I have with studying steam injection without their continued enthusiasm towards the work I and the previous grad students have done. Our Biweekly meetings were always great at helping me brainstorm my next steps and appreciate the time you all gave me.

As well I want to acknowledge all the help Zach Alden has provided me by teaching me everything I know about running the steam injection loop. You were a great mentor for my time

as an undergrad working in the lab and I have you to thank for graduate student I became. Without the foundation you helped create I would not have been able to accomplish all the work I have in the Lab. I hope that I will be able to pass on the work you have done onto the next generation of steam lab graduate and undergraduate students.

I give thanks to all my undergrads including Madeline Morrell, Lauren Hunter, and Peter Connell. I could not have obtained as much data during my few years in the MFVAL lab without their continued support and help maintaining and testing the loop. They are all great and shining future engineers and I am glad to have been part of their journey.

I want to acknowledge Erik Tillman for all the help taking X ray scans of my nozzles. I appreciate all the time you gave me and how helpful you were with getting the images I needed, and I wouldn't have been able to make as strong of a thesis without your help.

I want to show my appreciation to all my friends and family for all the support you have provided me to help finish this thesis and all the previous work I have done. Finally, I would like to thank my cat Jinx for always waiting by the door for me after a long day in the lab.

1 Introduction

Direct contact condensation (DCC) is a method of heat transfer that relies on the condensation of a vapor injected into a liquid process fluid. An example of this process is injecting steam with a sparger into a water tank to bring the water tank up to the correct temperature. The process is much more efficient than traditional heat exchangers due to direct contact between the two phases. The thermal resistance between the two is negligible compared to the walls of a heat exchanger. In addition to the increase in efficiency the process also can reduce the amount of equipment required in heating a product and reduce any waste steam that may normally be ejected[1]. While DCC is a great solution to simplify a thermodynamic system given certain conditions it will produce oscillations that cause unnecessary loads on the piping structure, and anything attached. In addition, these oscillations result in noise that can exceed OSHA limits and harm workers. These destructive frequencies result from plume oscillations at the gas-liquid interface.

The research described in this thesis is a continuation of the work started by Vineet Barot, Max Brennan, and Zach Alden [2]–[4]. Much of the previous research has focused on categorizing the plume behavior with stability regimes that help encapsulate the types of oscillations that occur during operation. This research focuses on the effect of nozzle diameter, type and length. In addition, this work explores the use of CFD of the vapor in the nozzle to understand plume stability In this thesis, the effect of nozzle geometry on the stability of a crossflow DCC process is evaluated. Steam is injected into a laminar stream of water, and the stability characteristics were measured and quantified. Several nozzle designs were fabricated, inspected, and experimentally evaluated. The geometric features that were adjusted include the area ratio, defined in this thesis

as the ratio of the areas at the exit and the throat of the nozzle, as well as the type of nozzle (e.g., straight, converging or diverging). A CFD model of the vapor flow within each of the tested nozzles was used to understand how the nozzle geometry affects the velocity distribution at the nozzle exit to correlate features of this exit flow with plume stability. Each nozzle was tested over a range of pressure ratios and water temperatures. The results of these tests show that the stability of DCC tends to improve if the vapor flow at the outlet of the nozzle is supersonic. Using the results provided here, a more stable nozzle can be designed for a range of conditions and fluids without resorting to complex simulations that involve multiple phases and free surfaces by instead focusing on developing a nozzle geometry that achieves the appropriate vapor exit condition.

2 Background

Direct contact condensation injectors have been in use since the 1860's with the invention of Giffards patented steam boiler injector[5]. Since then the method has been used in oil, food, paper and other industries as a way of reducing complexity and waste products. One of the earliest investigations into understanding this process was done in a paper by P. J. Kerney et al in 1972[6]. Since then, DCC has been the focus of many research papers with a focus on capturing the penetration characteristics, heat transfer coefficients and the pressure oscillations produced during operation. The following section contains a literature review describing the past work most relevant to this thesis. The literature review focuses on prior work on the stability of DCC [7-23], the effect of nozzle geometry [13-15,24-27] and the progress made to use CFD to understand DCC[28-37].

2.1 Direct Contact Condensation Stability

The plume in DCC creates thermal and pressure oscillations that cause structural damage and pose a noise hazard in application[7], [8]. The conditions of both the liquid and gas phases affect the strength and frequency of the oscillations experienced in DCC. Previous studies have categorized the behavior of these plume oscillations into different regimes including chugging, bubbling, and jetting regimes with jetting being split into conical, divergent, and ellipsoidal shapes[9]. Alden et al [10] reported that there was no consistent regime naming. For their study they focused on four main regimes:

1) Unstable, where there is a consistent formation and detachment of bubbles

2) Transition regime, where the plume it is switching between unstable and condensation oscillation regimes
3) Condensation oscillation regime, where there is a slight oscillation in the plumes shape but maintains a plume, and
4) Stable, where the plume maintains the same shape with little to no variation.

Under extreme conditions chugging was added to the regime map for unstable plumes that struggle to maintain a steady flow of steam. This thesis will use this naming convention when describing plume stability [10].

Many previous studies have attempted to categorize the steam plume regimes with regime maps that use different conditions experienced during DCC [11]–[18]. Early work on these regime maps used vapor mass flux and liquid temperature to create the bounds between each of the regimes[11], [19]. One of these early regime maps [19] can be seen in Figure 1.

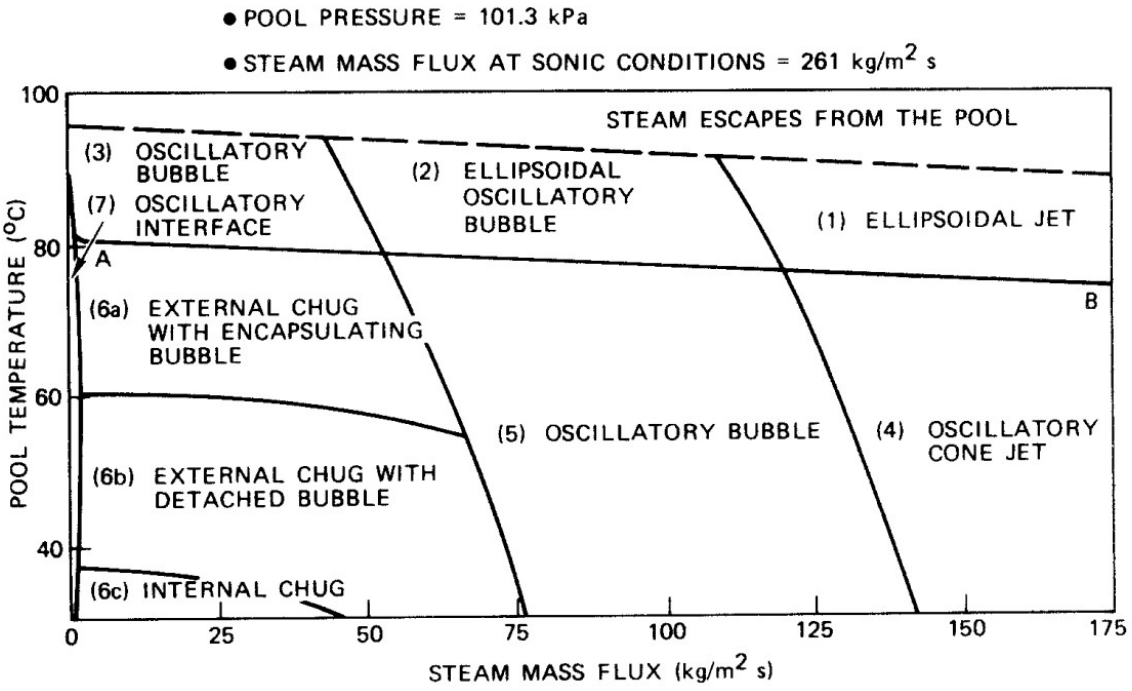

Figure 1: Early Regime Map for DCC into a pool[19]

As illustrated in Figure 1, more stable plumes occur at lower liquid temperatures where there is a higher condensation potential as well as a higher gas mass flux which helps to alleviate instabilities.

Research studies have also looked to apply and adapt these regimes to each of the DCC configurations ranging from sparging to cross flow injection. Xu et al. [20] studied how parallel flow affected a steam plume's regime. They were able to create a 3D regime map for this study by introducing the Reynolds number of the water into the traditional mass flux versus temperature regime maps seen previously in Figure 1. Xu et al. created stability plume regime maps using the Mach number of the steam flow. This work is relevant to how this thesis approaches its comparison between the CFD and experimental results of nozzles as the shock location is of great interest for comparing the different nozzles.

Additionally, there have been some attempts at actively controlling these regimes. For example, Boziuk [21] studied the effect of introducing acoustic waves onto a steam plume in a tank. They found it did not affect the velocity of the bubble but "roughed" it up as it condensed. In addition to shape, they also studied the effect of acoustics on the heat transfer coefficients of the DCC process and found that the time averaged results were 255% increased by the presence of the actuation, which was primarily the result on increasing the steam-water surface area. Another interesting study looked at using obstructions to improve the DCC process [8]. The obstructions in this study created a porous structure inside the test section. They found that this approached weakened thermal oscillations in their test section but that it increased the overall oscillations experienced downstream of the test section. For pressure, the porous structures were able to weaken the amplitude of the pressure oscillations and decrease the RMS values calculated during their experiments. Another approach studied by Li et al injected air into a stagnant pool of water and studied the effect it had on DCC as it had not previously been studied [22]. They found that increasing air mass fractions lead to more intense pressure oscillations. They also found the point at which the air mass fraction became critical was dependent on the steam mass velocity exiting the nozzle. Additionally, they formulated correlations between the pressure intensity for sparging using the Reynolds, Jacobs, and Mach numbers. These novel approaches both offer interesting insights into the DCC process but don't tackle how to change the injector for more traditional heaters.

2.2 Effect of Nozzle Geometry

Most previous work on DCC either studies a single nozzle or variations of a simple straight nozzle without focusing on features at the inlet or outlet [13]–[15]. One of the earliest

study on nozzle geometry studied the effect of the length to diameter (LD) ratio on the plumes penetration characteristics but did not evaluate the impact the LD had on the stability or oscillations produced during DCC [6]. Quddus et al. [16] studied the stability and shape of the plume in a sparging process. In this study it was found that having a bevel in the nozzle geometry caused the plumes axis of symmetry to shift when injected into a pool. Additionally, their study demonstrated how increasing this beveled angle results in a more unstable plume. The geometry is mapped out by Petrovic de With et al. [23] where the diameter was used as a third axis to mapping out the stability of a plume in a stagnant pool using data from previous research papers. The resulting regime maps is shown in Figure 2.

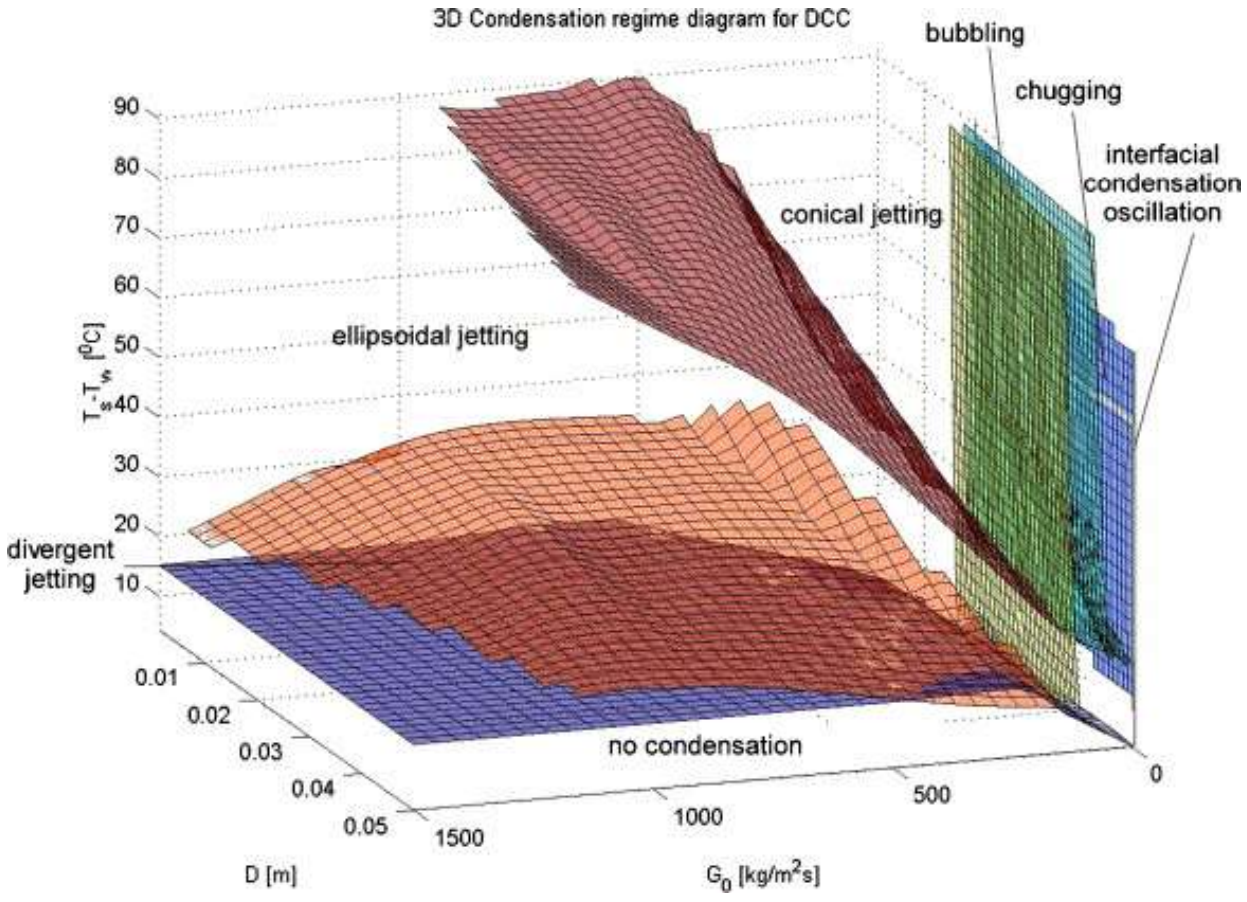

Figure 2: 3D Condensation Regime Map[9]

Although the majority of work in DCC focuses on a single nozzle, there has been some work looking at interactions of multiple plumes. Lu et al. [17] studied how two plumes interact with each other when injected into a pool. The study demonstrates how increasing the plume length at high temperatures would cause adjacent plumes to connect but does not affect the stability of the DCC process. A similar study from Zhao et al evaluated multi-nozzle steam injection with a focus on studying the differences between two and three nozzles as well as the effect of nozzle pitch [24]. They found that as the pitch of the nozzles increase, there is an increase in the dominant frequency and increasing hole numbers resulted in a decline in the dominant frequency. A more application based approach to multi nozzle designs can be found in a paper by Sangsom and Inprasit [25]*, which shows that* increasing the number of nozzles in a steam injection sterilizer will increase the sterilization temperature.

Another study that focuses on the effect of geometry on an application from Jimenez-Junca et al looks at how the changes to the foamability of milk[26]. Each nozzle focused on different methods of mixing air with steam so the nozzle geometry may not have the same impact as observed in this paper, but they found that each version had a significant impact on bubble formation. Also, this paper found that by having a higher steam pressure a more desirable frothing because of less bubbling in the steam plume which matches with the regime maps developed later in this paper. Another study by Wang et al compared a side ejecting nozzle to a orifice and pipe style injector[27]. They found that injecting steam from the side of a nozzle results in the smallest plume length and expansion ratio capable. They also found increasing the steam mass flow for a side hole nozzle will increase the instabilities experienced during condensation at higher pool temperatures.

2.3 CFD Studies

In addition to the experimental work described above, several authors have evaluated the DCC process using computational fluid dynamics (CFD). An attempt to understand the fundamentals of the interface was done in a paper from Y. Zhou and Y. Li [28] which placed a focus on determining what solution method can be used to solve the evaporation/condensation coefficients the best. They settled on using non-equilibrium molecular dynamics simulations to determine these coefficients by utilizing a two-boundary condition. Another such study from Gulawani et al. looked to validate the results of a multiphase flow simulation to video data looking at the height of the plume [29]. This paper was able to create correlations for the interfacial surface area that experiences condensation. The results from this study provide insights into the temperature distribution in the plume for different nozzle geometries that could not be obtained experimentally. As example of these results are shown in Figure 3.

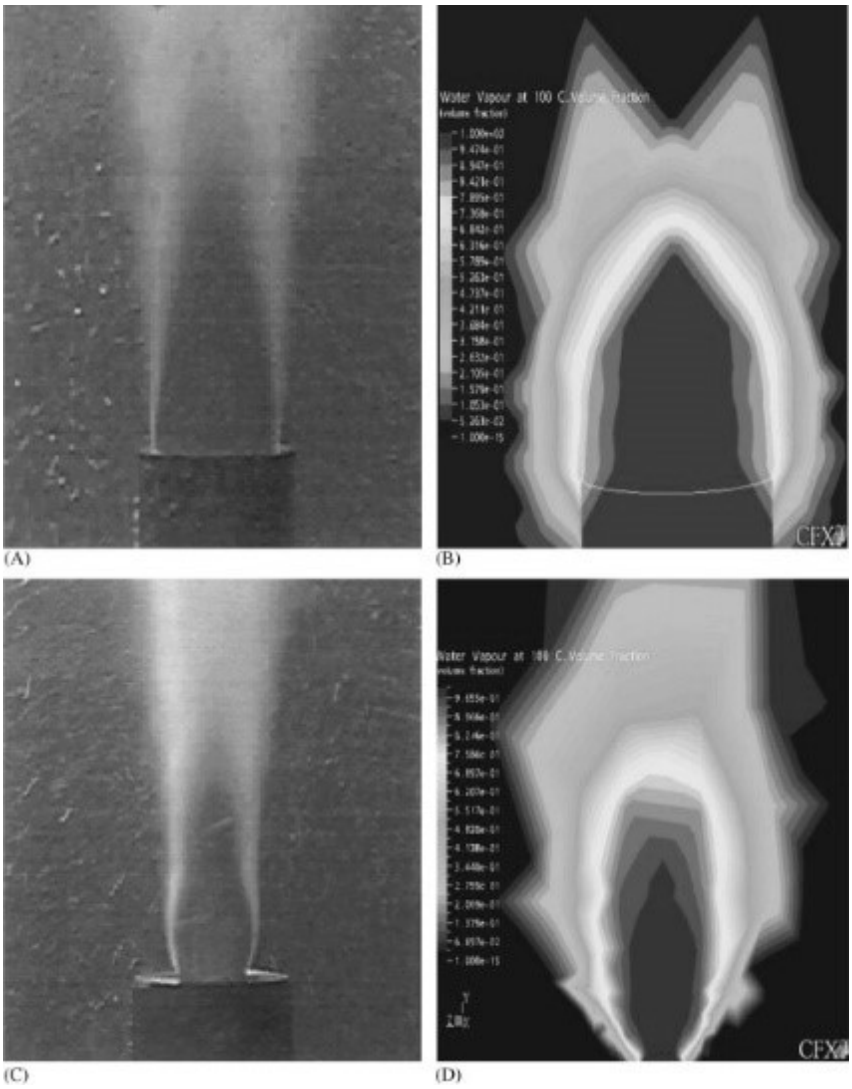

Figure 3: Different plume shapes compared to Gulawani et al. CFD results[1]

Another model developed by Li et al. used a volume of fluid technique to model the interfacial area and a large eddy simulation to measure turbulence[30]. This approach was able to illustrate the pressure and temperature distributions both spatially and temporally. The distributions demonstrated the oscillations experienced when under chugging and showed the separation of the plume in a simulated environment. Figure 4 is an example of the fluctuations studied in this paper.

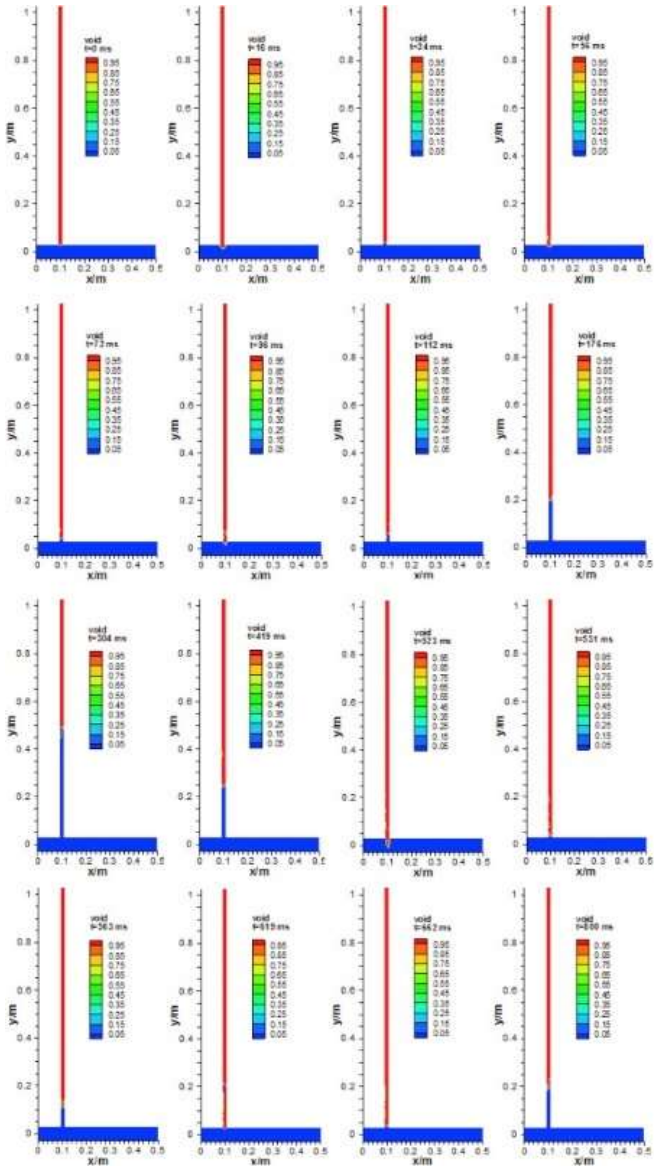

Figure 4: Steam plume variation with time [30]

Although commonly used, Gallego-Marcos *et al.* [31] found that using a VOF model cannot capture the steam flow characteristics from their experiments. Instead, they extended a version of the Effective Heat and Effective Momentum Source model to capture the turbulence production and dissipation that occurs when steam injection is sparged in a pool. Another model that focused on simulating a suppression pool from Patel et al. used a Eularian-Eularian

two fluid model with a Rayleigh-Taylor interface model and a k-ε model for turbulence[32]. Similarly, to the other experiments this model could determine the distributions of temperature and pressure as well as detailing the volume fraction of the steam water mixture at different points in the suppression pool. An example of the volume fraction and rates found in this paper is found in Figure 5.

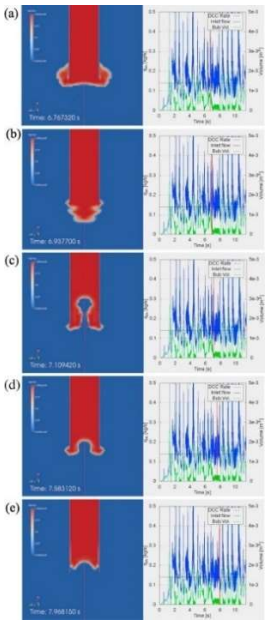

Figure 5: Instantaneous steam volume fraction, corresponding DCC rates and bubble volumes[32]

In contrast to the work described above, this thesis focuses on a more simplified single-phase model to allow for rapid simulation of the flow inside of different nozzle geometries and different conditions. Khan et al used a similar approach to study converging diverging nozzles [33]. Their research focused on using a 3D model to study the effect of using different angles of injection. Below are the results of changing the angle of injection on the void fraction in the subcooled water in Figure 6.

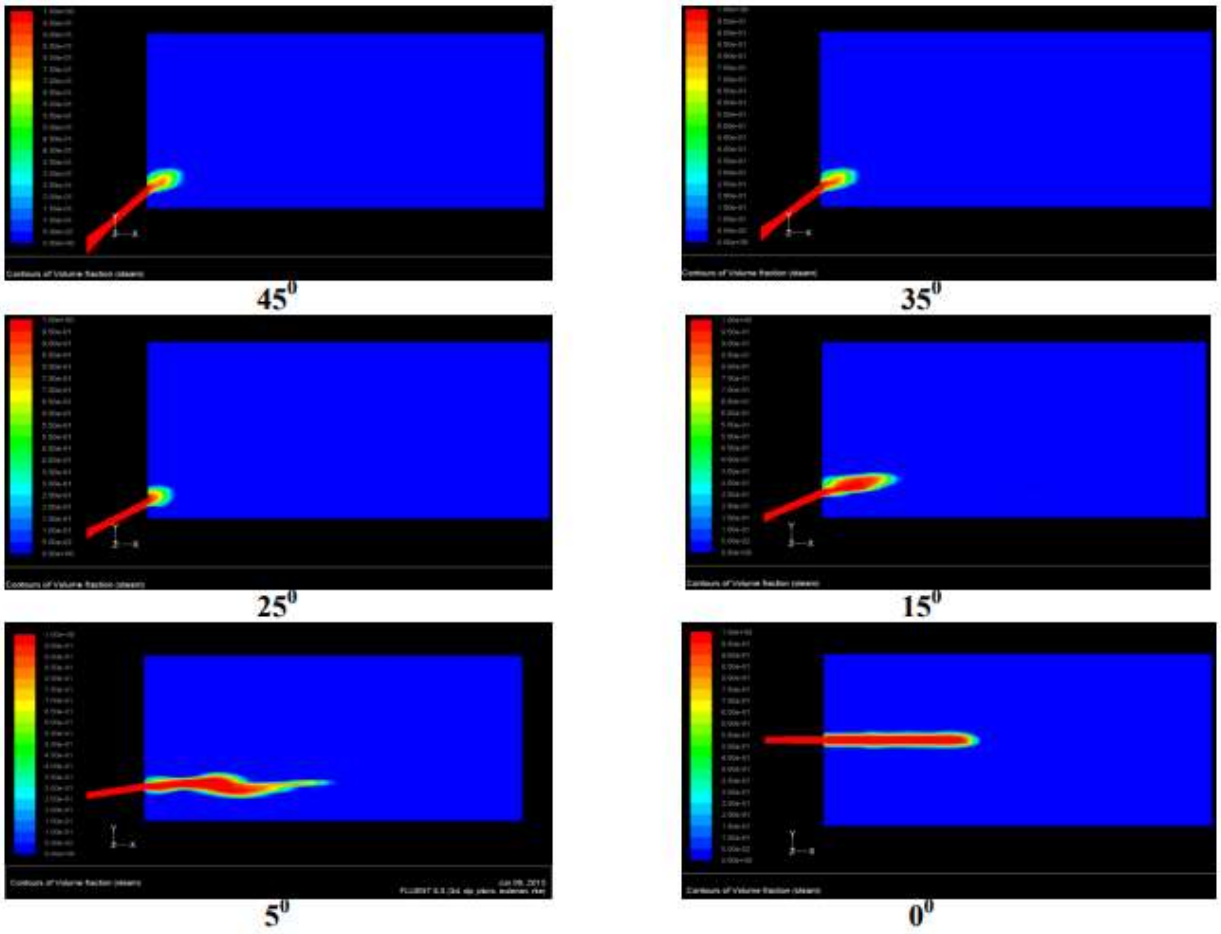

Figure 6: Qualitative void fraction of steam in the subcooled water region at different angles of injection[33]

In study by Jeon et al. [34] an axisymmetric approach is used to capture the movement of steam and water in a safety water injection tank and understand the turbulence and movement of the two phases. This approach uses a similar philosophy for geometry modeling as the one used in this thesis to model the flow of steam.

There are also examples of using CFD to help design applications. Like this thesis a study from Saraiva de Lira Araújo and Romero [35] aimed to use CFD to optimize the geometry of a steam injector but for reducing heat loss rather than controlling the regime of steam plume.

Another study by R. Gharibshahi et al. [36] looked to use CFD to optimize the steam injection process for better oil recovery using different nanoparticles in their model and experiment. Another example of CFD being used to aid in steam injection usage in oil production can be seen in a paper from Patureaux et al where it is used to help aid in the distribution of the catalyst with the usage of steam injection in their line[37].

2.4 Current Study

This thesis aims to fit into the previous literature by taking a finer look at the effect of nozzle geometry than previously explored. Previously there has not been an exploration into the effect of shock location on the stability of DCC where this work aims to fit into that gap. Additionally, the previous geometry studies looking at nozzle structures have never considered any defects or microfeatures that occur during manufacturing. This work emphasizes the importance of detailing those features in future literature so that a small burr won't lead to misleading data. Finally, this work seeks to demonstrate a simple and easy method of using CFD to validate or analyze DCC applications.

3.1 Experimental Setup:

This work is split into two main parts – an experimental evaluation of different nozzle geometries and a computational study of superheated steam through the nozzle. This section will describe the experimental methods used in this work, and the following section will describe the methods used to simulate the nozzle flow.

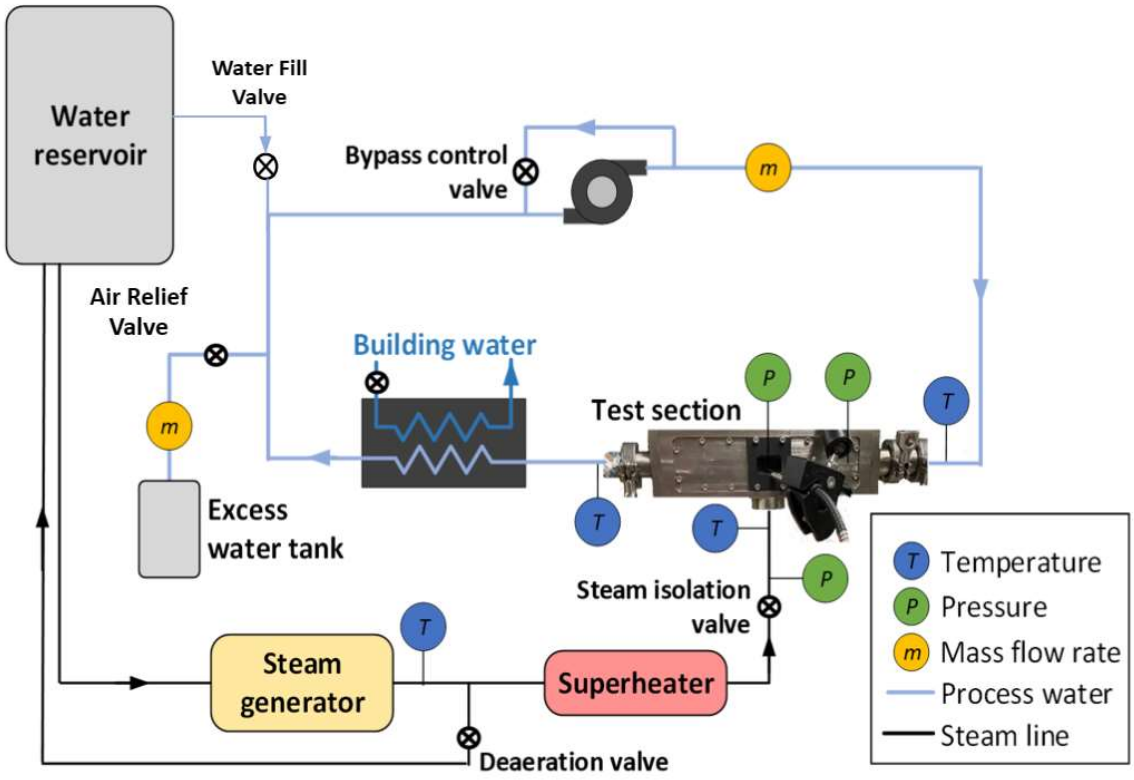

Figure 7: Schematic of experiment.

The test loop depicted in Figure 7 is split into two sections, each responsible for each of the two phases of the DCC process. These two sections meet at the test section, where a nozzle injects steam vertically into the process water. That steam flow is supplied by the water reservoir which feeds into the steam generator. The steam generator controls the pressure of the steam in the line by controlling the temperature of the steam exiting the generator. This

steam is then heated by heat tape in the superheater portion of the schematic to get up to a degree or more of superheat to prevent saturated steam. A ball valve controls the steam, allowing the injection process to start and stop quickly. Before the process, water is put into the water loop and heated to about 85C to help deaerate before testing. This heating is done by rerouting the steam line into the water reservoir, which is done by sparging steam into the water. The heated water is routed into the water loop until it is filled. Next, the pump is turned on to circulate the water to continue to aid in deaeration as the water rises to test pressure. The water pressure is set by using a bladder in the excess water tank. Following deaeration, the flow rate is set for test conditions by adjusting the bypass control valve. The temperature of the water line is controlled by the flow rate of cold water that goes through the heat exchanger during the injection. To capture data, there are temperature and pressure sensors for both flows before and after condensation. For the mass flow of steam, the excess water that travels to the overflow tank is measured and assumed to be fully condensed steam injected. At the same time, a volumetric flow meter is used to capture the water flow rate. To measure the plume a high-speed camera captures video using the window seen in Figure 1. Finally, a microphone is pointed at the test section to capture the noise level and frequency produced during the experiment.

3.1 Water Loop Control

Process water is circulated with a centrifugal pump (Bell & Gosset 90-4T, maximum flow rate of 75.7 L/min) and the flow rate is controlled by adjusting a ball valve in the recirculation loop.

Figure 8: Pump and Recirculation Loop

Next the water flows through the test section where it will be heated by the steam injector. After the test section the water flows to the heat exchanger where building water flows through the other side. The building water flow rate is controlled using a needle valve depicted in Figure 9.

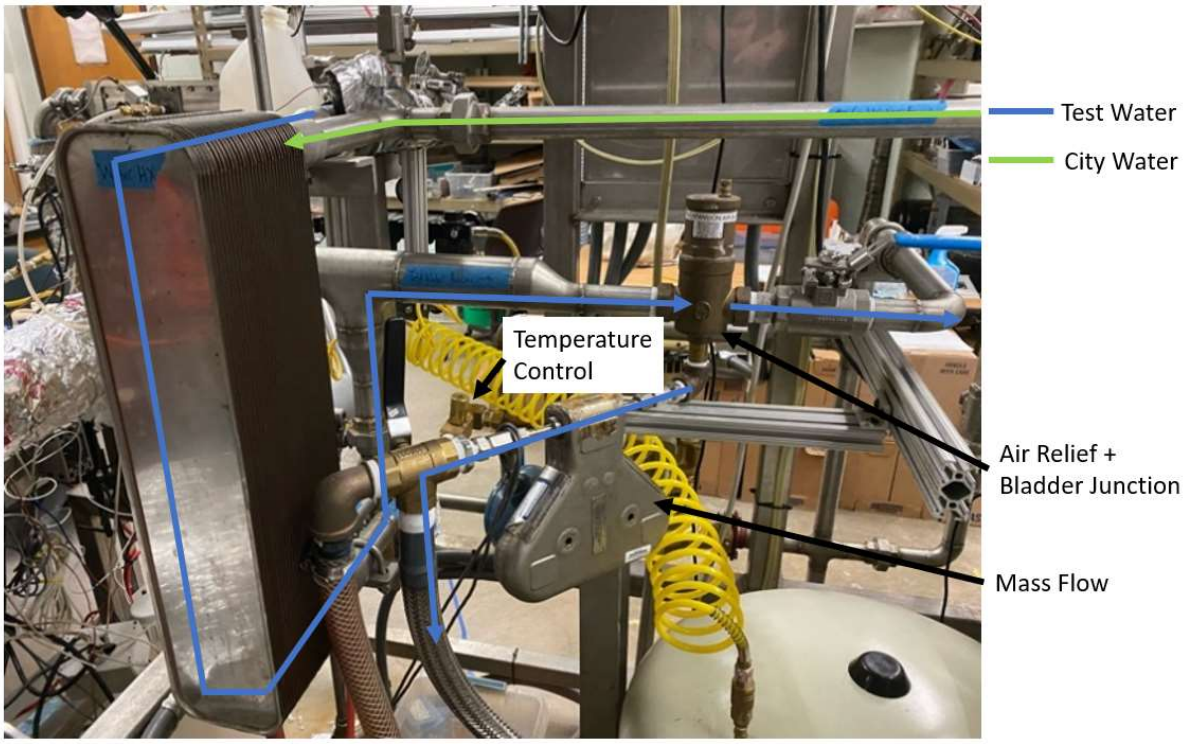

Figure 9: Heat Exchanger

The water then flows to a T junction where it either continues to the pump or flows to the bladder tank. Additionally, this T junction has an air bleed to help during the deaeration process of testing. In the bladder tank a bladder is pressurized by shop air which is controlled by the pressure regulator depicted below in Figure 10.

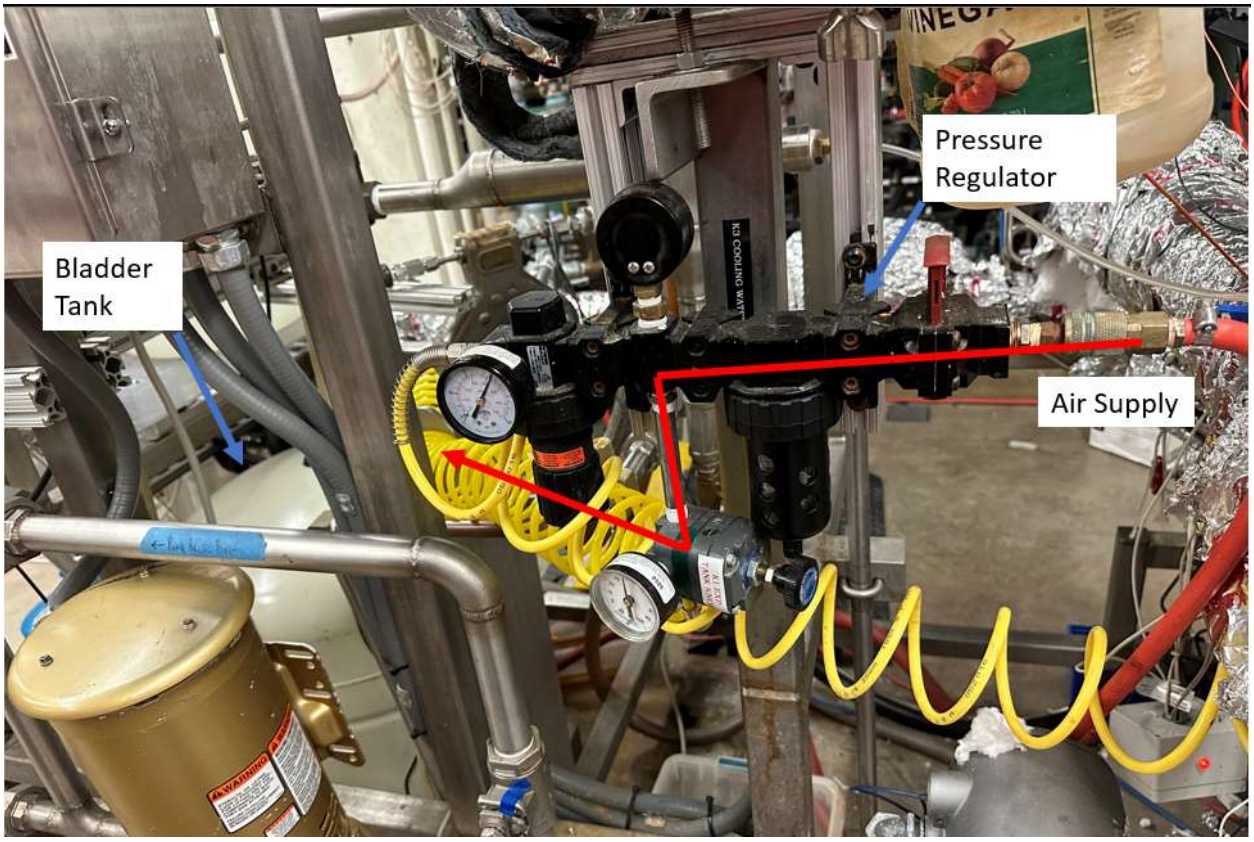

Figure 10: Bladder Tank and Pressure Controls

When the bladder is pressurized, it will keep the water pressure constant at the desired value for testing. Finally, the water returns to the pump where it continues to recirculate.

3.2 Steam Line Control

The steam line starts at the steam generator which is fed by the deaeration tank as seen below in Figure 11.

Figure 11: Steam Generator

The steam generator gets power supplied by the control box in Figure 11. The power supplied is regulated by a PID controller using a temperature probe at the top of the generator. The temperature is set to the desired saturation temperature for the steam pressure being tested. Additionally, a level switch at the top of the generator will activate the pump at the bottom of Figure 11 to supply more water to prevent starvation. As the steam leaves the generator, it crosses an emergency drain valve before reaching the cross junction, as seen below in Figure 12.

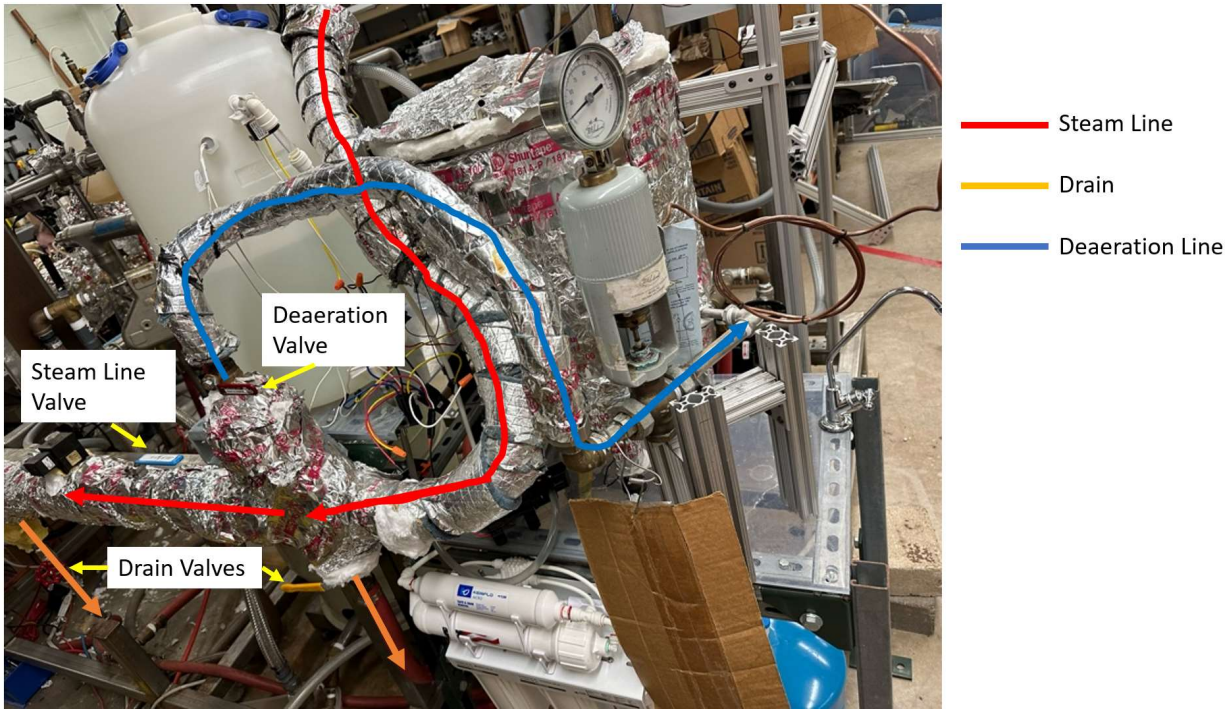

Figure 12: Steam Junction

Figure 12 shows how the steam from the generator is either sent to the test section, dearation tank or the drain depending on the need. During preparation the deaeration valve is opened to allow for sparging into the deaeration tank. When testing the only valve open is the steam valve line. Finally shutdown all but the drain valves are closed. From this junction the steam then proceeds to the superheater section of the steam line. An uninsulated example of the superheater section can be seen below in Figure 13.

Figure 13: Heat Tape used to Superheat Steam

After passing through the superheated section of the steam line it goes to T junction where it is either drained using the last drain valve in the line or is let into the test section via a ball valve as depicted in Figure 14.

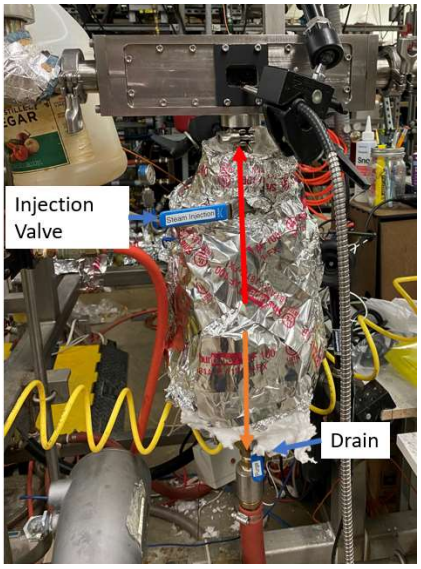

Figure 14: Steam Line connected to Test Section

In addition to draining steam during shut down the drain valve in Figure 14 is used to help remove any condensation that has formed or been left over from previous experiments inside the steam line.

3.3 Test Section

A test section was fabricated to evaluate steam injection into a process water stream in cross flow. A diagram of the test section is shown below in Figure 15.

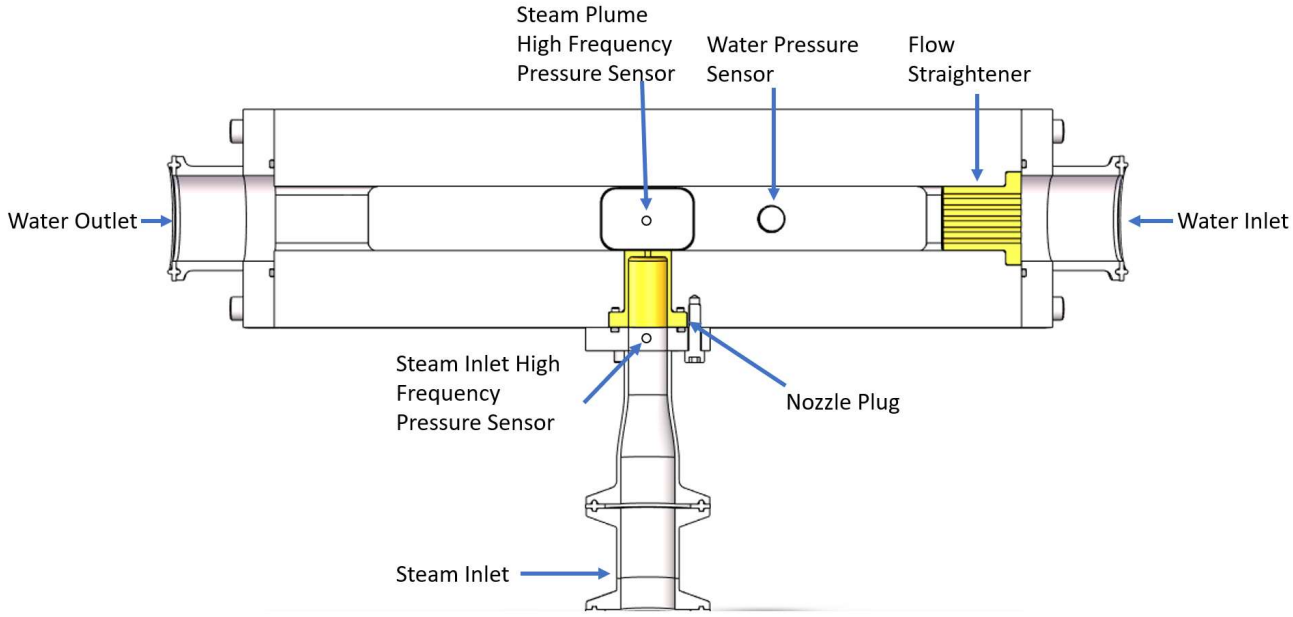

Figure 15: Cross section of Test Section

The test section consists of two inlets and one outlet. The water inlet contains a flow straightener to maintain a laminar flow field as steam and water contact. The other inlet has a reducer adapter which then contains a high-speed pressure sensor (Kulite XTME-190LM-35BARA) right below the nozzle. Above this pressure sensor is a cavity for the nozzle plugs, which can be easily replaced to allow for multiple nozzle geometries to be tested with this

setup. In the middle of the test section is another kulite pressure sensor which collects pressure data near the tip of the steam plume. Before the flow contacts the steam it first passes by a pressure sensor where the process water pressure is taken. Finally, the mixture flows out of the outlet where it will then flow past the outlet temperature sensor and into the heat exchanger.

3.6 Instrumentation:

To collect the process conditions an array of pressure, temperature, and flow rate sensors are used. All of the process conditions are recorded at 1000 Hz to capture the fluctuations observed taking only a few milliseconds. The process water inlet pressure was measured before it reaches the steam plume using a SSI Technologies P51-100-G pressure sensor, and the steam pressure is similarly taken upstream of the injection site using a Baumer pressor sensor (Figure 16).

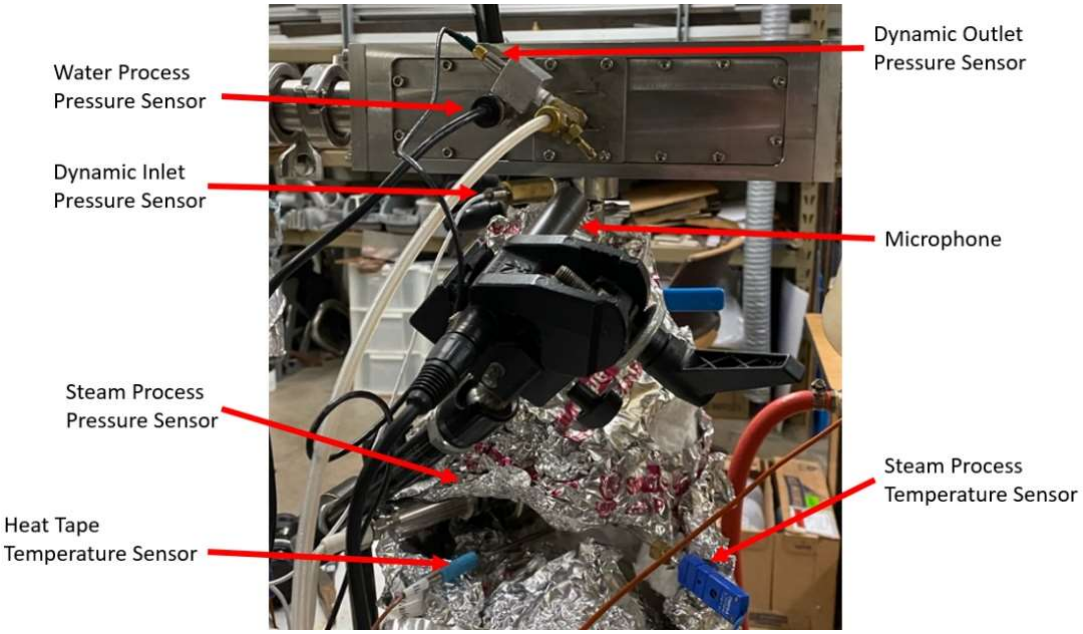

Figure 16: Backside of test section

The water temperature is measured at the test section inlet and outlet (shown in Figure 17) using two thermocouples (Type-E, ±1.7°C) that had previously been calibrated by Max Brennan[4].

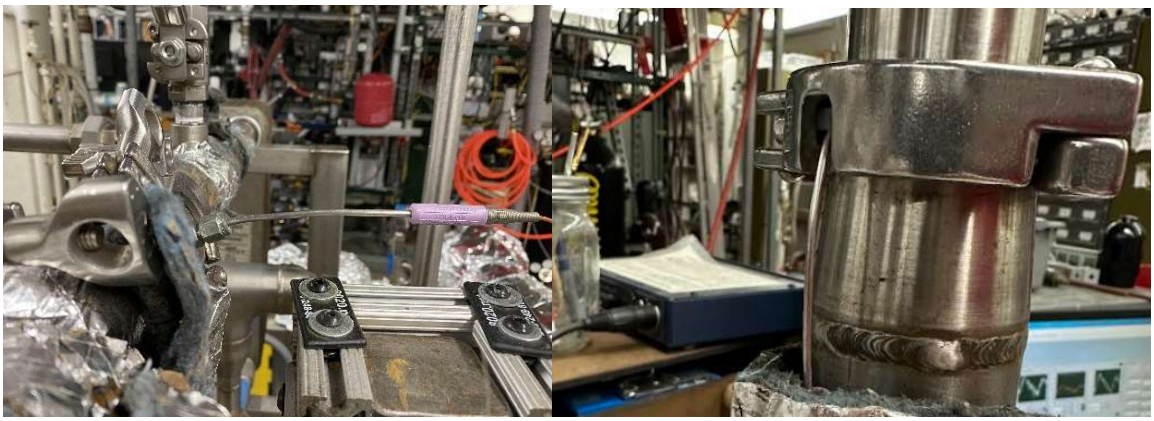

Figure 17: Thermocouple mounting locations (Outlet Temp left and Inlet Temp Right)

Next the water flow of the system is measured by a Toshiba GF630 electromagnetic flow meter and the mass flow of steam is measured with the excess water flow going into the bladder tank using a Coriolis mass flow meter (Emerson CMF010M) which had previously been validated in Zach Alden's work[10]. Both of these sensors are shown below in Figure 18.

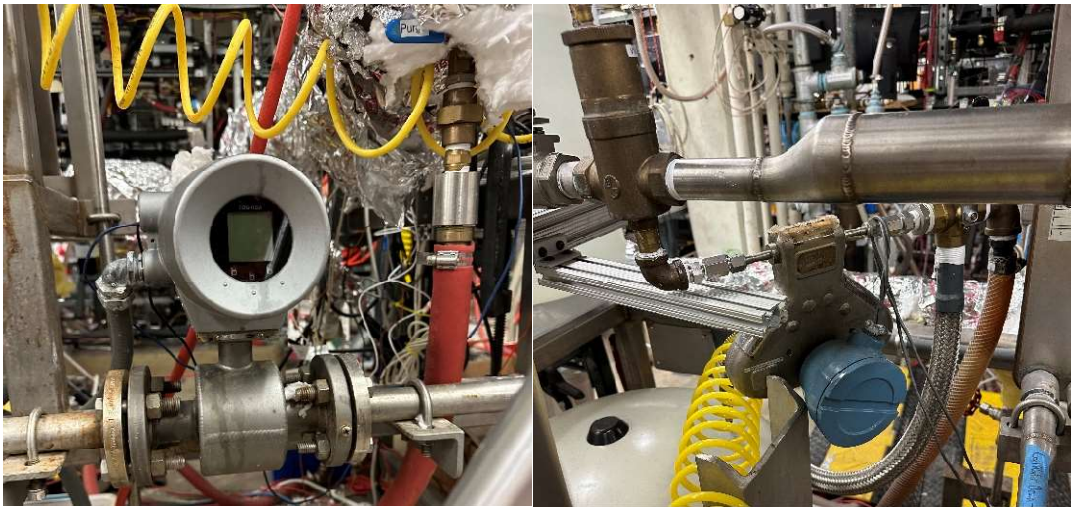

Figure 18: Flow Sensors (Water Flow Left and Steam Flow Right)

Dynamic data is taken with pressure sensors, a high-speed camera, and a microphone. To capture high speed pressure the previously discussed pressure sensors take data at high 40 kHz for 10 seconds. Video data is taken for 1 second at 80 kHz with the camera trigger is recorded so that the start of the video recording can be matched to the high frequency pressure data as well as any other process conditions. A Phantom V311 high speed camera takes images at 128x200 pixels (FOV ≈ 0.6”) was placed in front of the viewing window to capture these videos. To reduce any reflections from the fiber optic light and allow for clear contrast between the steam and water, the plate adjacent to the viewing window is painted matte black. The software PCC is used to save high speed video data to the computer. The orientation and setup of the fiber optic light and camera are shown in Figure 19.

Figure 19: Camera Set up for recording.

A Symetrix 302 dual preamplifier (20 kHz) is used with a microphone (AT3527) to record audio data. The microphone is mounted 1 meter behind the test section (shown in Figure 16). In addition to the microphone a decibel mete(Reed R8080) is mounted a meter away and pointed at the test section to capture standardized decibel readings. All the sensors are wired to a data acquisition (DAQ) system (Texas Instrument cDAQ-9178) which sends the data to the computer to be processed by LabVIEW. The DAQ setup is pictured in Figure 20.

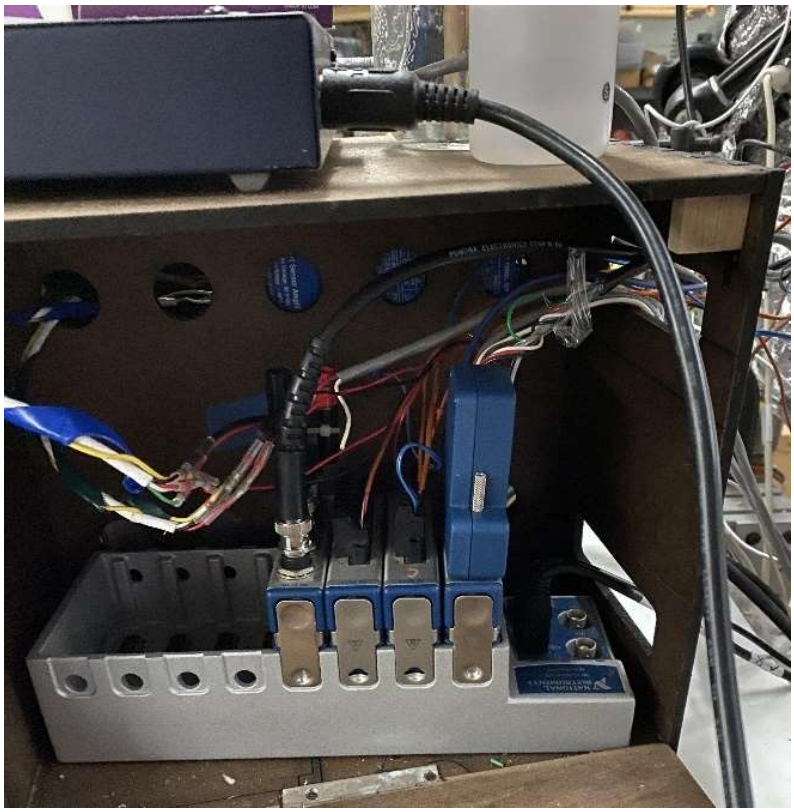

Figure 20: DAQ Setup

The DAQ contains 4 modules. The first module handles the trigger data from all of the dynamic sensors described above. The middle two modules handle the temperature sensors and the module on the right handles all the remaining sensors like the water flow meter. All the sensors used in this test apparatus are listed below in Table 1.

Table 1: Instrumentation and Uncertainty

Sensor	**Range**	**Uncertainty**	**Application**
SSI Technologies P51-100-G sensor	0-0.69 Mpa	±1.0% FS	Collect Process Water pressure
Type-E thermocouple	-200 - 900°C	±1.7°C (0.5%)	Collect water temperature post DCC
Kulite XTME-190LM-35BARA	0-3.5 Mpa	±1.0% FS	Collect Dynamic Pressure Data
302 Dual Microphone Preamplifier	20hz-20khz, Max 14dbv		Collect Audio data near DCC
Phantom V311	128x200 at 80,000 Frames	Exposure Time: 11.814 µs	Collects Visual Data of the Steam plume
Baumer pressure sensor	0-1.586 Mpa	±0.25% FS	Collect Steam Pressure
Emerson CMF010M Coriolis mass flow meter	125 barg	±0.10%	Measure Steam Mass flow
Audio Technica AT3527	30-20,000 Hz		Collect Audio Data
REED R8080	30 to 130dB (0.1 resolution)	±1.4dB	Measures Decibel Level

3.5 Testing Procedure

The first step of testing is to take the ambient conditions without any steam or water in the water loop, steam line and test section. Ambient conditions are taken to calibrate the

pressure and temperature sensors for a new 0 psig before any water or steam is in the loop. This is done using Labview with a program previously developed by Zach Alden for his research using the same test section. An example of the Labview program used to save test data can be found below in Figure 21.

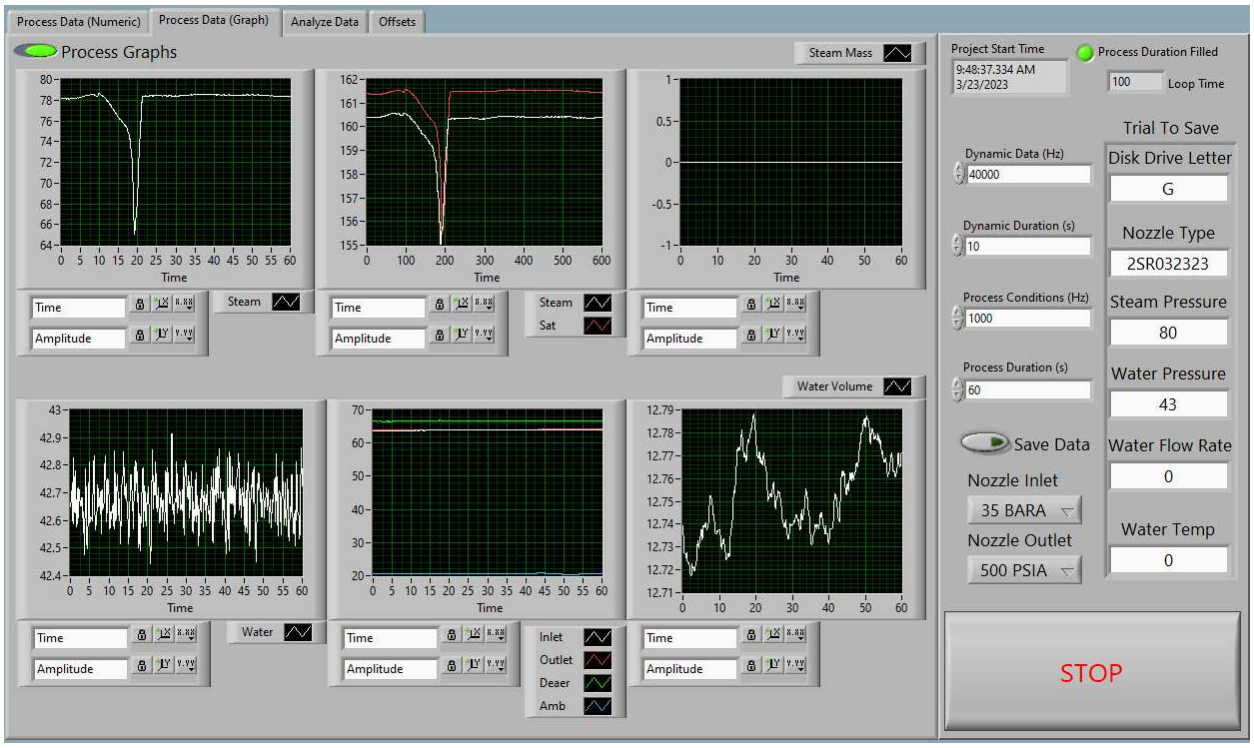

Figure 21: Ambient Condition Controls In LabVIEW

The next step is to prepare the process water through deaeration to help improve the quality of the video and sensor data. The deaeration process starts by running building water through a reverse osmosis filtration system to remove any particulate and passively deaerate the water before it goes into the reserve tank. In the reservoir tank the water is pumped into the deaeration tank if it is not filled. The next step in the deaeration process is sparging steam at 20 psig into the deaeration tank using the valves depicted in Figure 12 until the water in the

tank reaches 80-85°C. Next the heated water is pumped into the water loop till about 5 pounds of water are added to the overflow tank. After the loop is filled sufficiently the water loop pump is turned on and the overflow tank is pressurized to 30 psig. The water is then circulated for a hour to 4 hours depending on the level of bubbles present inside the water loop. Following the circulation of the water loop the steam line is prepped near the end of deaeration by first filling the steam line up with steam at test pressure (60-80 psig depending on the study). The heat tape is then turned on and set to continuously add heat to the steam to become at least 1-2 degree superheated to ensure a quality of 1. With both the portions of the test apparatus prepared steam flow is then injected into the test section. Following injection, the steam and water pressures are adjusted to the desired conditions for the given test. Next the high-speed camera in front of the test section is adjusted and focused so that the entirety of the plume is in frame and the lighting is deemed sufficient. The camera is then set up using the software PCC as seen below in Figure 22.

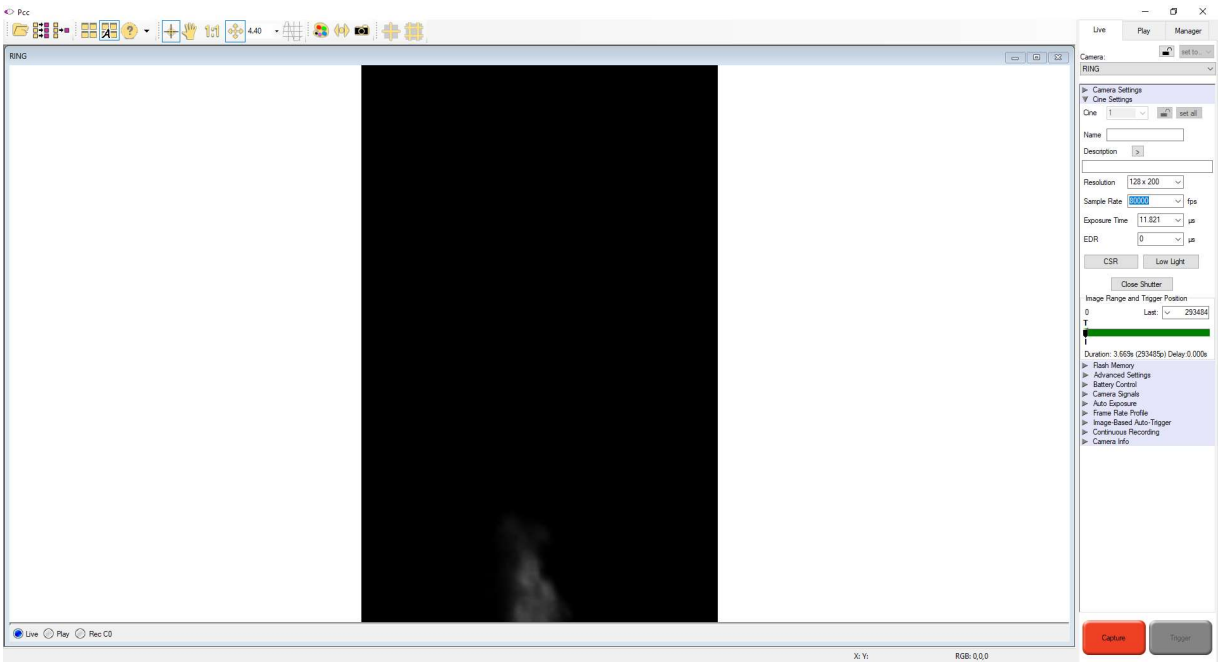

Figure 22: PCC Setup

To begin data collection the water temperature is lowered to below 25 °C by increasing the cold flow to the heat exchanger. Next the water flow is restricted to allow for the temperature of the water inlet to approach 25 °C. The high-speed camera and LabVIEW recording are triggered as the water flow reaches this temperature. The data is saved and these steps are repeated at every 5 °C until 80 °C. is data from 25-80 °C.

4 Simulation Settings

For simulating the steam flow through the nozzle Ansys R19.1 was used specifically the fluent package. Below in Figure 23 is an example of the workflow used to simulate and organize the results.

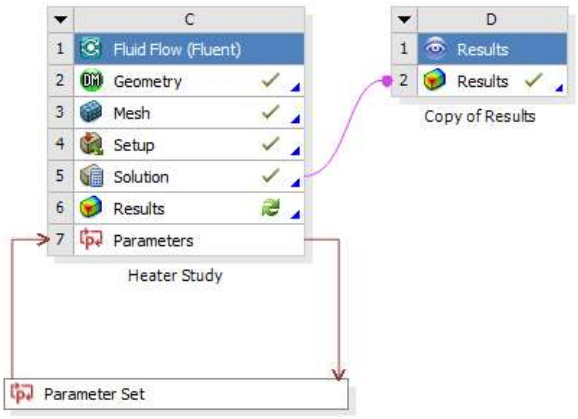

Figure 23: Ansys Workflow

To start a simulation the geometry is created either in design modeler or in solid works. Design modeler is used for its ability to integrate with the parametric studies available in Ansys. An example of one of these parametrized models is found below in Figure 24.

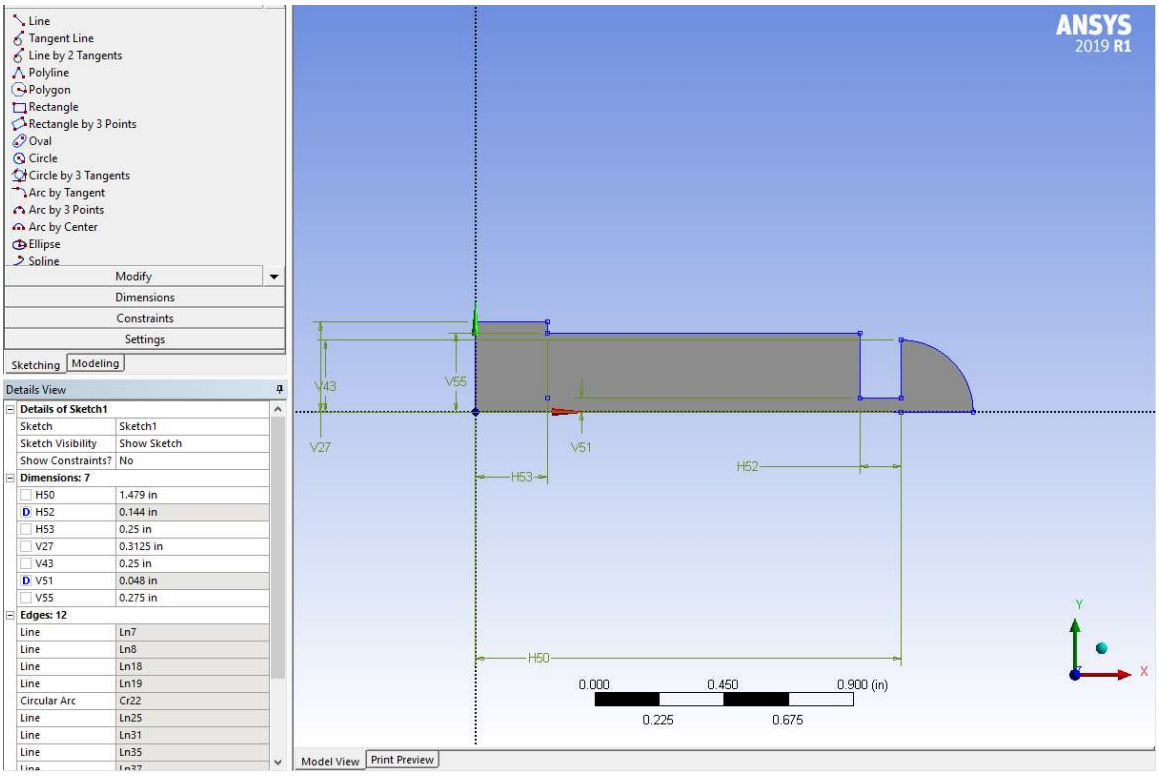

Figure 24: Parametric 2D Model of Nozzle

For the simulations done in this work all the geometries are 2D axial representations as symmetry is assumed for the flow through a nozzle. The geometry is created and then transferred to Fluent's meshing module. Most of the meshes were set to 50 µm for the element size and near the inlet and outlet a finer element of 25 micrometers was used. In Figure 25 is a mesh study that was used to decide these settings based on the simulated mass flow through a nozzle.

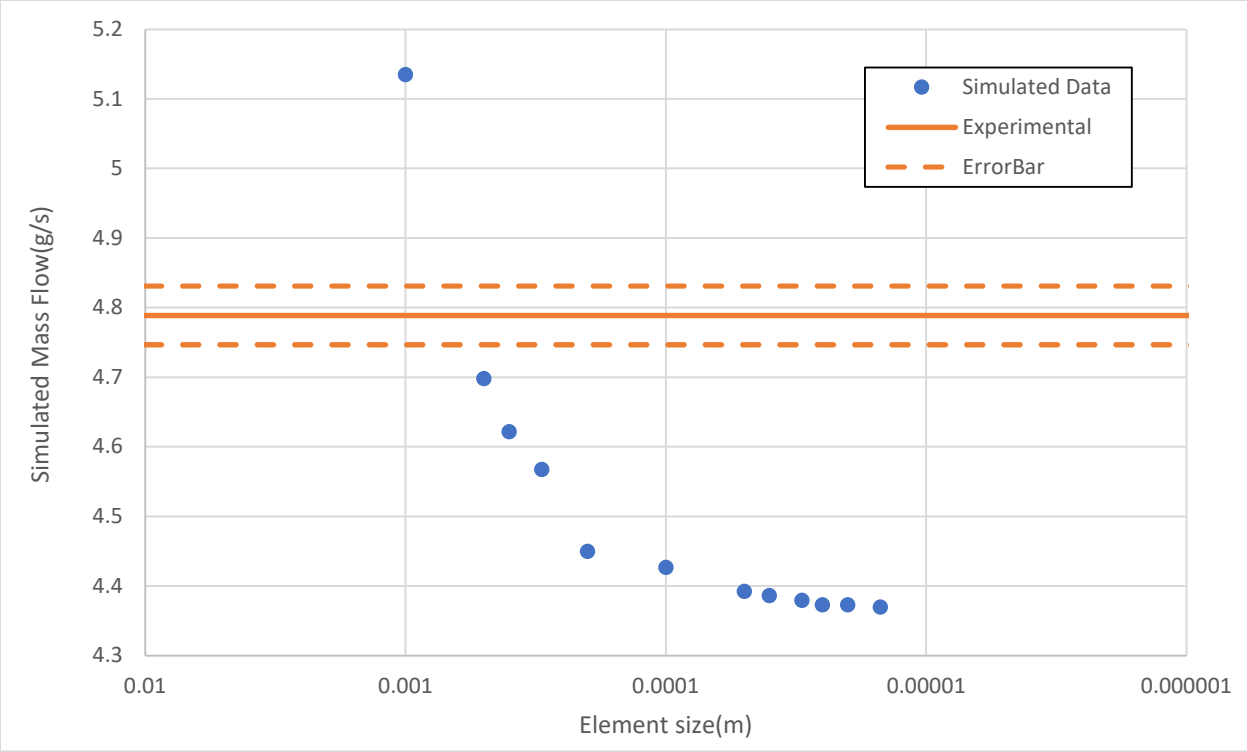

Figure 25: Mesh Study Results

A sphere of influence was used to define the regions with higher element sizing as seen below in Figure 26 where the density of elements is noticeably larger.

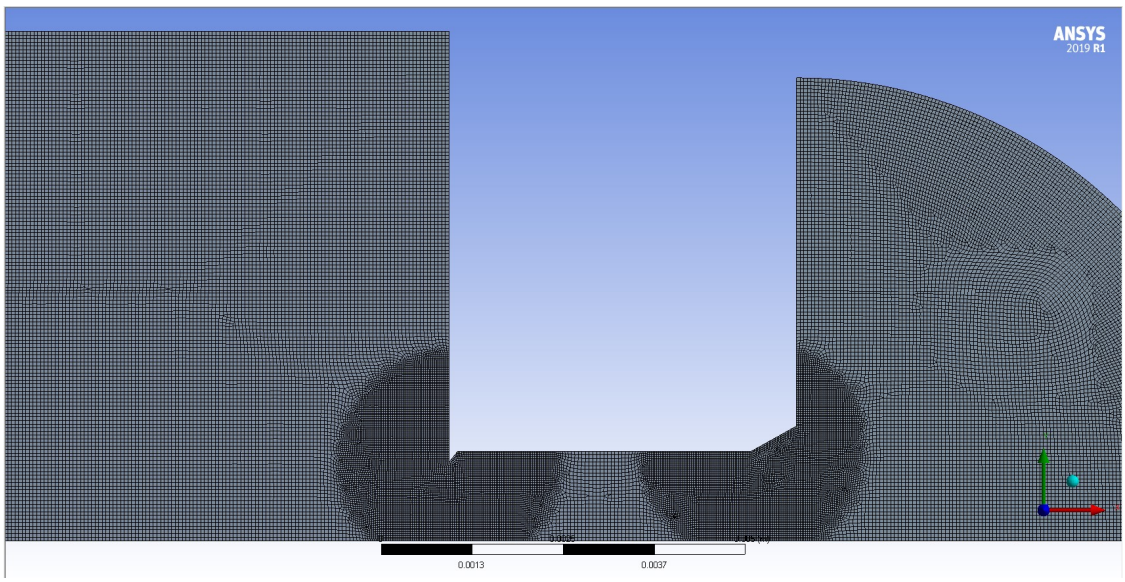

Figure 26: Mesh Example

After the geometry is meshed the boundaries are defined for an axial symmetric simulation. The boundaries used are axis, inlet, outlet, walls, and fluid which are all labeled in the diagram of the Ansys fluent window in Figure 27.

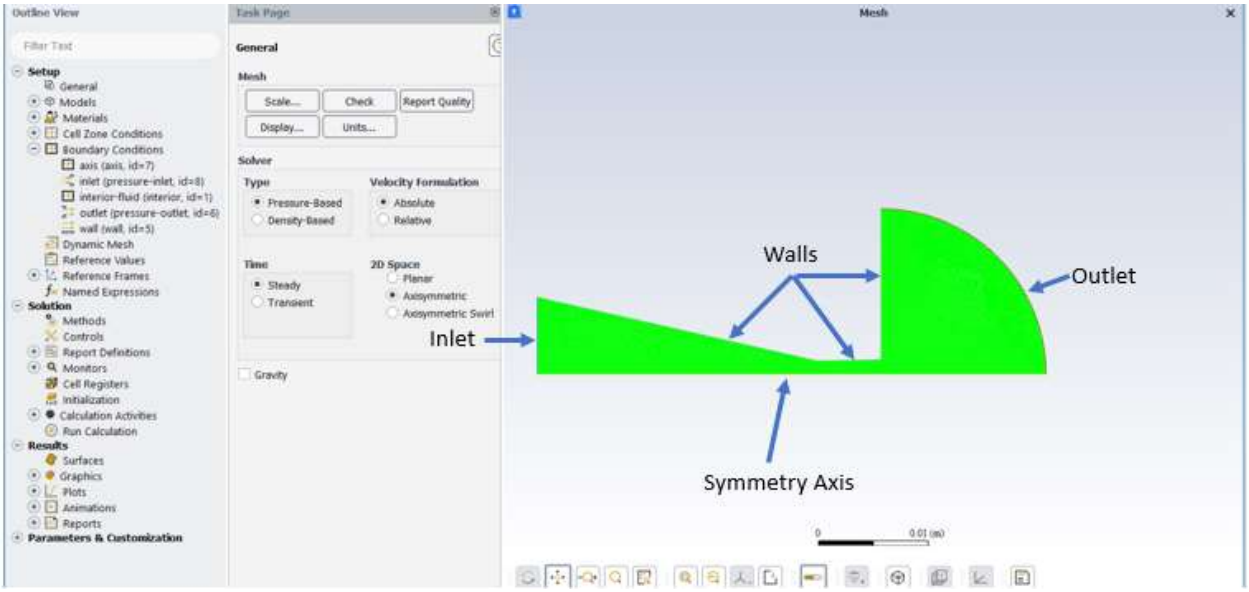

Figure 27: *Setup Diagram for 2CD Nozzle*

With the boundaries and mesh created the data is then transferred to the setup module in Ansys where the conditions and fluid properties are set. The solver used is an axisymmetric pressure based steady state solver. The inlet boundary above is set to the inlet pressure using 80 psi for most studies and varied when other steam pressures are tested. For the outlet boundary a pressure outlet is set to the pressure of the water pressure tested in the experimental tests. Finally the walls are set as no slip stationary walls using a standard roughness model and a heat flux of 0. Following the definition of the boundaries the fluid properties were set using IAWPS and using ideal gas law for the density of the steam to account for compressibility in the nozzle. Next the solver environment is set to a convergence criterion of 1e-4 for all functions and 1e-6 for energy. To begin the simulation a hybrid initialization is ran

followed by a run of 20,000 iterations or until the solution has reached convergence. An example of the results of a simulation are shown below in Figure 28.

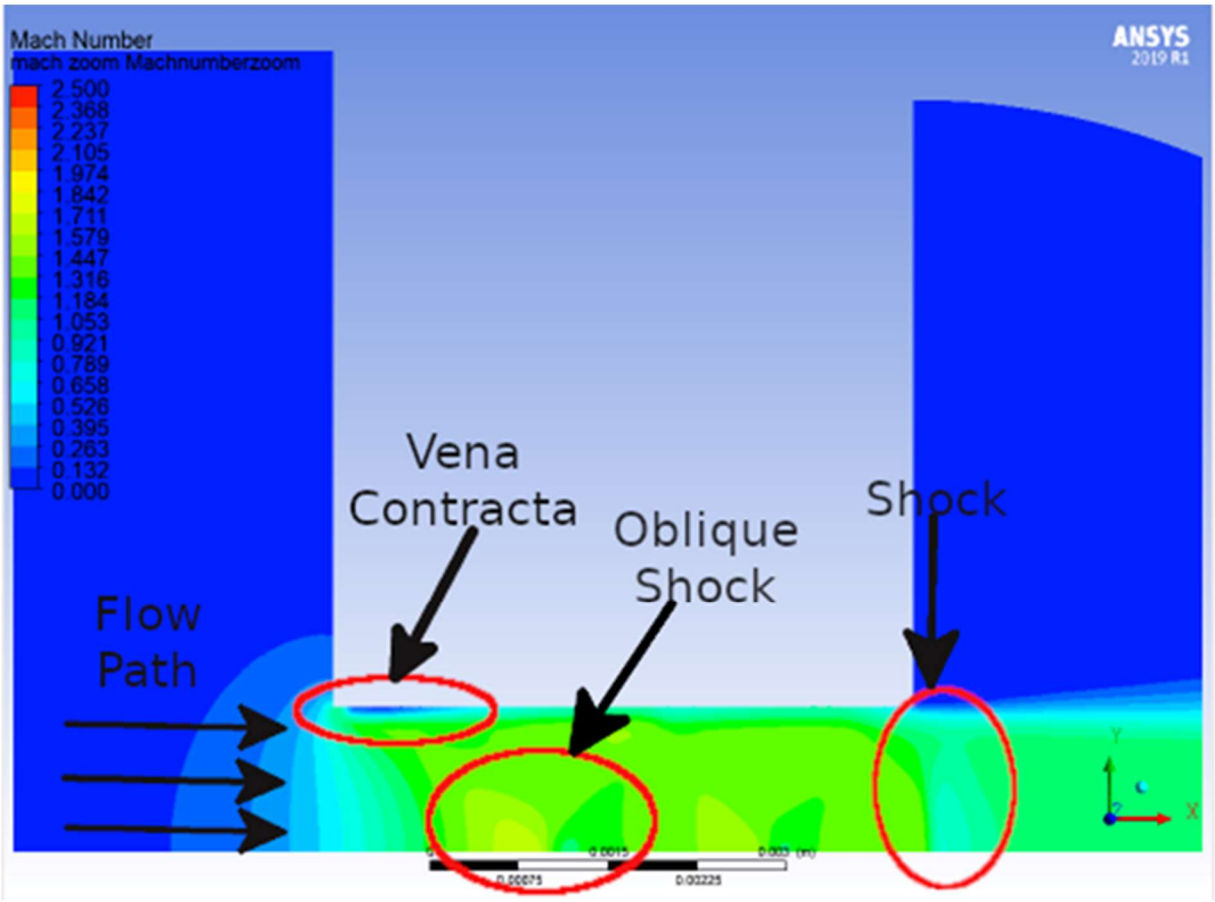

Figure 28: 2-2S Example Results from Ansys Fluent

When looking at the results of all of the studies taken in this work it was noticed that there were three key elements observed in flow of the nozzles simulated. The first being the shock which appears in almost all nozzle simulations that are below the critical pressure ratio of the steam. They are indicated by a large drop in both pressure and velocity either inside the nozzle or downstream of the outlet. The next element observed in Figure 28 are oblique shocks which are only seen in the orifice type nozzles tested and not in the converging or converging

diverging nozzles. The oblique shock is indicated by a sharp drop in pressure and velocity but rather that continuing to drop in will jump back up in pressure and Mach number forming a diamond like structure in the flow that will eventually result in a final shock downstream of the initial oblique shock. The final element observed in the simulated flow is the vena contracta which is a portion of the nozzle where there is no flow at all due to rapid contraction of the throat. Due to the need of this rapid contraction this element is only seen in orifice nozzles and not in any of the nozzles with a converging inlet. This portion of no flow causes the area ratio of the nozzle to increase as there is a smaller throat due to the contraction.

5 Regime Classification

For this study regimes are used to categorize and describe the oscillatory behavior of the steam plume as it condensates. For all the studies discussed in this thesis there are six regimes used which are the stable, condensation oscillation (CO), transition, unstable, early condensation, and unstable regimes. The stable regime is categorized by its ability to maintain a constant shape with very little change in the height of its tip. An example of a stable plume can be seen in top left of Figure 29. Previous papers have described this regime [2], [9], Next the CO regime is defined by its oscillating tip as it condenses at different heights sometime this is accompanied by little pockets of steam separating from the main plume but still small enough to not be considered bubbles. An example of this tip change can be seen in the two top right frames of Figure 29. The CO regime evolves into the transition regime where the tip oscillations become necking and bubbling of the plume as the instabilities of steam condensation begin to take hold of the process. The transition regime still has pockets of stable plume as it is switching back and forth between a stable and unstable regime. An example of both of the stable and unstable parts of the transition regime are shown below in the middle of Figure 29. If the instabilities dominate and become a constant element of the video the steam plume enters the unstable regime. This regime is described as having large necking and bubble formation as the steam exits the nozzle as seen in the bottom left of Figure 3. The next two regimes fall under the unstable regime but are defined further due to their lack of plume. The first of these is the chugging regime where large bubbles are formed and separated at the nozzle exit resulting in moments of no plume as seen in the bottom right of Figure 3. The final regime is the early

condensation regime which is when there is little to no plume present and all the steam condensates inside the nozzle as presented in the bottom of Figure 3.

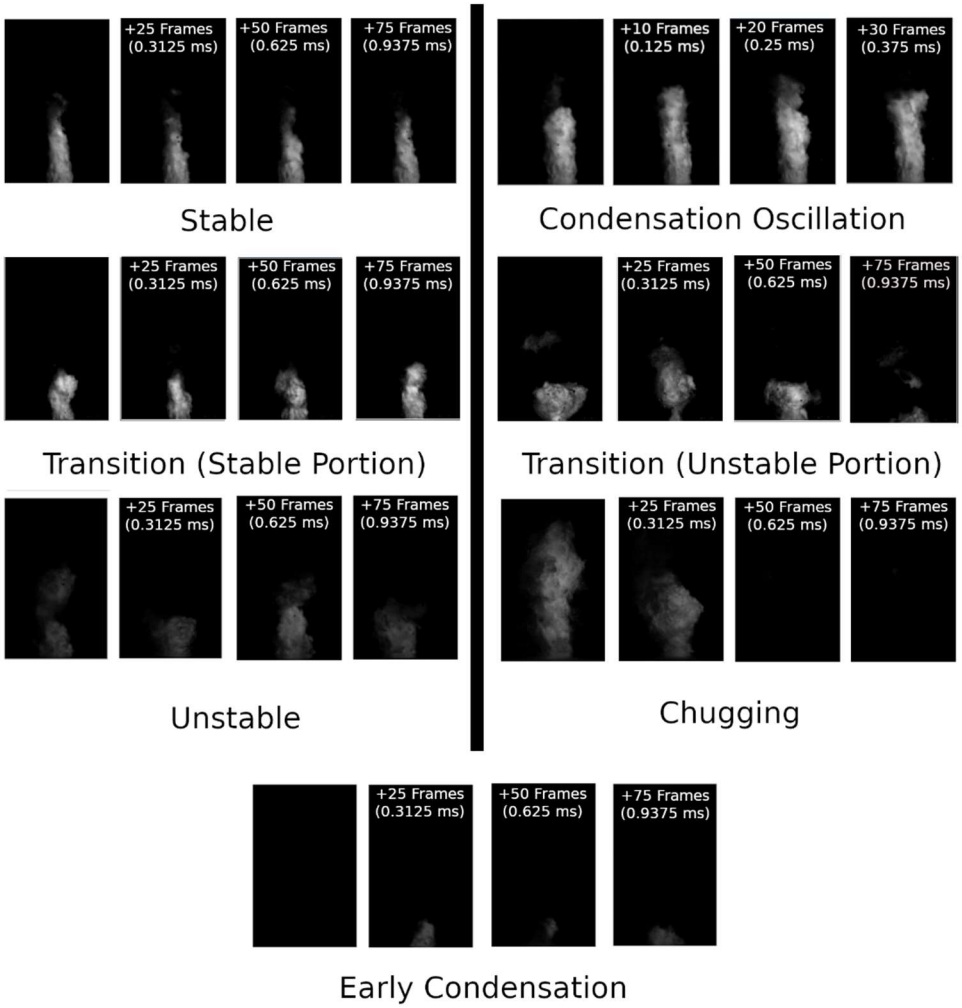

Figure 29: Stability Regimes

With the regimes defined MATLAB's image processing toolbox was used to quantify the different aspects of each regime similar to the approach used in the work from E. Hujala et al[38]. The video footage is first processed with MATLAB's imshapen to clean up the image before its then binarized by using a comparison to a threshold based on the lighting conditions. The next step is using the functions regionprops and bwboundaries to isolate the different objects in each

frame. In addition to isolating each object the diameter, height, and area of each object is object. Then using assumptions about where the plume is relative to the frame the bubble and plume are defined separately from the objects detected in MATLAB. This process is illustrated below in Figure 30.

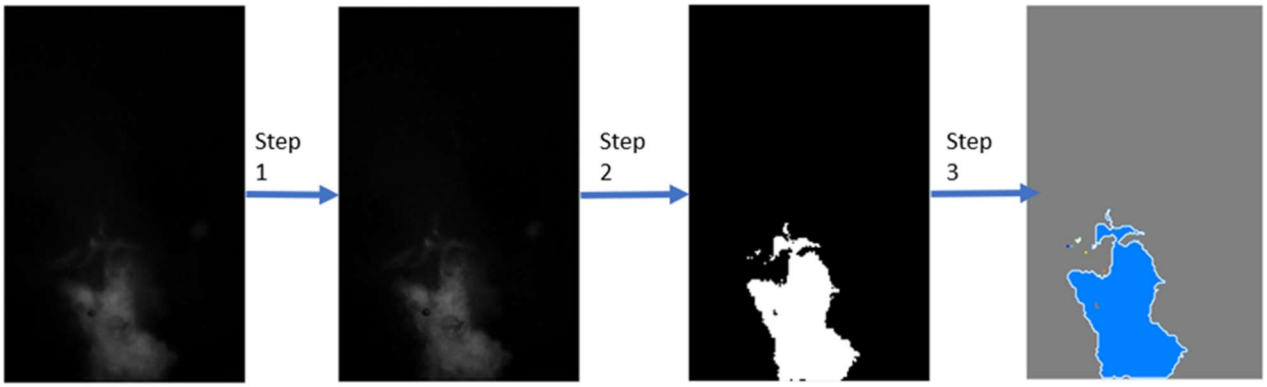

Figure 30: Video processing example

After processing all the frames for a test point, the data is then used to determine its regime using the flowchart in Figure 31.

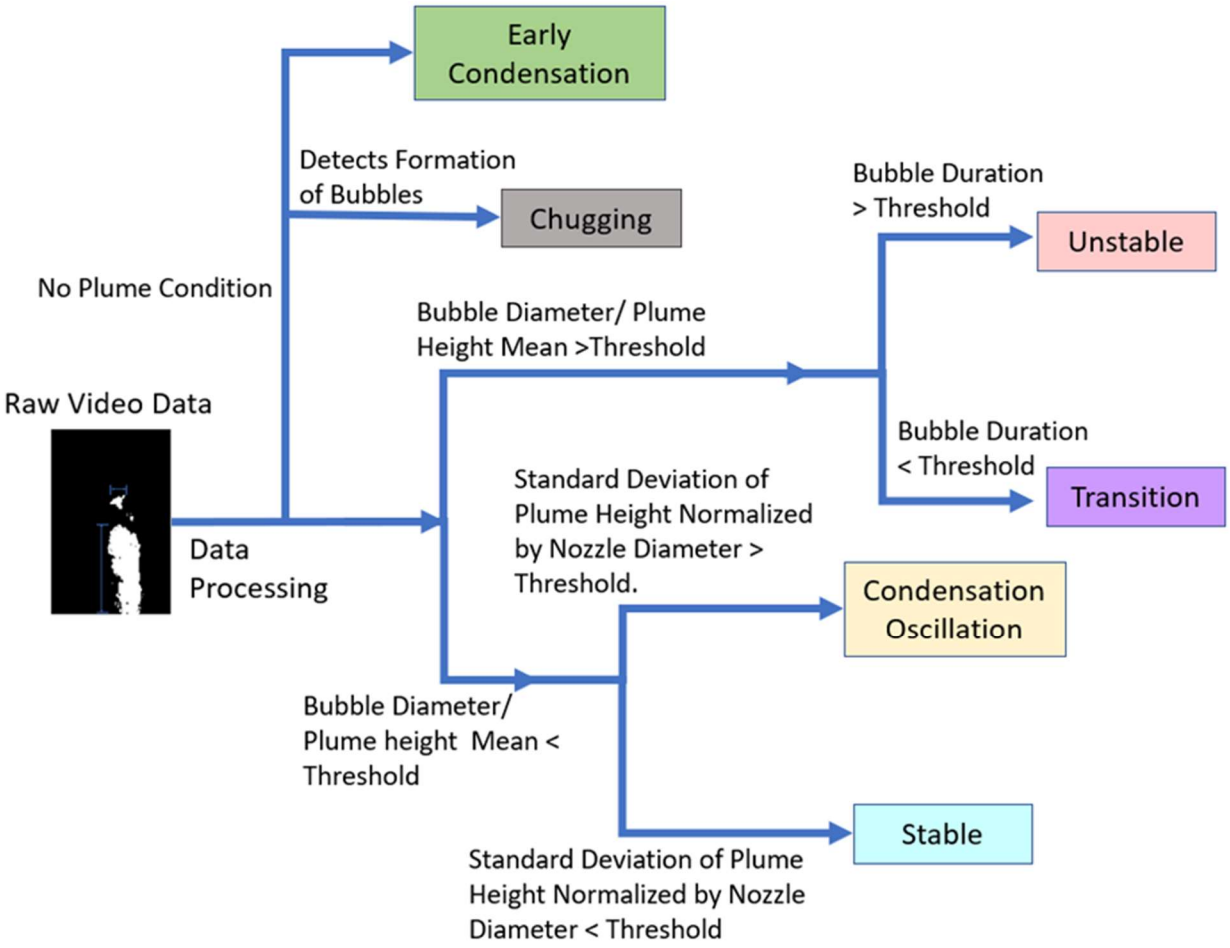

Figure 31: Regime Flowchart

First the software checks if there is an extended amount of time where the plume is nonexistent and directs the flow chart to either early condensation or chugging. From here the software determines if there is any sizable formation of bubbles that are released into the water flow and will determine the data point to be chugging otherwise it will default to early condensation. If there is consistently a plume at the exit of the nozzle it, then decides if it is in a completely stable regime (stable and CO) or if it experiences enough instabilities to be considered transitionary or unstable. The criteria used to make this decision is the average bubble diameter using a threshold of 50% of the throat diameter. An example of this threshold

being used to distinguish between CO and transition can be seen below in Figure 6a with the different regimes highlighted in the background of the plot. Following the path in Figure 5 up the next criteria used is the bubble duration. This is used to determine if the instabilities are only momentarily like in the transition regime or if bubble formation is a consistent component of the footage. In addition to separating the two regimes from one another it is also able to demonstrate how unstable the plume is in the unstable regime as illustrated in Figure 6a as the bubble duration continues as the plume visibly gets worse and worse. Going to the final decision of the flow to decide if the flow is purely stable or CO the plume height fluctuation is used to separate the two regimes. To capture the height fluctuation the standard deviation of the plume tip position is used and is normalized by the nozzles diameter to have a unit less measurement as seen in Figure 6c.

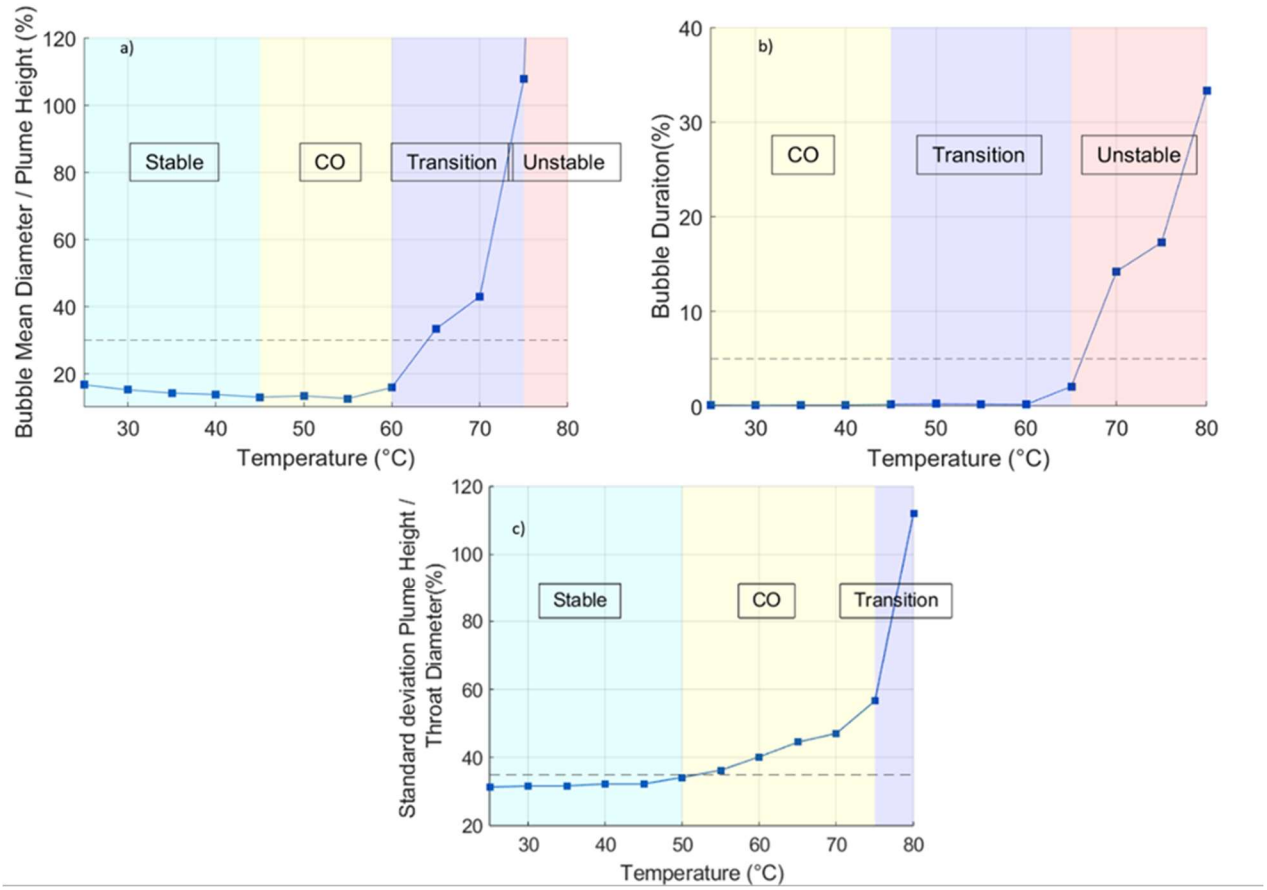

Figure 32: Regime Map Thresholds

The video data is then processed so that the regimes can be determined for each of the nozzles. But when reviewing the results there are some data points due to bad video data will improperly represent the regimes. The unedited results of a first pass with this algorithm is pictured in Figure 33 a.

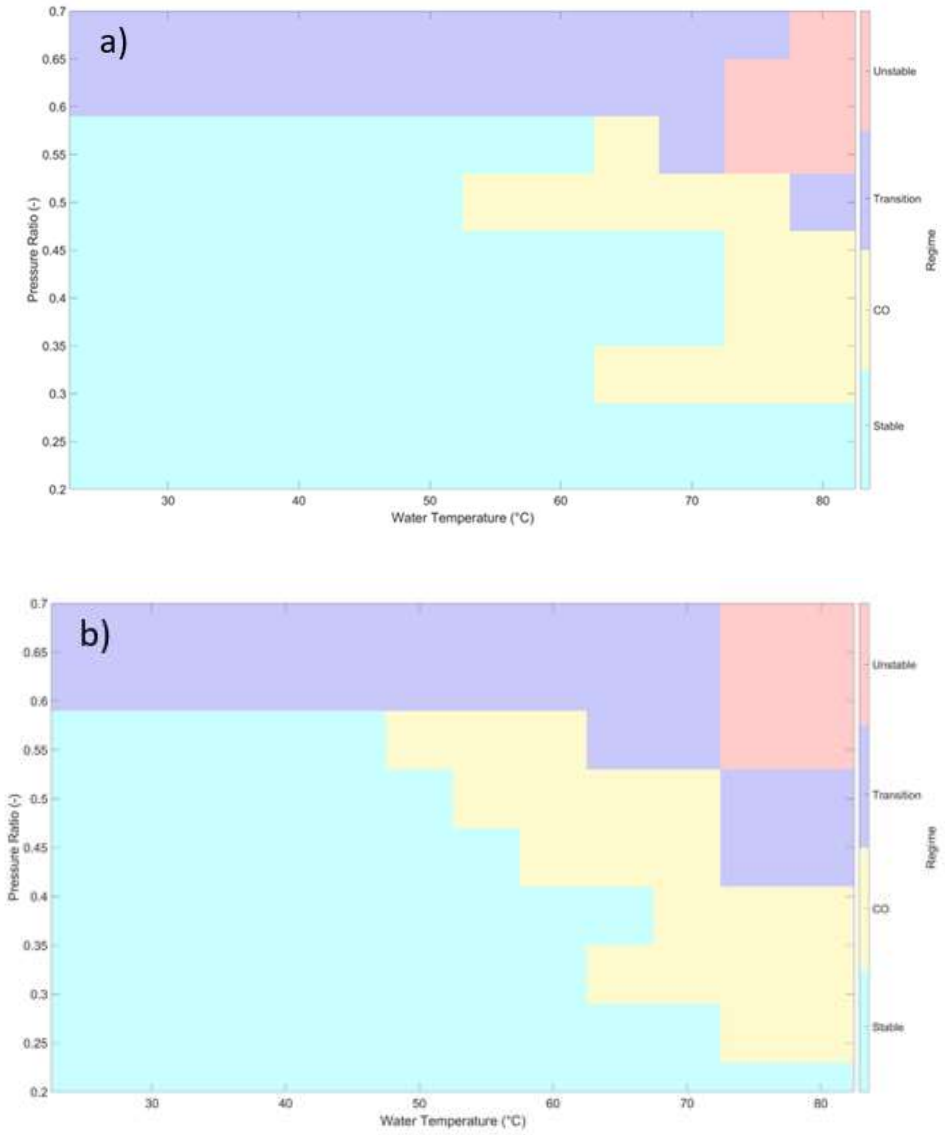

Figure 33:Regime map results (unedited a, edited b)

The map illustrates how occasionally there will be false positives for bubble detection and plume variation. This occurs because the video taken may have improperly set the exposure or focus such that edges of the plume may have the same RGB values as portions of the test section. Another way that this might occur is that the light used to allow for high-speed footage of the steam plume may be improperly positioned such that the tip of the plume is

vastly more bright than the bottom and even with a proper threshold being used for that data set will still cause the program to register the plume as a bubble rather than a consistent plume. Finally, it is possible that due to the camera moving during testing or the bottom of the frame not being set properly some of the steam plume to not fully be captured in the frame whilst testing and may not be caught till the algorithm is run. An example of these improperly shot frames is depicted in Figure 34.

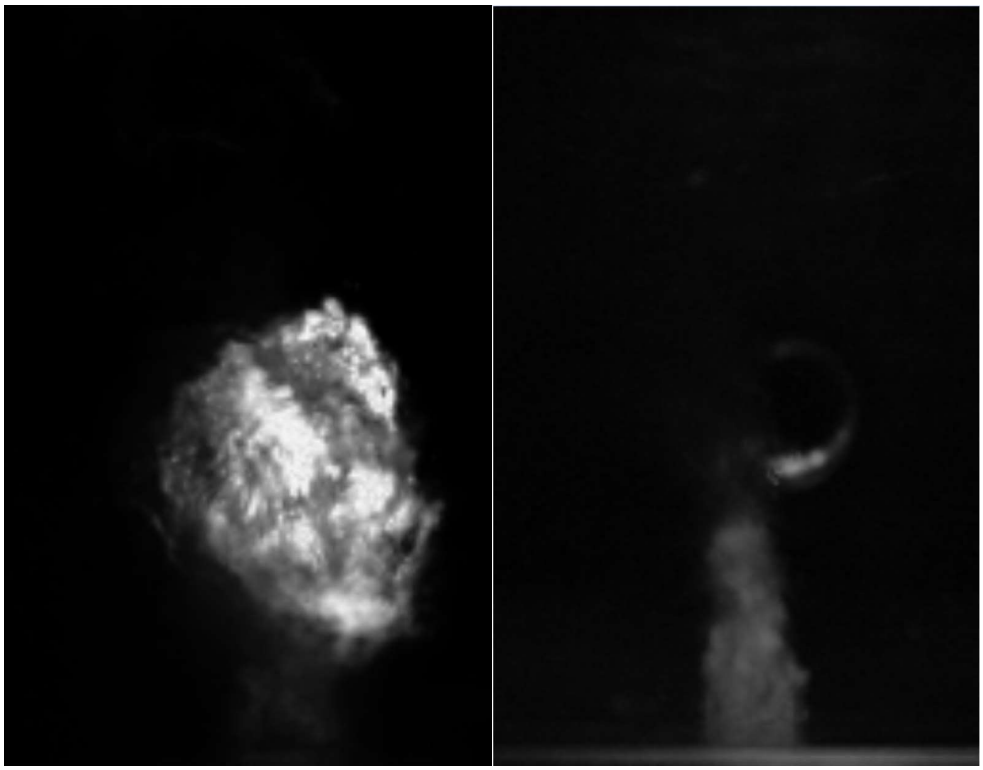

Figure 34: Video Frames the Algorithm has trouble with (Improper lighting position right and improper exposure left)

When one of these issues is identified with the video footage the data is then reviewed to ensure a correct identification of the regime. This is done so that previous data doesn't have to be retaken when all the other aspects of testing are satisfactory as it takes a full day to

recreate the conditions of previous experiments. Alongside a qualitative review of the footage the high frequency pressure and audio data is used in conjunction to help understand a clear distinction between the regimes. To analyze the audio and pressure data the power spectral density code that Zach Alden previously wrote is used to produce frequency graphs for each of the temperatures for a full sweep of data. An example of one of these graphs is shown below in Figure 35.

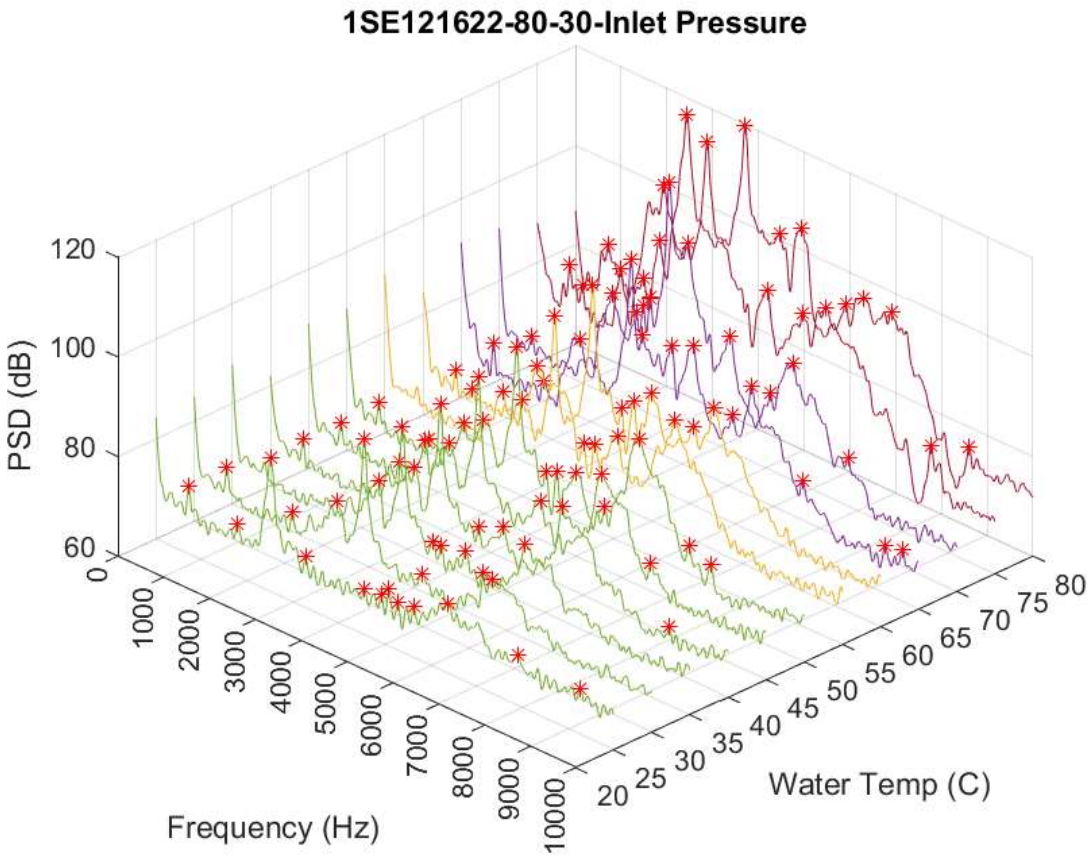

Figure 35: Power Spectral Density 3D Graph for Dynamic Inlet Pressure Data with a 1S Nozzle at 80 SP and 30 WP

In Figure 35 the colors of each of the lines represent the regime they are in at each temperature. As the plume becomes more unstable the power at the dominant frequencies grows in strength as well as the secondary frequencies become more and more prominent. By reviewing these plots, it adds a second layer of confirmation to the regimes classified used with the algorithm or the ones that needed to be reevaluated using qualitative means.

6 Shock location Study

The first study performed in this thesis looked at how the sub or supersonic outlet flow of steam affected the stability of plume. This study focused on using two nozzle types: converging and converging diverging nozzles as depicted in Figure 37.

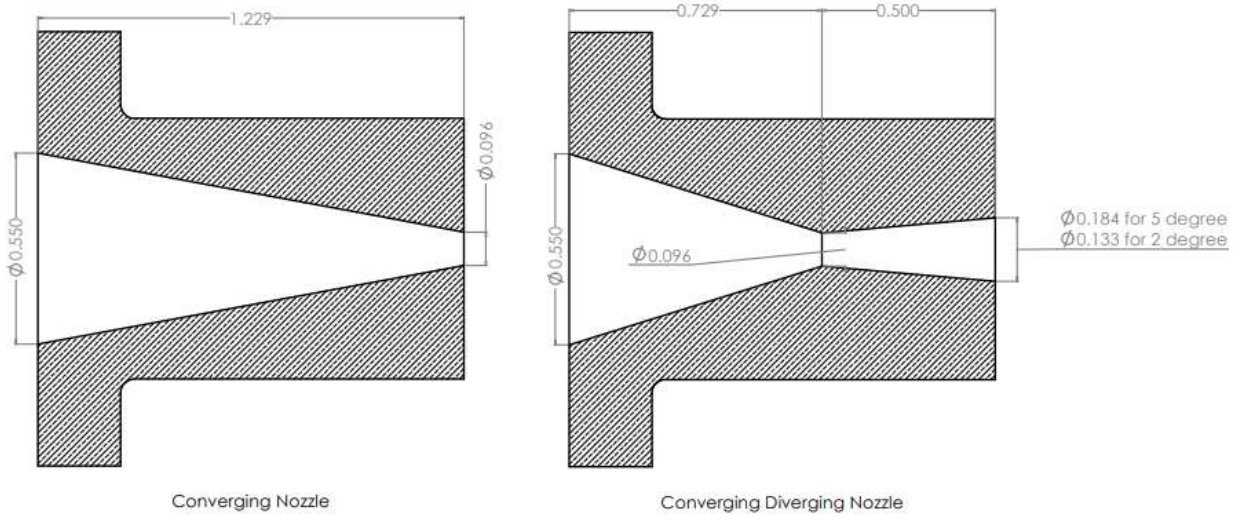

Figure 37: Converging and Converging Diverging Nozzle Drawings

Using the dimensions from Figure 37 simulations are performed on all three nozzles at 9 pressure ratios between 0.2-0.68. The inlet pressure for all the simulations in this study is kept the same at 80 psig so that the only varying factor is the pressure ratio. An example of Mach contours of each of the nozzles simulated at 0.48 pressure ratio is shown in Figure 38.

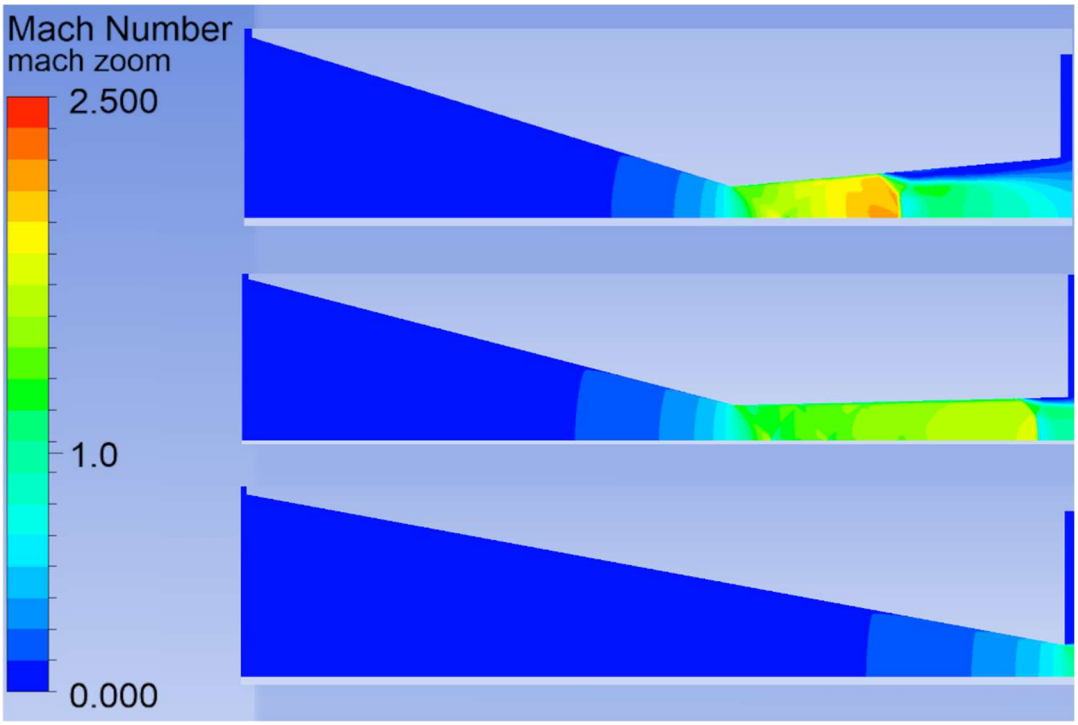

Figure 38: Mach Contours for Shock Location study at 0.48 PR (5 degree top, 2 degree middle, converging bottom)

Each of the simulated data points were also tested and recorded using the steam injection loop. Using the experimental data a regime map was created for each of the nozzle using pressure ratio and temperature as the two axis. The shock location observed in all of the CFD data points is then normalized by the length of the nozzle and then plotted against the pressure ratio. Combining these 4 plots in Figure 39 helps illustrate the effect of the different geometries.

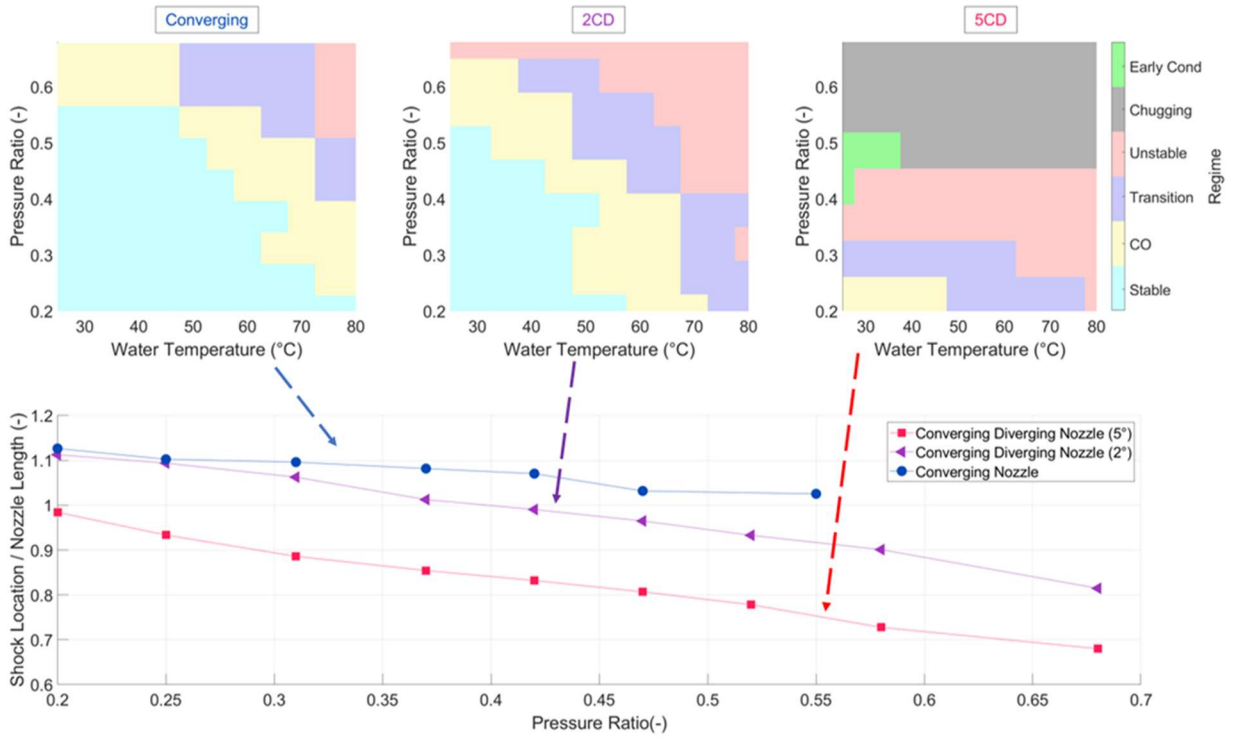

Figure 39: Converging and CD Nozzle Regime maps and Shock Location as a function of Pressure Ratio

In the shock location plot the converging nozzle data points cut off above 0.55 PR because the simulation predicts that the flow will be subsonic at the exit (no shock). The regime maps show that the converging nozzle is the most stable over the largest range of pressure ratios and temperatures. The CD nozzle with a 5° taper demonstrates the worst performance. This nozzle is unstable above 0.35 PR and experiences chugging for a significant portion of the conditions tested. The CFD results in the bottom half of Figure 39 exhibit a strong correlation between the steam flow inside a nozzle and the stability. The shock occurs down stream of the nozzle exit for the most stable nozzle (converging) consistently except above 0.55 where the flow is subsonic. In contrast, the 5° taper exhibits a shock inside the nozzle at all pressure ratios. These trends illustrate that the further downstream a shock, the better the performance of a

nozzle in relation to its ability to maintain a stable plume. Additionally, these results show how simple modeling tools can be to predict the performance of a nozzle using the pressure ratio and geometry of a DCC application.

7 Manufacturing Study

The next study focused on using the same nozzle design but altering the type of manufacturing. For this study 3 orifice nozzles with an LD ratio of 2 were manufactured using lathe but by two different people and 1 using EDM manufacturing. The target design for these nozzles is shown in Figure 40.

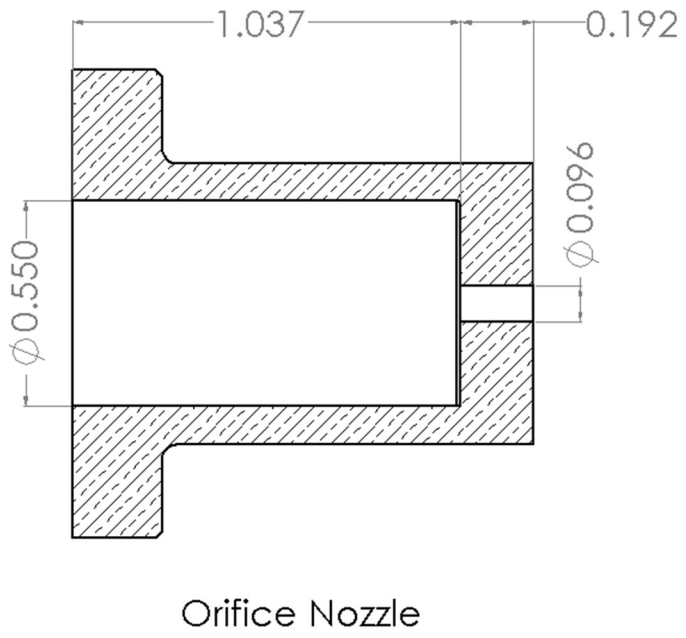

Figure 40: 2S Nozzle Design

Each of these nozzles were x-ray scanned to determine the internal structure and the microfeatures at the inlet and outlet of the orifice and the resulting images are shown in Figure 41 with the outline of their geometries in red.

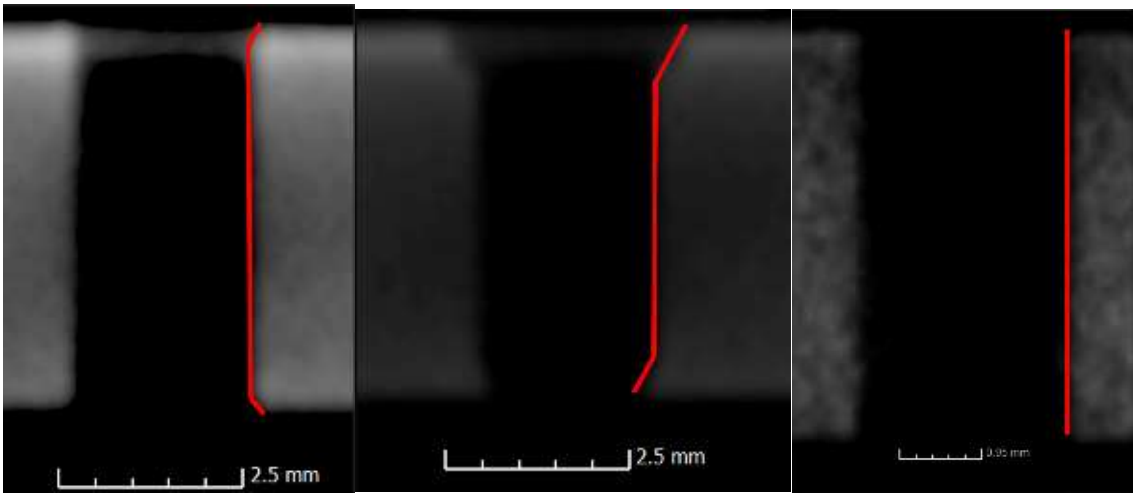

Figure 41: Xray Scans of 2S Nozzles (2S Left, 2-2S middle, 2S EDM right)

Inspecting the scans it is clear that the 2S EDM is the closest to the specified drawing in Figure 41 with perfectly straight edges. In contrast the 2-2S nozzle has a clearly defined burr at the inlet and a large, chamfered edge at the outlet. Finally, the 2S has small chamfers at both the inlet in outlet that are much less drastic than as seen with the 2-2S. After these nozzles outlines were acquired, they were imported into Ansys fluent to be simulated under the different pressure ratios studied in this experiment. An example of the Mach number results for all three of these nozzles at 0.48 PR is shown below in Figure 42.

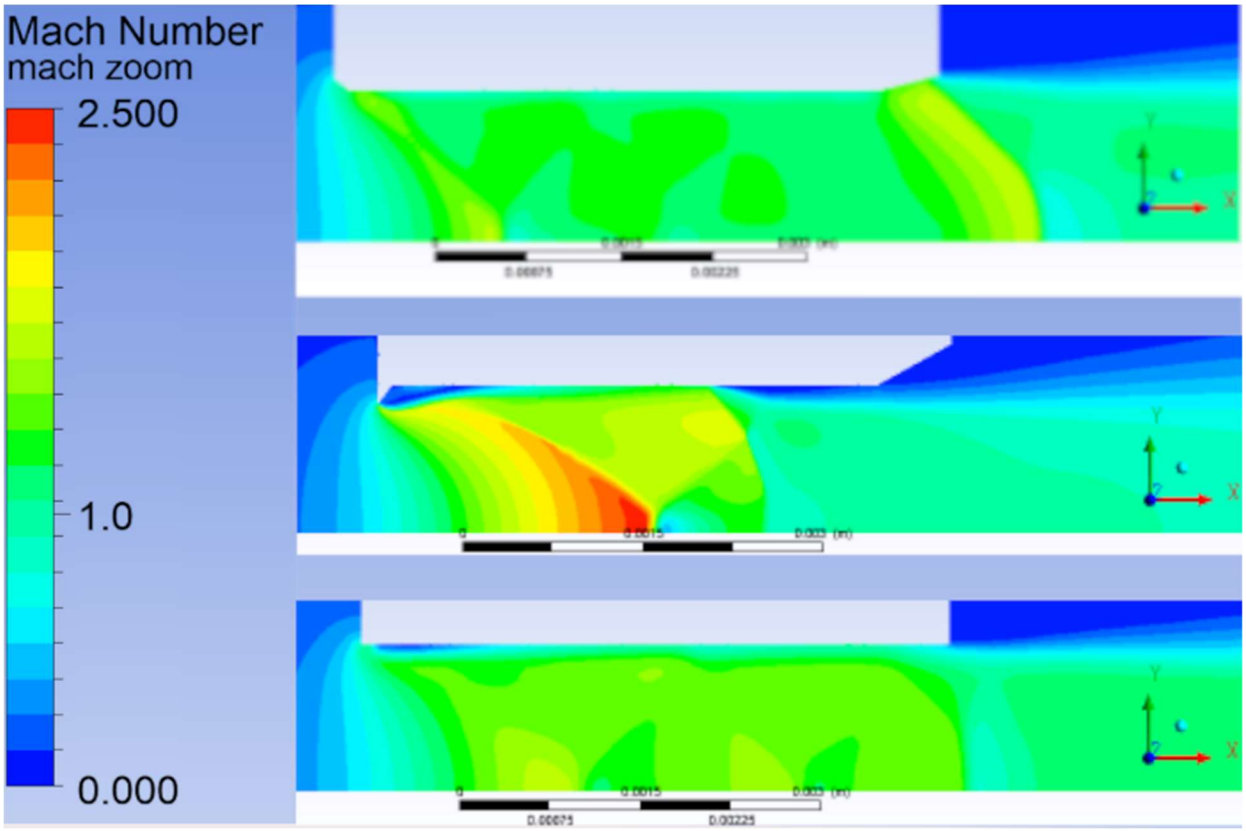

Figure 42: Mach Contours for orifice nozzles at 0.48 PR (2S top,2-2S middle, 2S EDM bottom)

Looking at just the contour results in Figure 42 based on the results in the shock location experiment the 2S appears to perform the best pushing the shock downstream of the outlet much further than the other 2 nozzles. All three of the nozzles have oblique shocks early on in their length with the 2-2S having the strongest shock reaching above 2.5 Mach then dropping down to subsonic. While it has the strongest oblique shock the 2-2S is the only nozzle at this pressure ratio that is not capable of pushing the last shock outside of the nozzle causing the flow to be subsonic as it reaches the outlet. Additionally, the 2S has the strongest shock of all of the nozzles as it reaches the exit going upwards of 1.5 Mach. To compare the simulated data the shock location was found for each of the 3 nozzles using the location of the final shock and

then dividing the result by the orifice length rather than the total nozzle length as done in the shock location study. The tests conducted on these three nozzles were done from a pressure ratio of 0.2-0.58 at 12 different temperatures. The calculated shock location as a function of pressure ratio and the experimental regime maps are plotted in Figure 43 like the previous Figure 43.

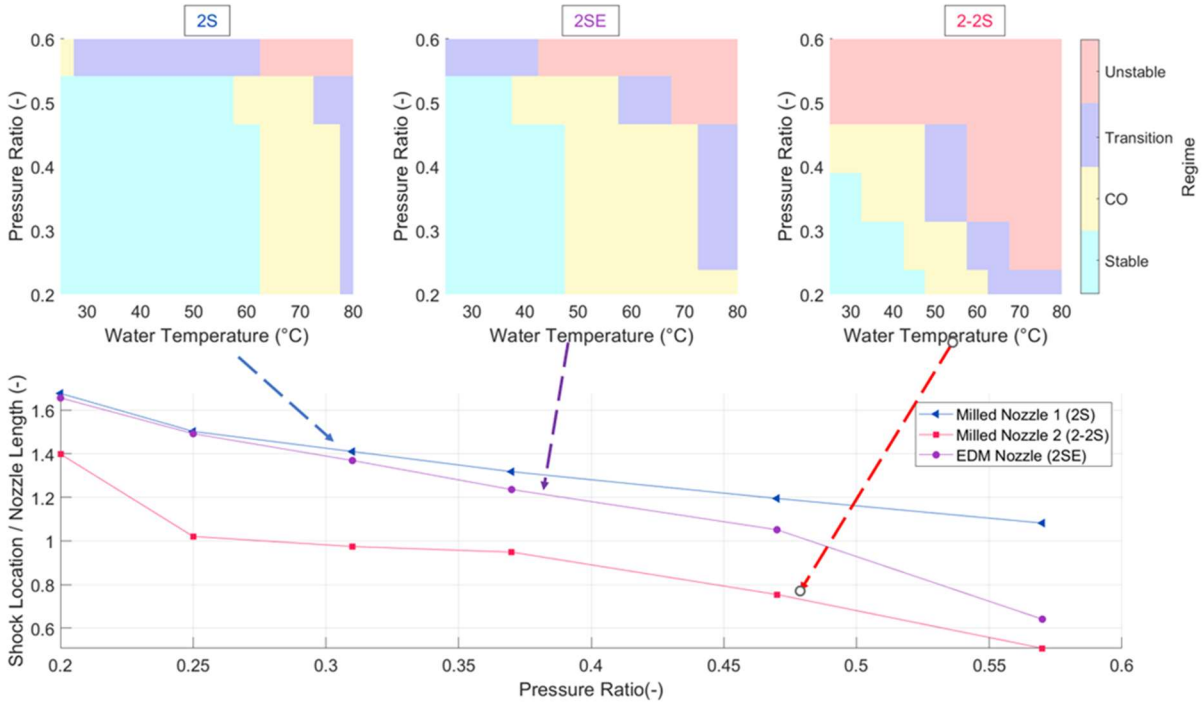

Figure 43: Bubble Duration and Shock Location as a function of pressure ratio for 2S nozzles manufactured using different techniques.

The correlation between stability and shock location seen in Figure 43 validates the previous findings of the shock location experiment. The flow from the 2-2s nozzle exits the orifice subsonic above a PR of 0.25, whereas the flow from the 2S nozzle shocks outside the orifice for all simulated pressure ratios. As expected, this results in poor performance from the 2-2s nozzle, which has an unstable plume at a PR of 0.25, and good performance from the EDM

and 2S nozzles, which remain stable until a PR of 0.5 – 0.55. The results of this experiment and the shock location experiment confirm the correlation between DCC stability and the location of a shock in the vapor's flow field and by extension demonstrate the importance of describing the geometry of nozzles when studying plume stability.

8 Summary and Conclusion

Direct contact condensation (DCC) that results in unstable plumes will generate destructive noise and vibrations that limit their use. This thesis increases the understanding of the effect of nozzle geometry on the conditions that cause instability in DCC. Using single phase compressible ideal gas CFD the flow inside the nozzles was simulated to help understand the correlation between steam flow and stability. The correlation found in this thesis focused on the relationship between shock location and the experimental onset of instability in DCC. Nozzle geometry, including small features due to manufacturing defects or tolerances, strongly affects shock location and therefore has an impact on plume stability. The results highlight the importance of disclosing and analyzing the nozzle geometry carefully in future DCC studies. It was demonstrated that single-phase CFD simulations of the flow inside the nozzle can be used successfully to predict nozzle performance and design better nozzles.

There are many avenues for future work in DCC. Specific to the facility used in this thesis, work could be done to improve the data quality with a new test section. Specifically, the outlet pressure sensor could be replaced with a window and an LED panel to improve video quality. I believe back-lighting the plume would help produce more uniform video data for future experiments. It would be an easy change as the outlet pressure mount and the glass window have the same dimensions and are interchangeable. Additionally, the outlet pressure sensor could be mounted at a different portion where there are more consistent readings as it has been one of the most inconsistent measurement devices in the test apparatus. Another change to the loop would be to move towards more sensitive control valves and possibly integrate PID controls to help smooth out any change in pressure or flow rate that may occur as

the bladder tank fills up. This would help get better data as well as require fewer minute changes from the user when testing to help with efficient usage of time.

Future studies could explore many different aspects of crossflow DCC. One potential study could look at adding turbulence to the test section by removing and replacing the flow straightener with mixing vanes. This would allow for an in-depth analysis of how to affect the water flow in a perpendicular crossflow without having to change the flow rate or pressure of the water loop. Another study could continue to advance the CFD studies done in this work by including the multi-phase interaction and focus on one nozzle to understand the interaction of the two phases in a way not measurable with the current test apparatus. The types of nozzles tested could be expanded to include more unique designs such as an internal counterbore or non-circular hole nozzles.

Works Cited

[1] S. Sideman and D. Moalem-Maron, “Direct Contact Condensation,” in *Advances in Heat Transfer*, J. P. Hartnett and T. F. Irvine, Eds., Elsevier, 1982, pp. 227–281. doi: 10.1016/S0065-2717(08)70175-8.

[2] Z. R. Alden, G. D. Maples, K. M. Dressler, G. F. Nellis, and A. Berson, “Plume Stability During Direct Contact Condensation of Steam in a Crossflow of Subcooled Water, at High Mass Flux and With a Small Nozzle Diameter,” *J. Heat Transf.*, vol. 143, no. 9, p. 091602, Sep. 2021, doi: 10.1115/1.4051667.

[3] V. S. Barot, “Thermal and fluid behavior of a steam-driven jet in subcooled water crossflow,” 2011., 2011. Accessed: Apr. 15, 2023. [Online]. Available: https://search.library.wisc.edu/catalog/9910105473402121

[4] M. J. Brennan 1994-, author, “Conditional stability of a steam jet during direct contact condensation in subcooled water crossflow,” 2019., 2019. Accessed: Apr. 15, 2023. [Online]. Available: https://search.library.wisc.edu/catalog/9912808857302121

[5] “Giffard’s Patent Model of a Steam Boiler Injector – ca 1860,” *National Museum of American History*. https://americanhistory.si.edu/collections/search/object/nmah_846123 (accessed Apr. 21, 2023).

[6] P. J. Kerney, G. M. Faeth, and D. R. Olson, “Penetration characteristics of a submerged steam jet,” *AIChE J.*, vol. 18, no. 3, pp. 548–553, May 1972, doi: 10.1002/aic.690180314.

[7] B. Qiu, S. Tang, J. Yan, J. Liu, D. Chong, and X. Wu, “Experimental investigation on pressure oscillations caused by direct contact condensation of sonic steam jet,” *Exp. Therm. Fluid Sci.*, vol. 52, pp. 270–277, Jan. 2014, doi: 10.1016/j.expthermflusci.2013.09.020.

[8] J. Wang, C. Chen, D. Liang, T. Lu, and S. Bai, “Temperature and pressure oscillations induced by steam direct contact condensation in a T-junction with porous inner-structures,” *Int. J. Heat Mass Transf.*, vol. 168, p. 120863, Apr. 2021, doi: 10.1016/j.ijheatmasstransfer.2020.120863.

[9] A. Petrovic de With, R. K. Calay, and G. de With, “Three-dimensional condensation regime diagram for direct contact condensation of steam injected into water,” *Int. J. Heat Mass Transf.*, vol. 50, no. 9, pp. 1762–1770, May 2007, doi: 10.1016/j.ijheatmasstransfer.2006.10.017.

[10] Z. R. Alden, G. D. Maples, K. M. Dressler, G. F. Nellis, and A. Berson, “Plume Stability During Direct Contact Condensation of Steam in a Crossflow of Subcooled Water, at High Mass Flux and With a Small Nozzle Diameter,” *J. Heat Transf.*, vol. 143, no. 9, Jul. 2021, doi: 10.1115/1.4051667.

[11] Q. Zhao and T. Hibiki, “Review: Condensation regime maps of steam submerged jet condensation,” *Prog. Nucl. Energy*, vol. 107, pp. 31–47, Aug. 2018, doi: 10.1016/j.pnucene.2017.12.014.

[12] S. Zare, M. H. Jamalkhoo, and M. Passandideh-Fard, “Experimental study of direct contact condensation of steam jet in water flow in a vertical pipe with square cross section,” *Int. J. Multiph. Flow*, vol. 104, pp. 74–88, Jul. 2018, doi: 10.1016/j.ijmultiphaseflow.2018.03.009.

[13] Q. Xu, L. Guo, S. Zou, J. Chen, and X. Zhang, “Experimental study on direct contact condensation of stable steam jet in water flow in a vertical pipe,” *Int. J. Heat Mass Transf.*, vol. 66, pp. 808–817, Nov. 2013, doi: 10.1016/j.ijheatmasstransfer.2013.07.083.

[14] P. Datta *et al.*, “Experimental investigation on the effect of initial pressure conditions during steam-water direct contact condensation in a horizontal pipe geometry,” *Int. Commun. Heat Mass Transf.*, vol. 121, p. 105082, Feb. 2021, doi: 10.1016/j.icheatmasstransfer.2020.105082.

[15] S. R. Yang, J. Seo, and Y. A. Hassan, “Thermal hydraulic characteristics of unstable bubbling of direct contact condensation of steam in subcooled water,” *Int. J. Heat Mass Transf.*, vol. 138, pp. 580–596, Aug. 2019, doi: 10.1016/j.ijheatmasstransfer.2019.04.065.

[16] A. Quddus *et al.*, “Experimental study on steam plume shape characteristics for bevelled spray nozzles exhausting into quiescent water,” *Nucl. Eng. Des.*, vol. 394, p. 111824, Aug. 2022, doi: 10.1016/j.nucengdes.2022.111824.

[17] D. Lu *et al.*, “Experimental research on the characteristics of steam jet condensation in subcooled water through a double-hole nozzle in one direction,” *Ann. Nucl. Energy*, vol. 151, p. 107898, Feb. 2021, doi: 10.1016/j.anucene.2020.107898.

[18] D. Chong, Q. Zhao, F. Yuan, W. Wang, W. Chen, and J. Yan, “Research on the steam jet length with different nozzle structures,” *Exp. Therm. Fluid Sci.*, vol. 64, pp. 134–141, Jun. 2015, doi: 10.1016/j.expthermflusci.2015.02.015.

[19] C. K. Chan and C. K. B. Lee, “A regime map for direct contact condensation,” *Int. J. Multiph. Flow*, vol. 8, no. 1, pp. 11–20, Feb. 1982, doi: 10.1016/0301-9322(82)90003-9.

[20] Q. Xu, L. Guo, and L. Chang, “Mechanisms of pressure oscillation in steam jet condensation in water flow in a vertical pipe,” *Int. J. Heat Mass Transf.*, vol. 110, pp. 643–656, Jul. 2017, doi: 10.1016/j.ijheatmasstransfer.2017.03.017.

[21] T. R. Boziuk, M. K. Smith, and A. Glezer, “Acoustic enhancement of direct-contact condensation using capillary waves,” *Int. J. Heat Mass Transf.*, vol. 138, pp. 357–372, Aug. 2019, doi: 10.1016/j.ijheatmasstransfer.2019.04.028.

[22] W. Li, Z. Meng, J. Wang, and Z. Sun, “Effect of non-condensable gas on pressure oscillation of submerged steam jet condensation in condensation oscillation regime,” *Int. J. Heat Mass Transf.*, vol. 124, pp. 141–149, Sep. 2018, doi: 10.1016/j.ijheatmasstransfer.2018.03.068.

[23] Q. Xu, S. Ye, Y. Chen, Q. Chen, and L. Guo, “Condensation regime diagram for supersonic and subsonic steam jet condensation in water flow in a vertical pipe,” *Appl. Therm. Eng.*, vol. 130, pp. 62–73, Feb. 2018, doi: 10.1016/j.applthermaleng.2017.10.135.

[24] Q. Zhao, W. Chen, L. Wang, D. Chong, and J. Yan, “Experimental investigation on pressure oscillations of steam jet condensation through multi-holes,” *Int. J. Heat Mass Transf.*, vol. 132, pp. 662–670, Apr. 2019, doi: 10.1016/j.ijheatmasstransfer.2018.12.042.

[25] W. Sangsom and C. Inprasit, “Design Parameters on Impingement Steam Jet Heat Transfer of Continuous Liquid Food Sterilization,” *Fluids*, vol. 7, no. 6, p. 185, May 2022, doi: 10.3390/fluids7060185.

[26] C. Jimenez-Junca, A. Sher, J.-C. Gumy, and K. Niranjan, “Production of milk foams by steam injection: The effects of steam pressure and nozzle design,” *J. Food Eng.*, vol. 166, pp. 247–254, Dec. 2015, doi: 10.1016/j.jfoodeng.2015.05.035.

[27] W. Wang, F. Yuan, Q. B. Zhao, D. T. Chong, W. X. Chen, and J. J. Yan, “Experimental study on the submerged steam jet through side hole nozzle,” *IOP Conf. Ser. Mater. Sci. Eng.*, vol. 88, p. 012029, Sep. 2015, doi: 10.1088/1757-899X/88/1/012029.

[28] Y. Zhou and Y. Li, “Molecular dynamics simulation of kinetic boundary conditions and evaporation/condensation coefficients of direct-contact condensation in two-phase jet,” *AIP Adv.*, vol. 12, no. 5, p. 055010, May 2022, doi: 10.1063/5.0092010.

[29] S. S. Gulawani, J. B. Joshi, M. S. Shah, C. S. RamaPrasad, and D. S. Shukla, “CFD analysis of flow pattern and heat transfer in direct contact steam condensation,” *Chem. Eng. Sci.*, vol. 61, no. 16, pp. 5204–5220, Aug. 2006, doi: 10.1016/j.ces.2006.03.032.

[30] S. Q. Li, P. Wang, and T. Lu, “CFD based approach for modeling steam–water direct contact condensation in subcooled water flow in a tee junction,” *Prog. Nucl. Energy*, vol. 85, pp. 729–746, Nov. 2015, doi: 10.1016/j.pnucene.2015.09.007.

[31] I. Gallego-Marcos *et al.*, “Pool stratification and mixing induced by steam injection through spargers: CFD modelling of the PPOOLEX and PANDA experiments,” *Nucl. Eng. Des.*, vol. 347, pp. 67–85, Jun. 2019, doi: 10.1016/j.nucengdes.2019.03.011.

[32] G. Patel, V. Tanskanen, E. Hujala, and J. Hyvärinen, “Direct contact condensation modeling in pressure suppression pool system,” *Nucl. Eng. Des.*, vol. 321, pp. 328–342, Sep. 2017, doi: 10.1016/j.nucengdes.2016.08.026.

[33] A. Khan, K. Sanaullah, M. S. Takriff, H. Zen, and L. S. Fong, “Inclined Injection of Supersonic Steam into Subcooled Water: A CFD Analysis,” *Adv. Mater. Res.*, vol. 845, pp. 101–107, Dec. 2013, doi: 10.4028/www.scientific.net/AMR.845.101.

[34] B. G. Jeon, S. U. Ryu, and D. J. Euh, “CFD analysis of steam jet injection in a hybrid SIT,” *Ann. Nucl. Energy*, vol. 115, pp. 126–137, May 2018, doi: 10.1016/j.anucene.2018.01.016.

[35] S. Saraiva de Lira Araújo and O. J. Romero, “A CFD study of steam injection tubing heat losses,” *Ingeniare Rev. Chil. Ing.*, vol. 27, no. 4, pp. 600–612, Dec. 2019, doi: 10.4067/S0718-33052019000400600.

[36] R. Gharibshahi, A. Jafari, and H. Ahmadi, “CFD investigation of enhanced extra-heavy oil recovery using metallic nanoparticles/steam injection in a micromodel with random pore distribution,” *J. Pet. Sci. Eng.*, vol. 174, pp. 374–383, Mar. 2019, doi: 10.1016/j.petrol.2018.10.051.

[37] T. Patureaux and D. Barthod, “Usage of Cfd Modelling for Improving an Fcc Riser Operation,” *Oil Gas Sci. Technol.*, vol. 55, no. 2, pp. 219–225, Mar. 2000, doi: 10.2516/ogst:2000014.

[38] E. Hujala, V. Tanskanen, and J. Hyvärinen, “Pattern recognition algorithm for analysis of chugging direct contact condensation,” *Nucl. Eng. Des.*, vol. 332, pp. 202–212, Jun. 2018, doi: 10.1016/j.nucengdes.2018.03.032.

Appendix 1: Xray Scans for Shock location and Manufacturing Study

For both the shock location and manufacturing study all of the nozzles were scanned and the results of those scans are detailed below in table 2.

Table 2: Nozzle Xray Scans for Thesis

Nozzle	**Geometrical Area Ratio**	**Nozzle Features**	**Nozzle Scans**	**Zoomed In and Threshold Applied (orifice only)**
Converging	1	No noticeable burrs or defects in the nozzle	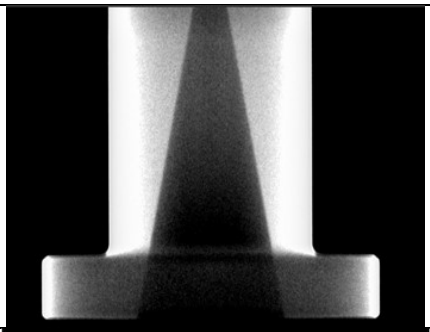	
2S	1.20	Small converging inlet and a small diverging outlet.	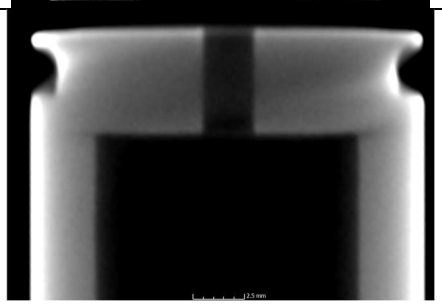	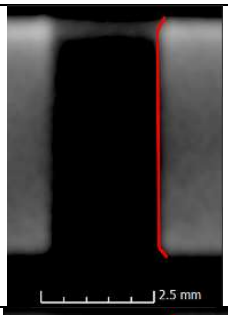
2-2S	2.14	Inlet Burr and large Diverging outlet chamfer	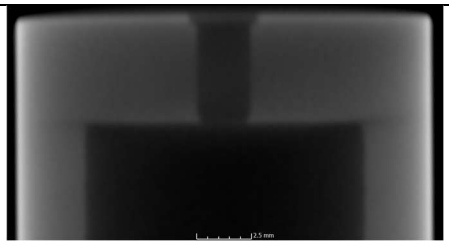	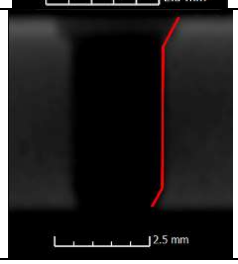

2SE	1	No noticeable burrs or defects in the nozzle		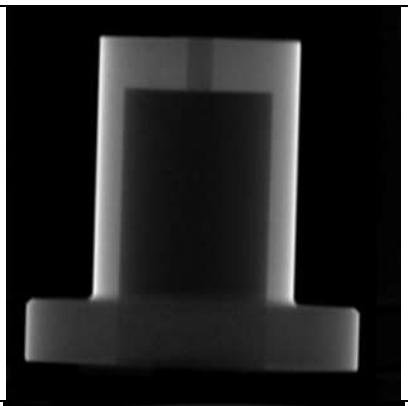	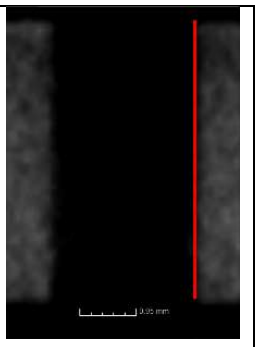
2CD	1.50	No noticeable burrs or defects in the nozzle		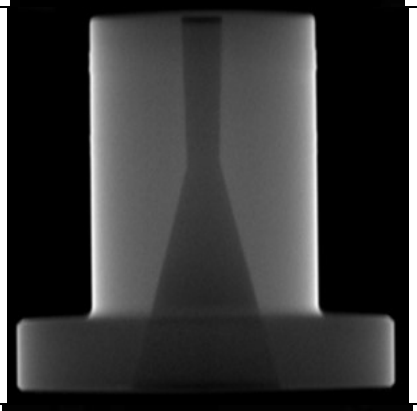	
5CD	3.67	No noticeable burrs or defects in the nozzle		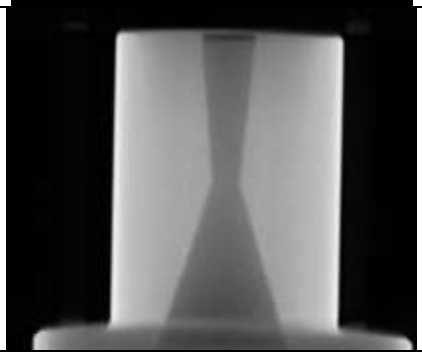	

Appendix 2: Converging Nozzle Inlet Pressure vs Pressure Ratio Study

This study focused on determining whether the pressure ratio or inlet pressure had more of an impact on the stability of DCC. The rationale behind this decision is that a converging nozzle will at most have an exit Mach of 1 and thus the flow should be able to be calculated easily with both simple 1D and 2D models. The geometry of this converging nozzle is depicted previously in Figure 37. Using this nozzle, the effect of both the steam inlet pressure and the pressure ratio was studied by taking 16 tests at inlet pressures varying from steam inlet pressures ranging from 50-80 PSIG and pressure ratios from 0.3-0.65. To represent the data from this study the regime at each temperature is mapped for all the test conditions with the steam pressure and pressure ratio on the y axis in Figure 44 (note: older regime map as this was done before automation).

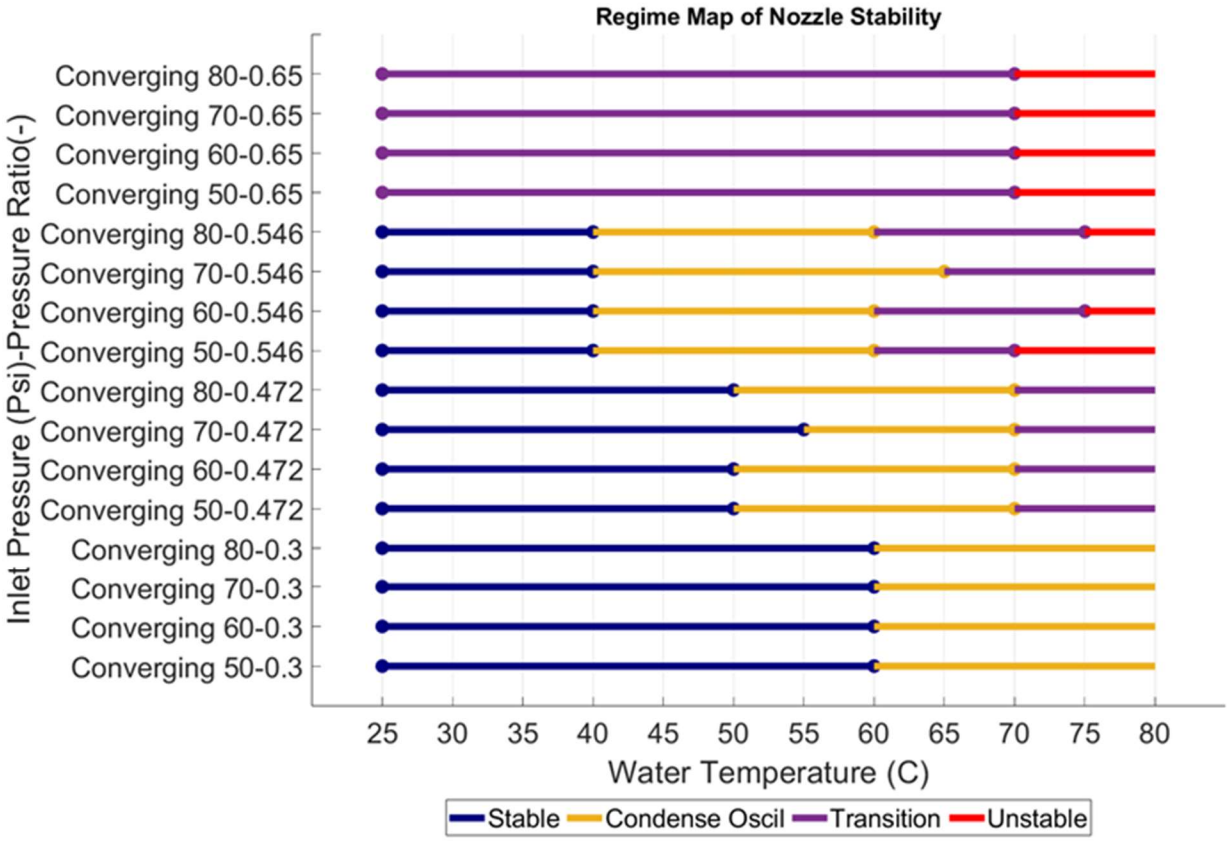

Figure 44: Regime Map for Converging Pressure Study

In the regime map in Figure 44 the different pressure ratios are grouped together and increase from bottom to top. By grouping the data points by pressure ratio, it becomes clear that the pressure ratio used is the dominant variable of the two investigated by this early study. This can be seen when looking at how at 0.3, 0.472, and 0.65 pressure ratios there is no change in how the nozzle performs at different temperatures as the inlet pressure is increased and at 0.546 there is only a slight difference between the different steam pressures. What is affected by the steam inlet pressure is the mass flow through the nozzle as depicted below in Figure 45.

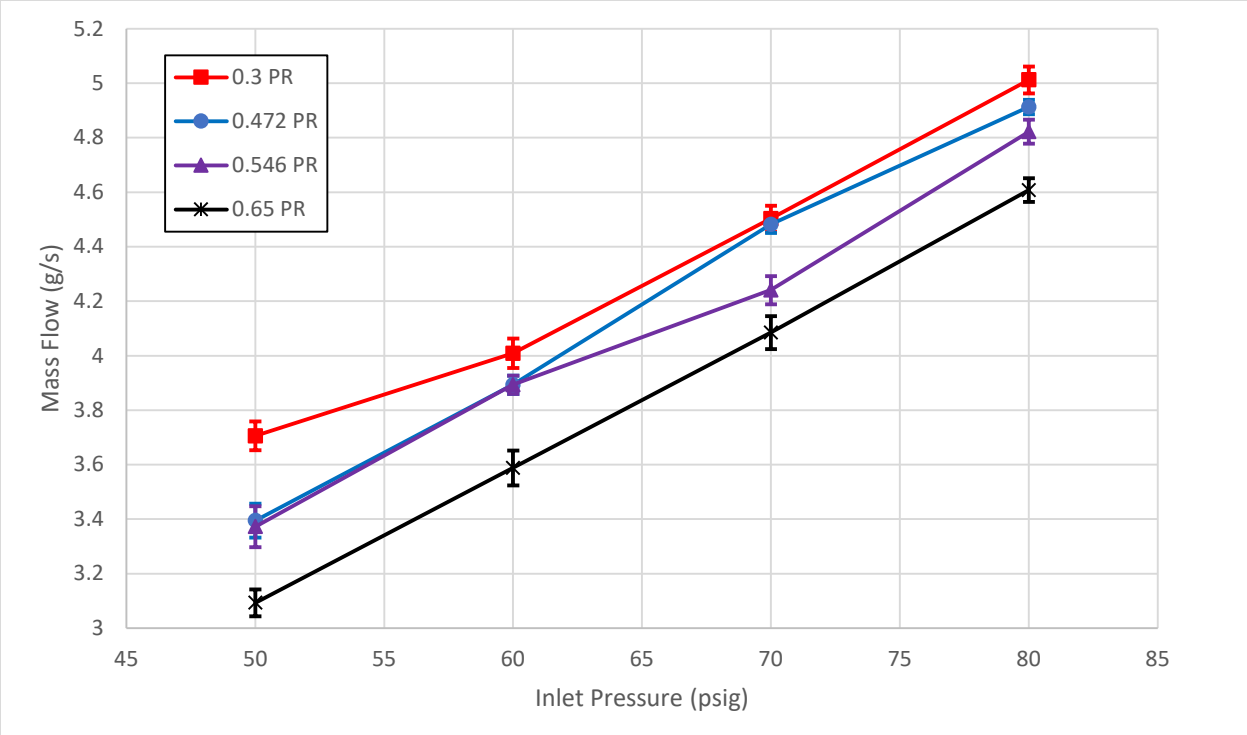

Figure 45: Mass flow vs Inlet Pressure and Pressure Ratio

The mass flow plot illustrates that the dominant variable in determining the mass flow for the experimental setup is the inlet pressure and the pressure ratio itself plays a much smaller role in comparison. Additionally, when comparing the results in Figure 45 to the results of the regime map in Figure 44 the conclusion can be drawn that the mass flow has little to no effect on the stability of the plume for at least for the experimental apparatus and conditions studied in this thesis. To further understand why the mass flow might not influence stability the Mach contours for the simulations ran at a constant pressure ratio were put together in Figure 46 to illustrate the effect that increasing inlet pressure has on the flow of steam.

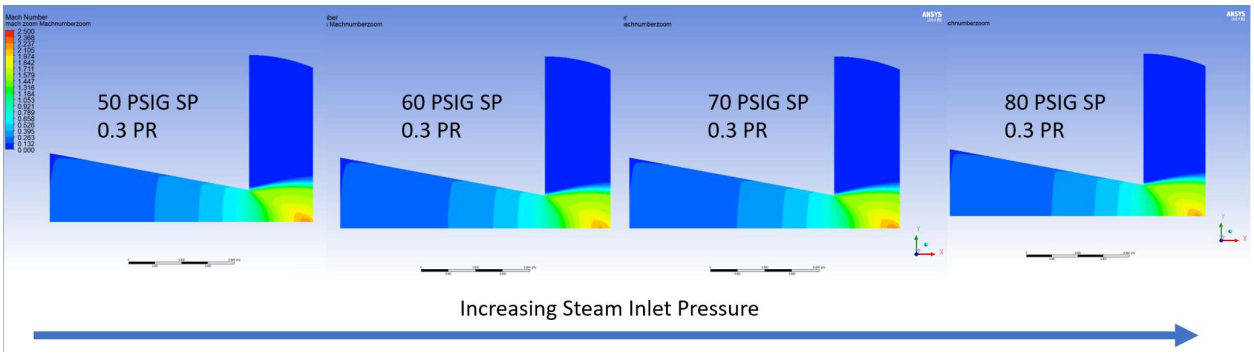

Figure 46: Mach contours for increasing inlet pressure for converging nozzle study.

The contours in Figure 46 illustrate the lack of change in the flow profile when increasing steam pressure. All the contours show a shock downstream of the nozzle outlet at the same location. The only major difference between the simulations was the mass flow which came close to matching the experimental results seen in Figure 45. Moving onto studying the effect of the pressure ratio the Mach contours were put together in Figure 47.

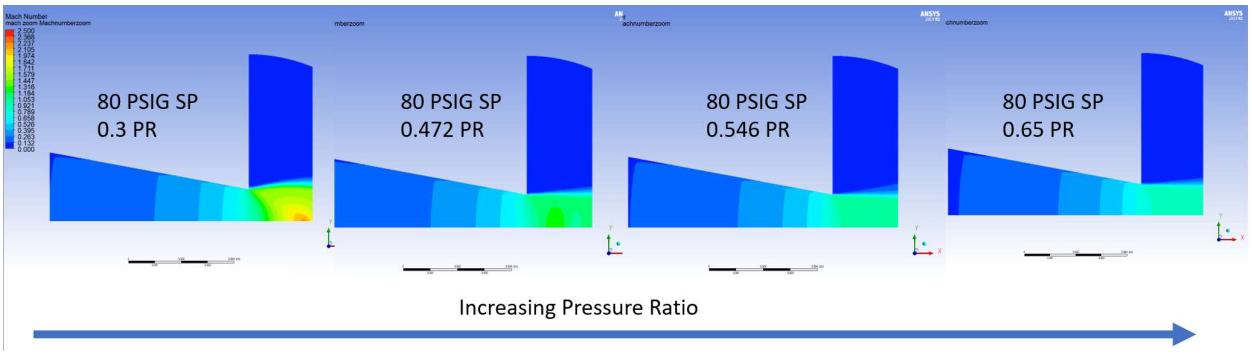

Figure 47: Mach Contours for increasing pressure ratio at a constant inlet pressure.

In contrast to Figure 46 the change in pressure ratio has a much larger impact on the flow field of the steam through the nozzle. This trend is illustrated with the decrease in Mach number as the pressure ratio with the flow becoming subsonic as the it continues towards the right. This trend was also noticed with other inlet pressures as their pressure ratios were

increased. Comparing the CFD results to the experimental regime map suggests a correlation between pressure ratio and the stability of a plume in a direct contact condensation application.

Appendix 3: LD Study

This study focused on different LD nozzles with an emphasis on looking at only the LD without any influence from manufacturing defects. To avoid defects, all nozzles were manufacturing with EDM. For each LD nozzle, data was taken at 4 different pressure ratios and 12 different temperatures. In total there were 9 nozzles manufactured. The nozzle geometry used for this study is the same found in Figure 40 but the orifice length was decreased and increased. A contour map for the 0.58 Pressure ratio is found below in Figure 48 with the LD ratio as the y axis rather than pressure ratio.

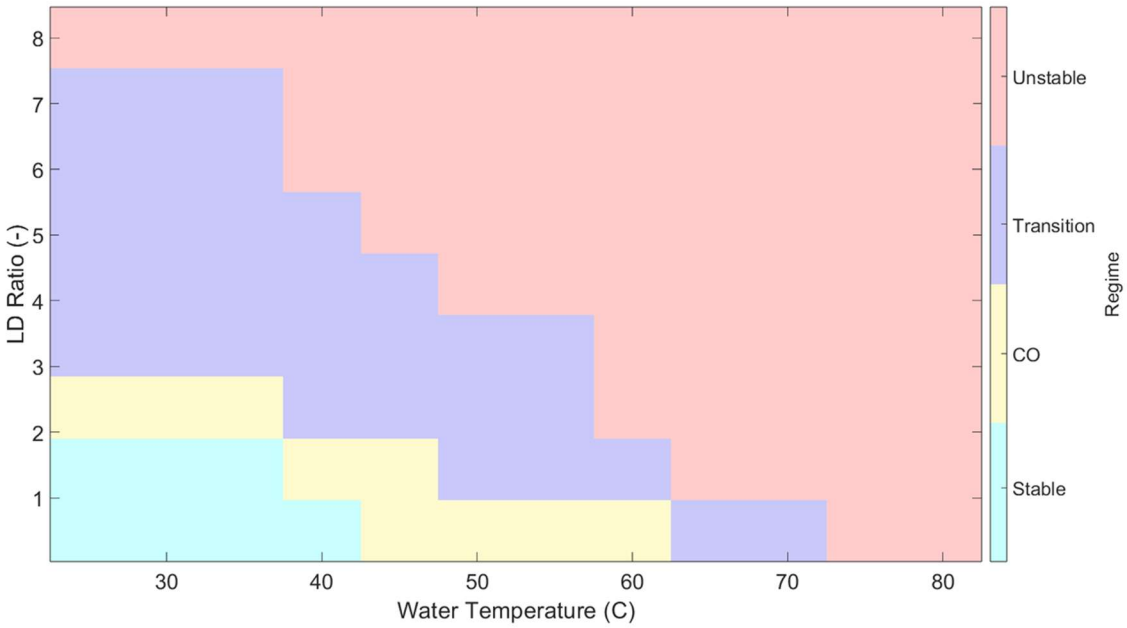

Figure 48: LD Regime Map for 0.58 PR

Looking at the trends in Figure 49 illustrates that a smaller LD nozzle will result in a more stable nozzle. Decreasing the pressure ratio to 0.48 we see a similar trend as depicted in Figure 49.

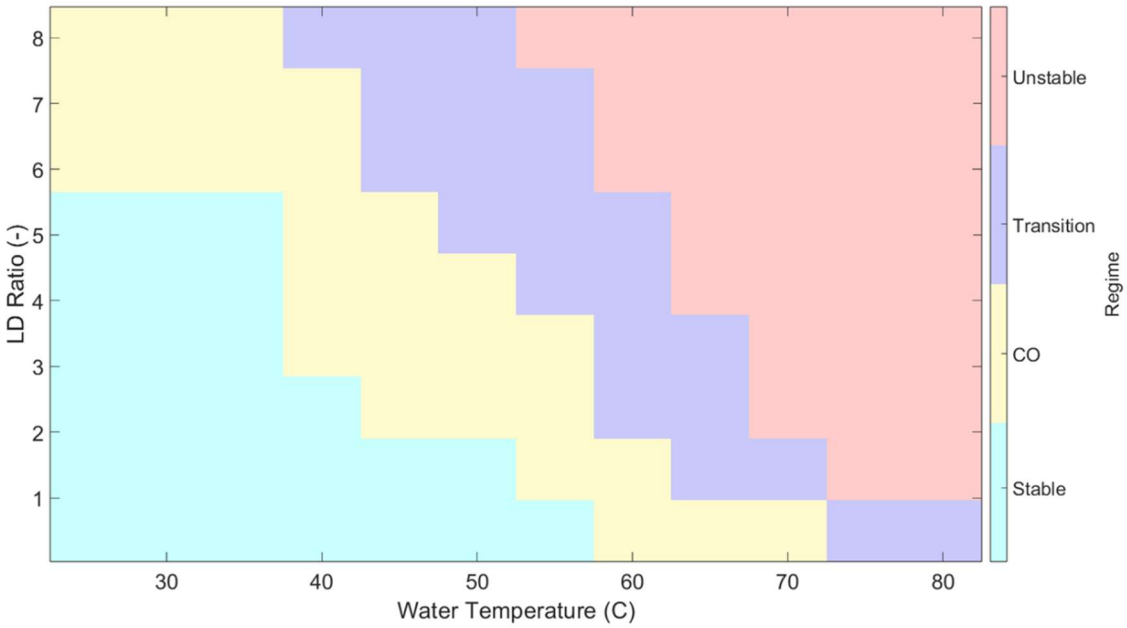

Figure 49: LD Regime Map for 0.48 PR

Like what was seen in the previous studies, a lower pressure ratio has a more stable nozzle. Additionally, there is a continued trend for the LD ratio demonstrated in Figure 49. Two other PRs are shown in Figure 50 and 51. There is a slight trend correlating the LD ratio to stability but it is not as strong as seen in Figures 48 and 49.

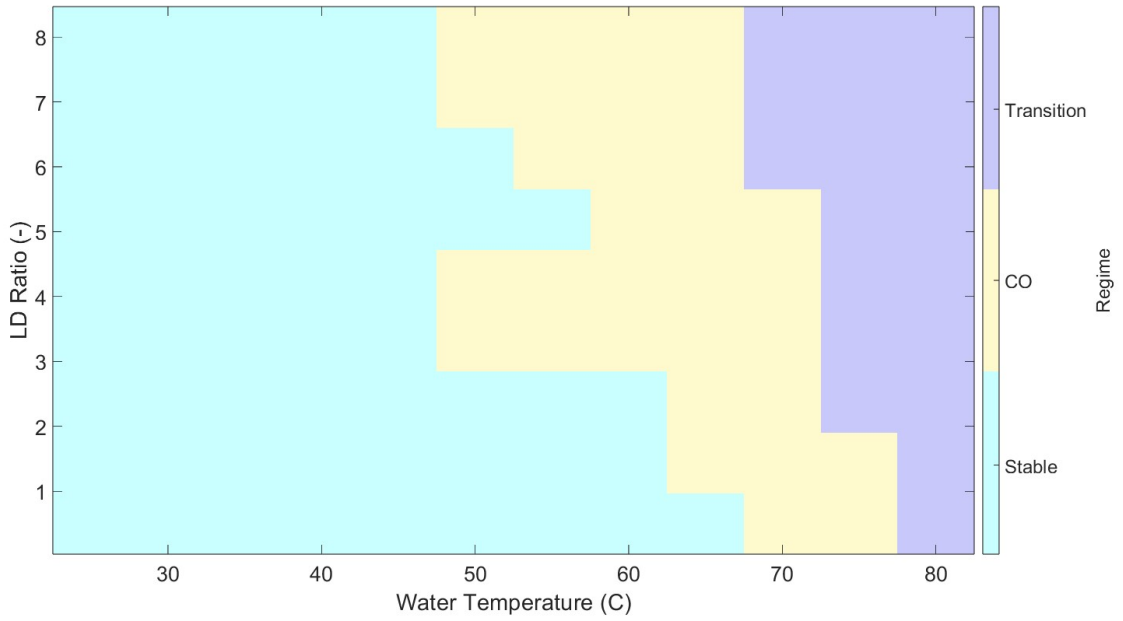

Figure 50: LD Regime Map for 0.36 PR

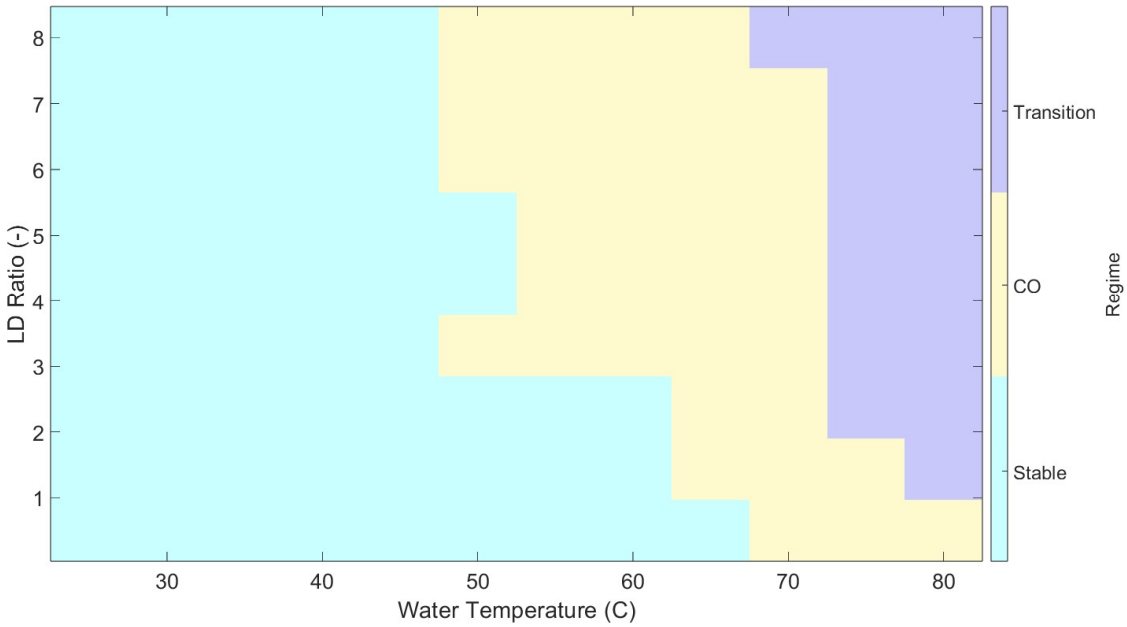

Figure 51: LD Regime Map for 0.26 PR

To look at how the LD affected the Mach contours, simulation results for each Nozzle are shown in Figure 52 going from shortest to longest nozzle tested in this study.

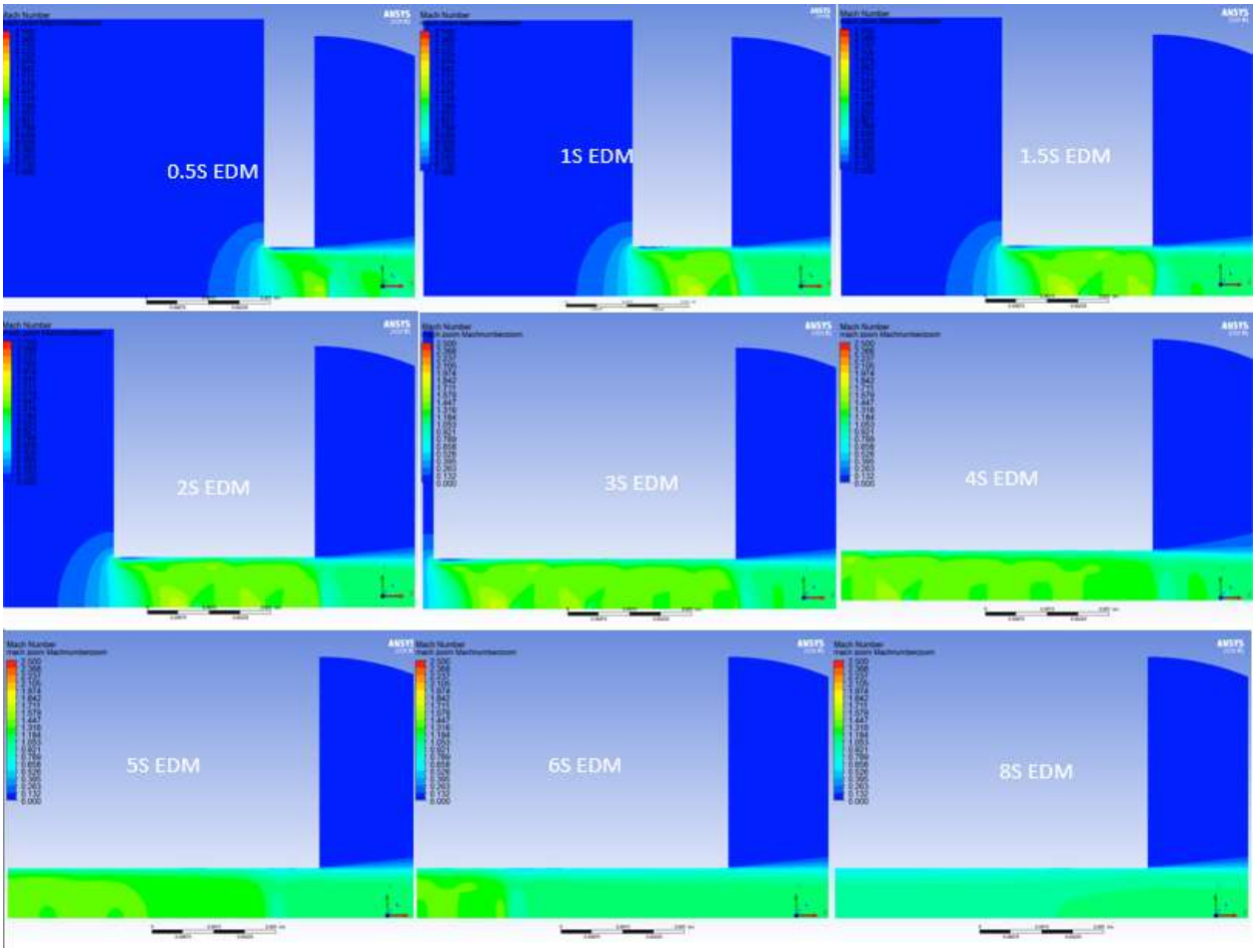

Figure 52: Mach Contour progression (1S left,3S center, 5S right) at 0.48 PR

To get a better visual representation in the differences in shock location between each LD a select amount of the centerline Mach number CFD results (to reduce visual clutter) were plotted below in Figure 53.

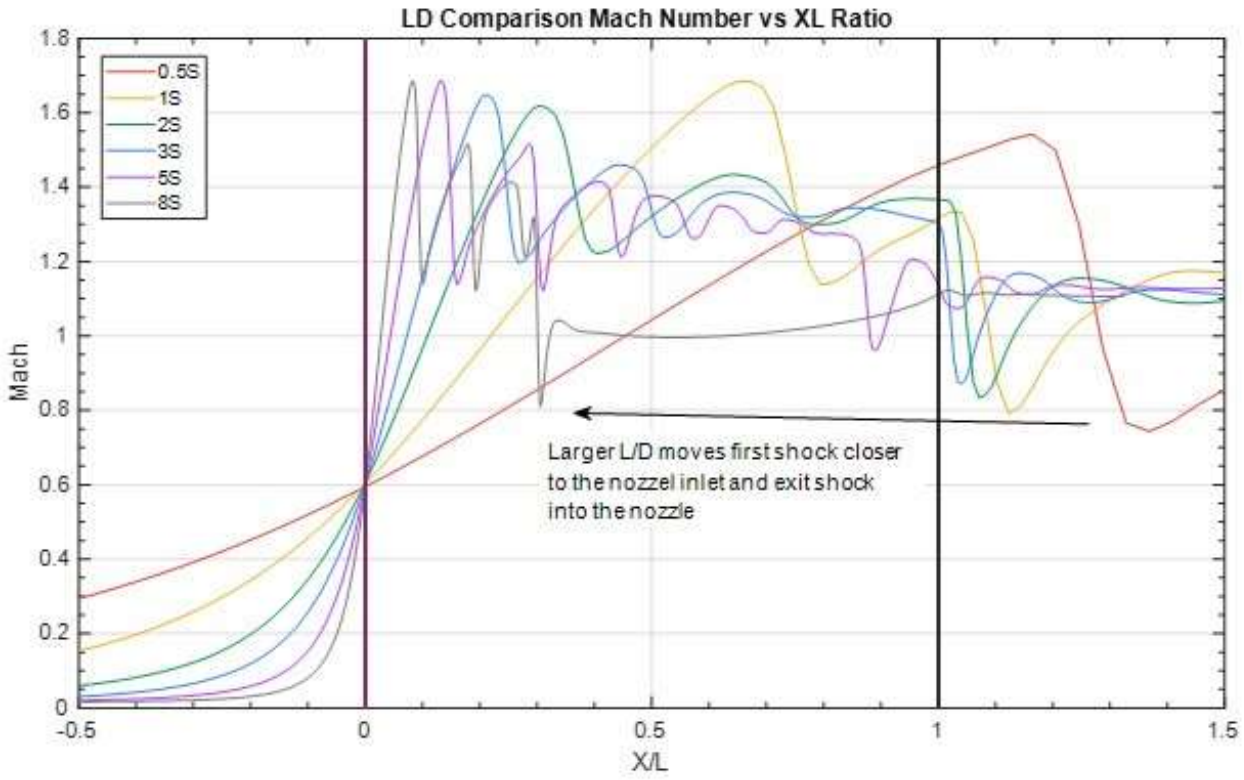

Figure 53: Mach Number Plot versus position over orifice length for LD Study at 0.48 PR

Figure 53 displays how increasing the LD at 0.48 pushes the shock further inside the nozzle. The shock location study would suggest that this trend would result in a more unstable nozzle which was seen in the regime maps in Figures 48 - 51. Finally, the mass flow for all of the tests taken can be found below.

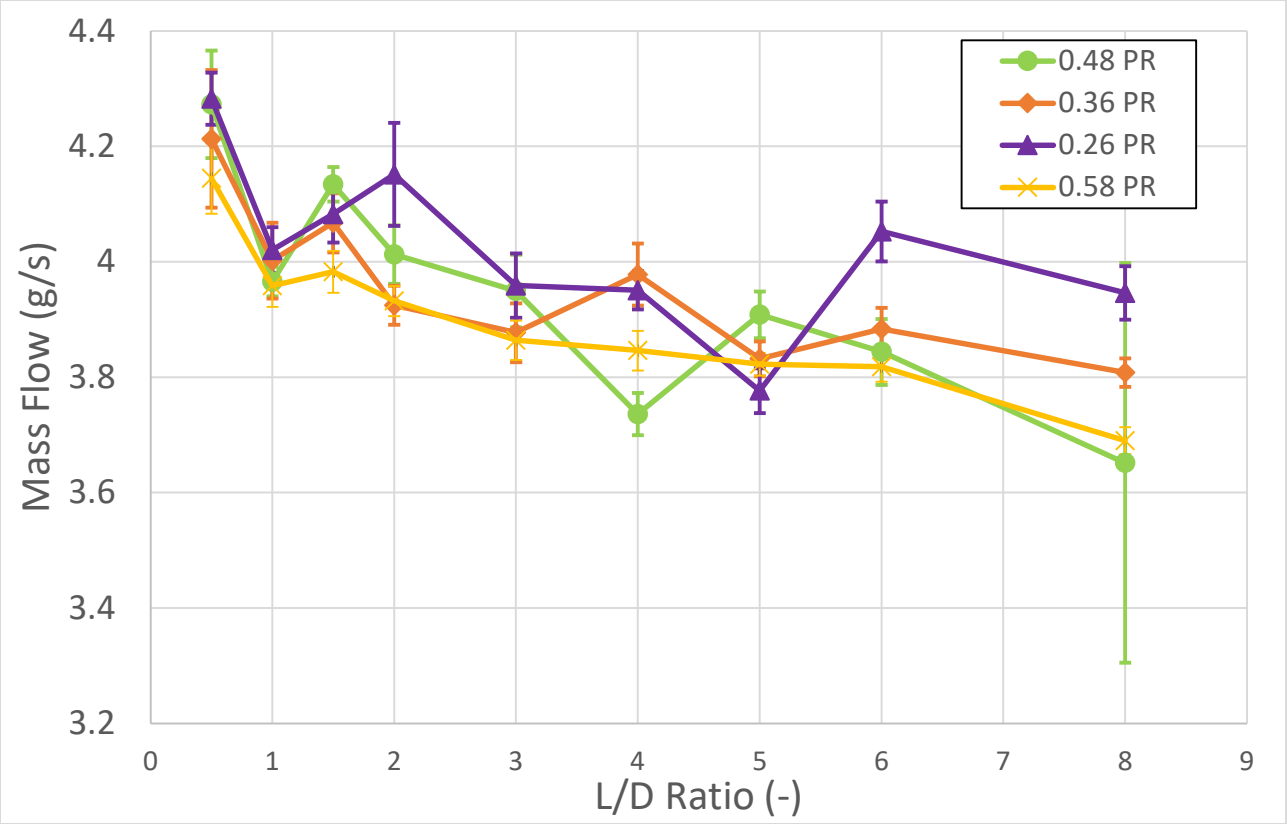

Figure 54: Mass flow of L/D Ratio Study

Below in Table 3 is a collection of all the nozzle scans taken of the EDM straight nozzles for the LD study.

Table 3: Nozzle Scans of LD Nozzles

Nozzle	**Nozzle Scans**	**Zoomed In**
0.5S	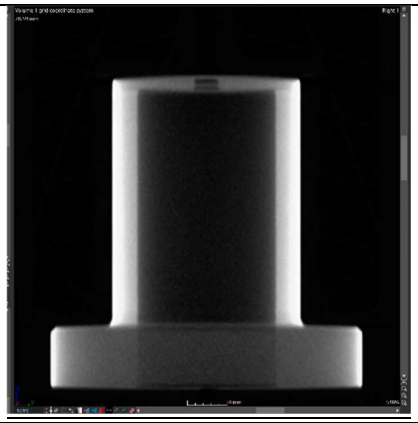	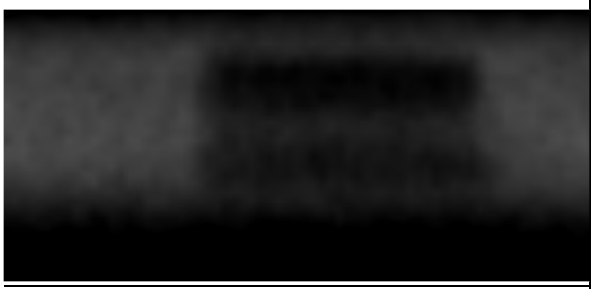

1S	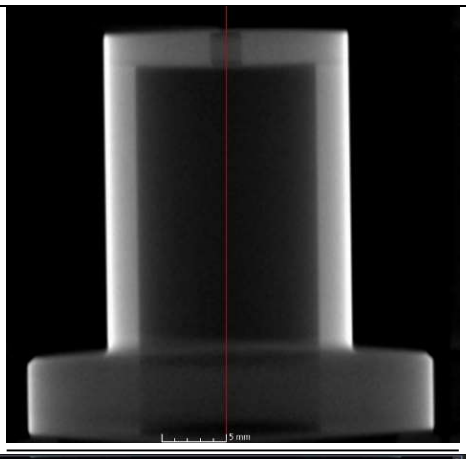	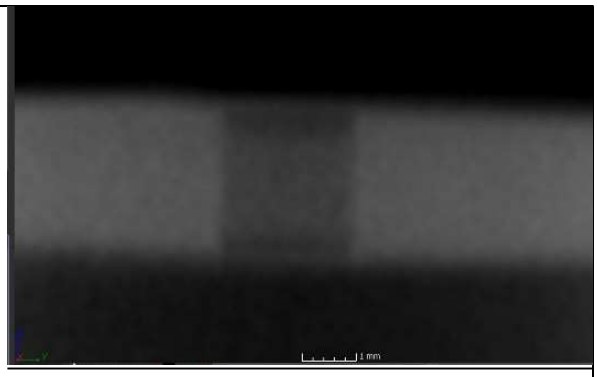
1.5S	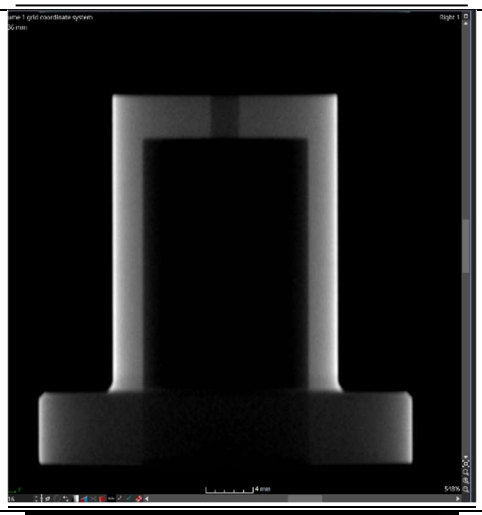	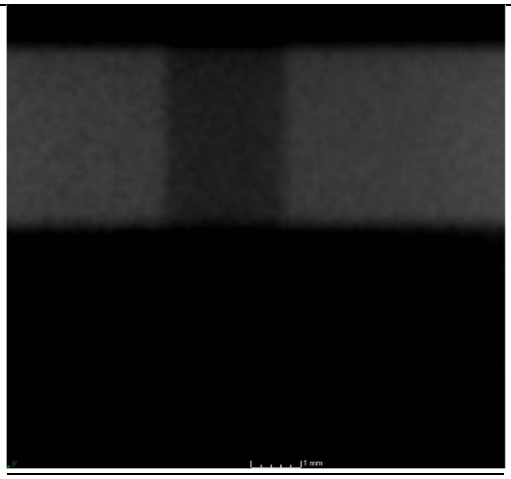
2SE	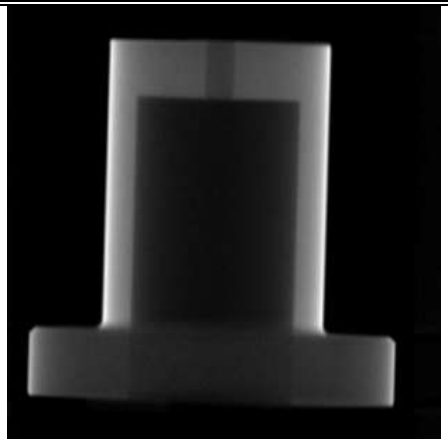	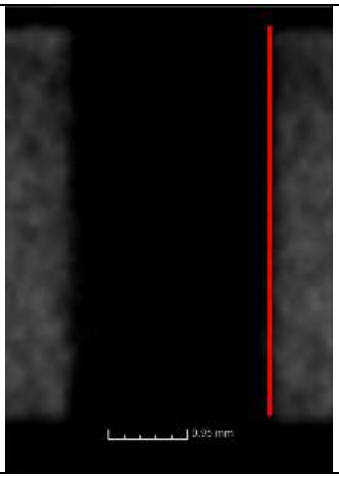

3S	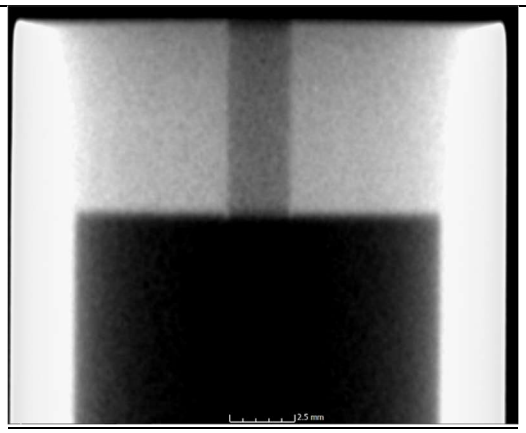	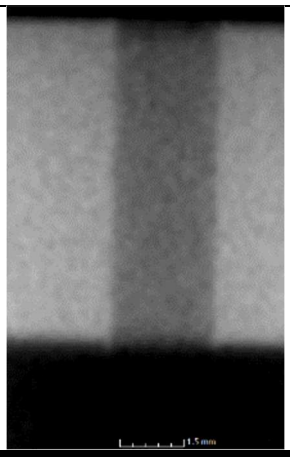
4S		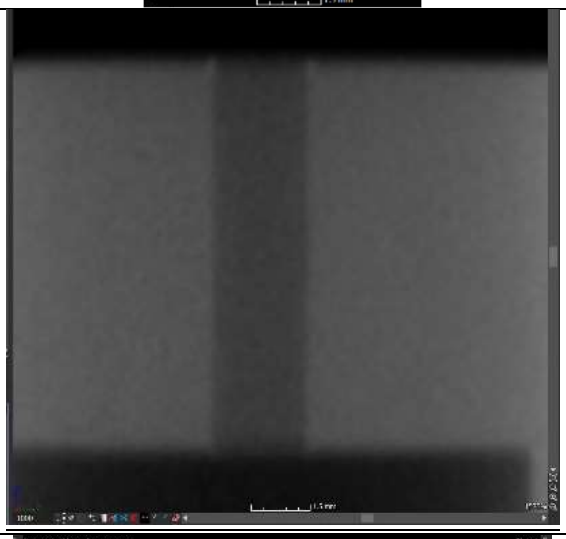
5S	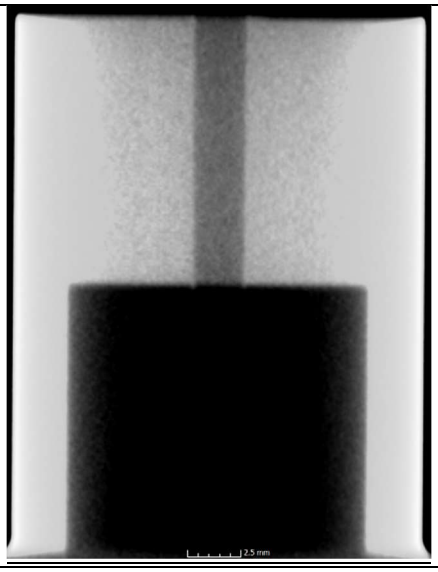	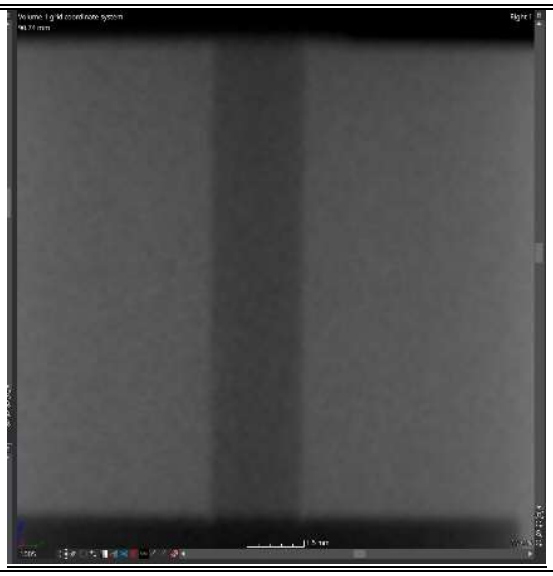

6S	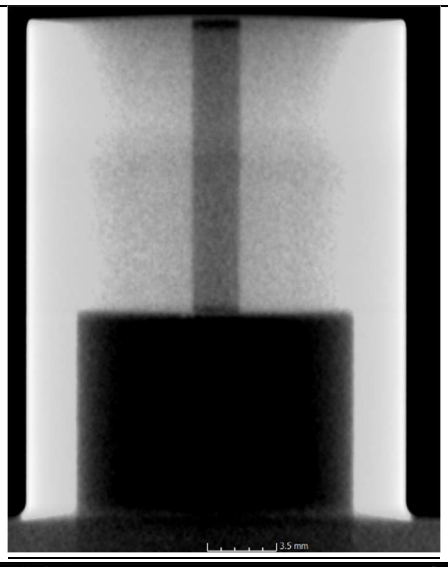	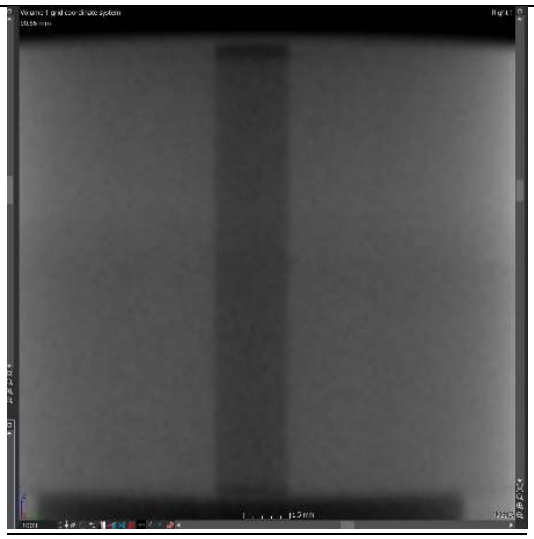
8S	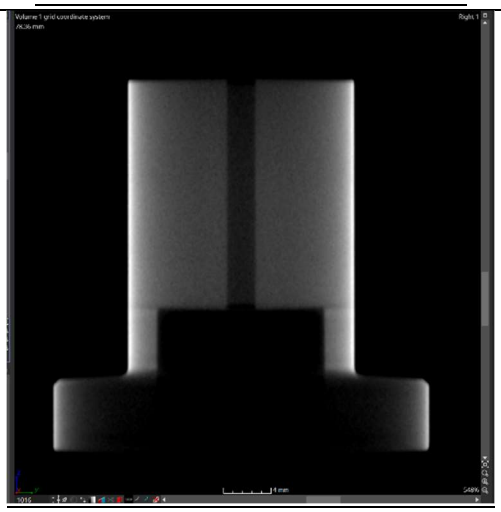	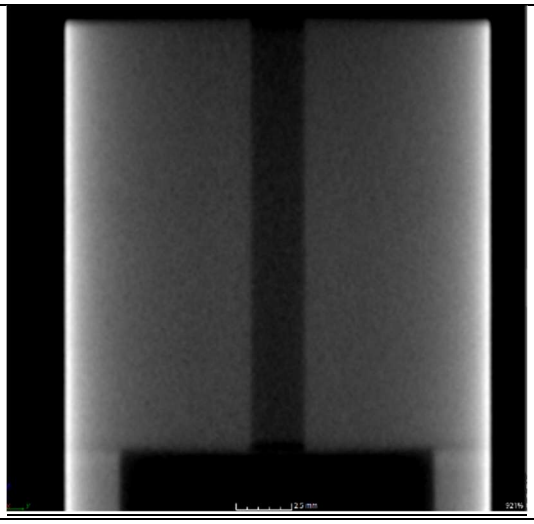

Appendix 4: Diameter Study

This study aimed to expand on the converging and LD study to further understand the effect of increased mass flow on both the noise and the stability of a DCC application. For this study 5 nozzles were tested each with different diameters while keeping the LD ratio constant at 1. The dimensions for these nozzles have the same exterior dimensions as the 2S nozzle in Figure 40 but the ID and orifice length change with a LD ratio of 1 being kept for all of them. All of the nozzles were tested at a inlet pressure of 70 psig to ensure that the steam generator was able to supply enough mass flow safely for the largest nozzles tested. To maintain a pressure ratio close to the one most used in past experiments the water pressure was maintained at 25 psig. The mass flow results for both the experimental and simulated studies are found below in Figure 55.

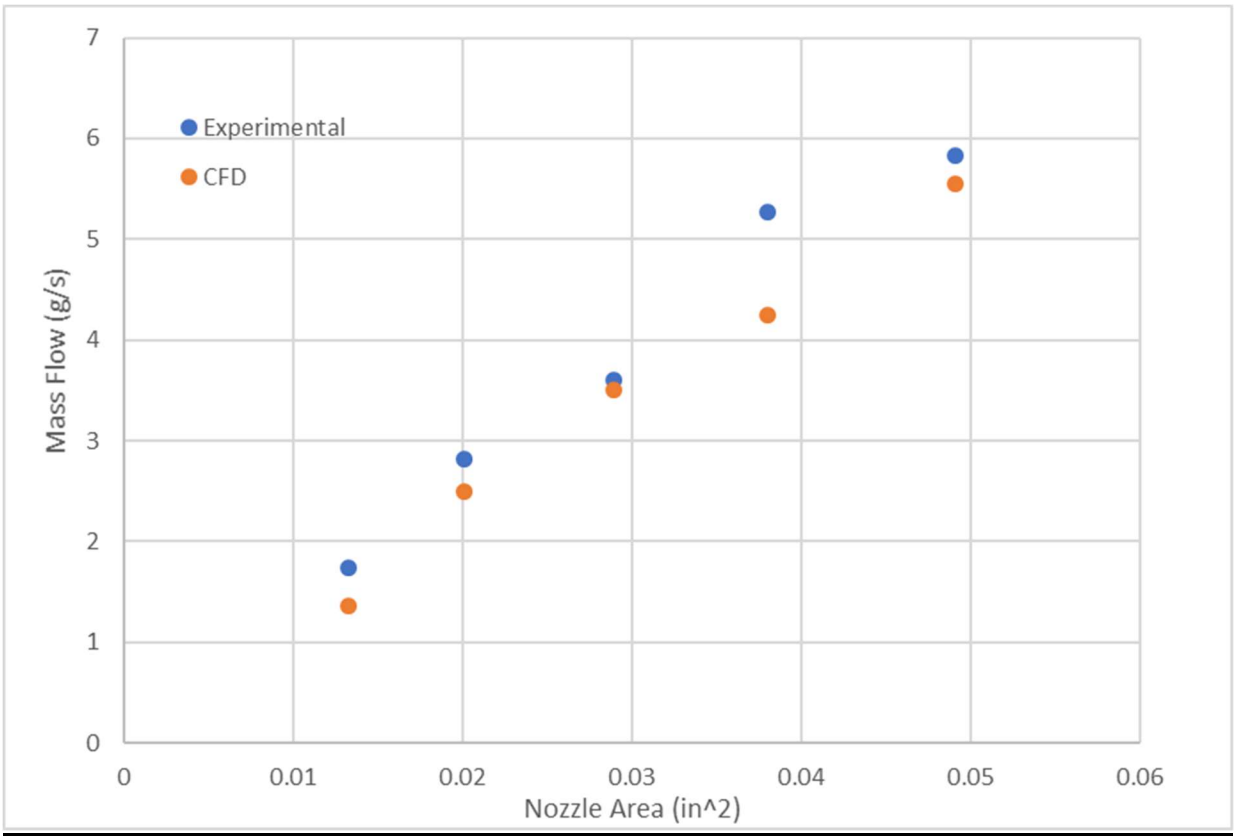

Figure 55: Mass Flow Rate Results for Diameter Study

Part of this study added a decibel meter (REED R8080) a meter away from the test section to capture readings that are applicable to the ones that may be measured in the field by onsite inspectors using a standardized distance. For all the nozzles tested in this study the decibel level in dba was measured at each temperature and the results are found in Figure 56.

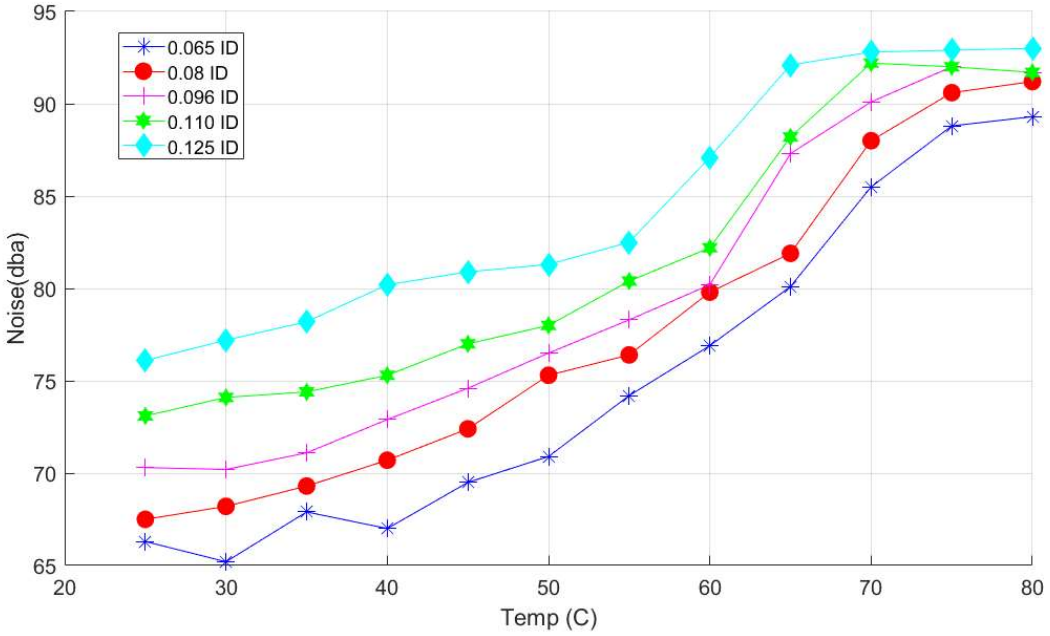

Figure 56: Decibel Results for Diameter Study

It appears based on these results that having a larger diameter and mass flow will increase the level of noise produced by the steam plume. To look at how the diameter impacts the stability of the nozzle a regime map using nozzle diameter and water temperature as its axis is below in Figure 57.

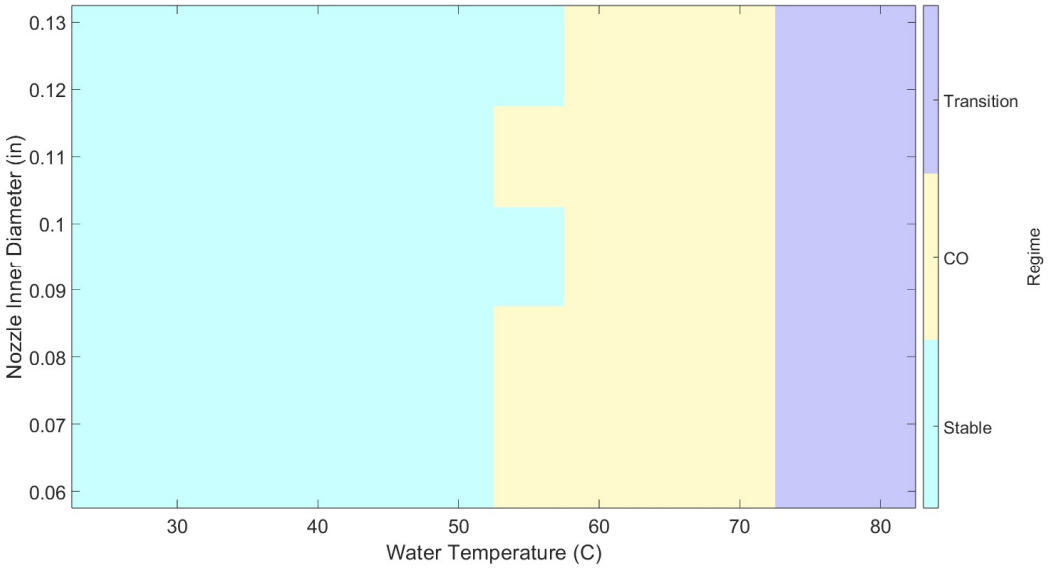

Figure 57: Regime Map for Diameter Study

There is little to no change in the regimes as the diameter increased. To see how the flow is affected by diameter the Mach contours at 0.48 PR were simulated and placed below in Figure 57. These results show that there is little change in the shock location inside the nozzle as the diameter is increases, which is expected based on the stability results.

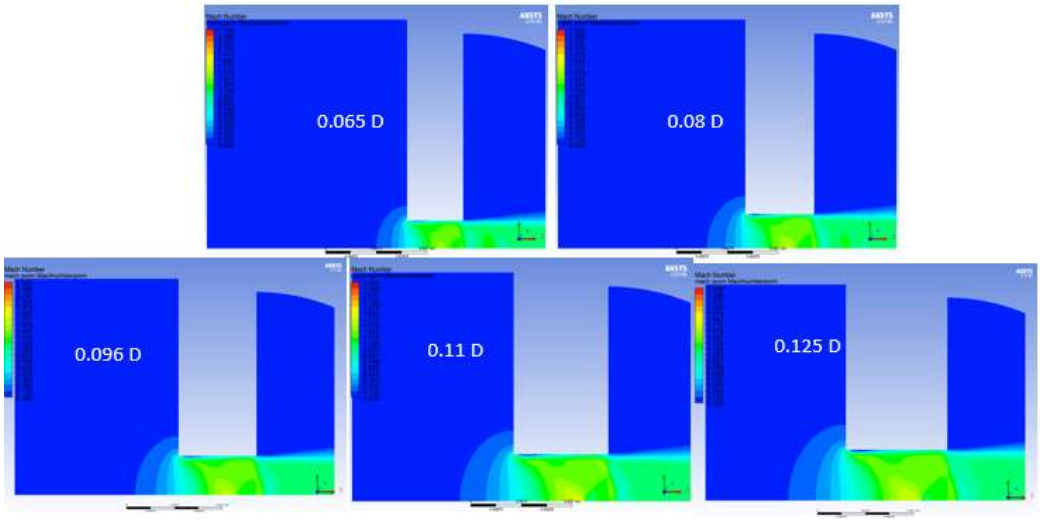

Figure 58: Mach Contour progression examples at 0.48 PR

Each of the nozzles were scanned to identify any manufacturing defects. Images of the scans are placed below in Table 4. The EDM process produced consistent straight nozzles, but there were some issues in imaging the smallest ones with the available X-ray scanner (1500 W Comet x-ray source, & 1621 Perkin-Elmer scintillation detector).

Table 4: Nozzle Scans for Diameter Study

Nozzle	**Nozzle Scans**	**Nozzle Scans Zoomed In**
1S 0.65 ID	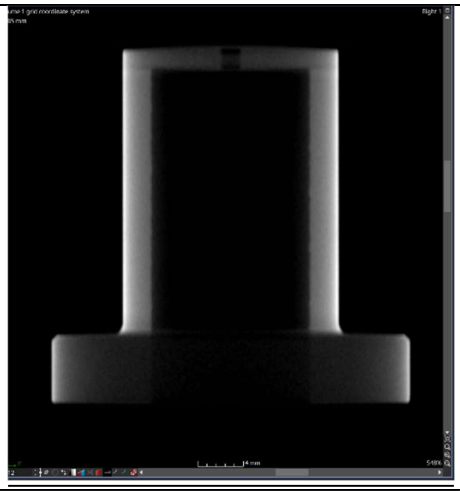	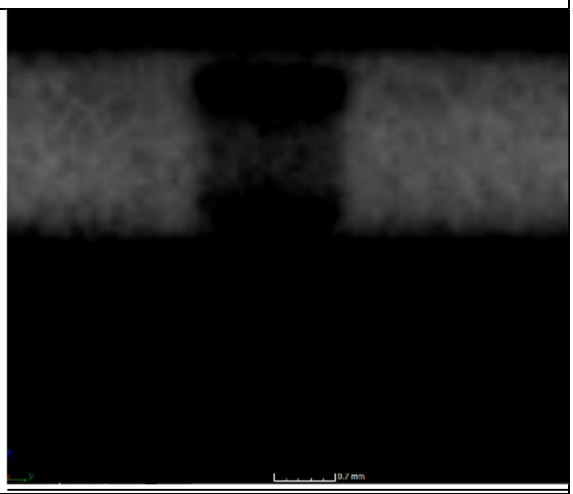
1S 0.080 ID	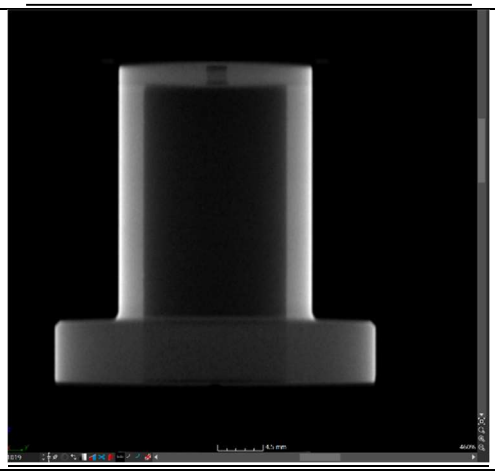	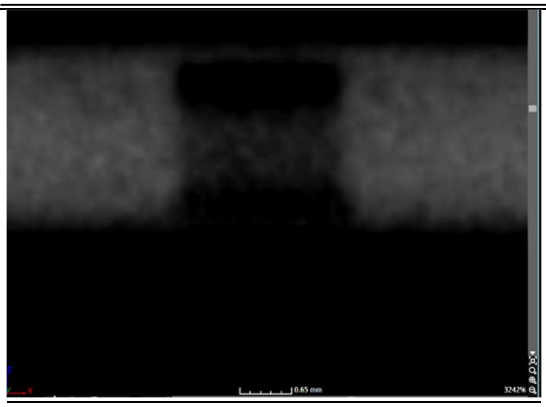

1S 0.096 ID	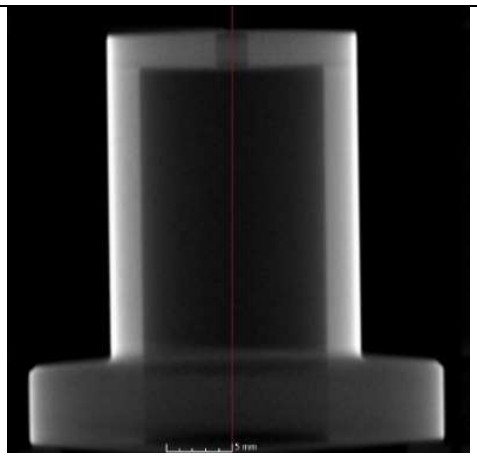	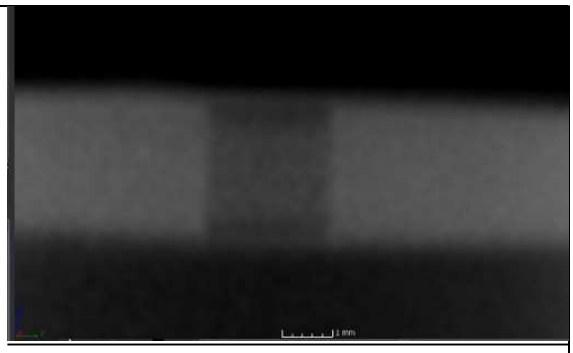
1S 0.11 ID	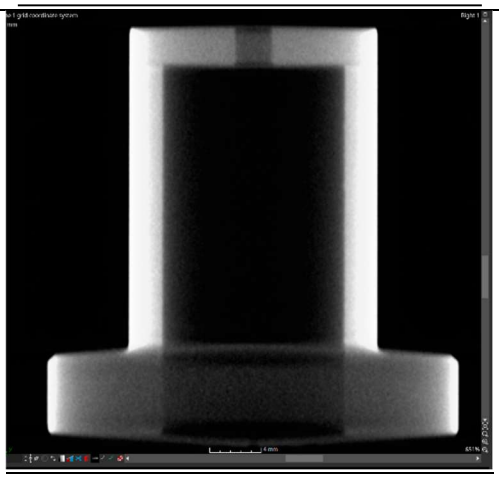	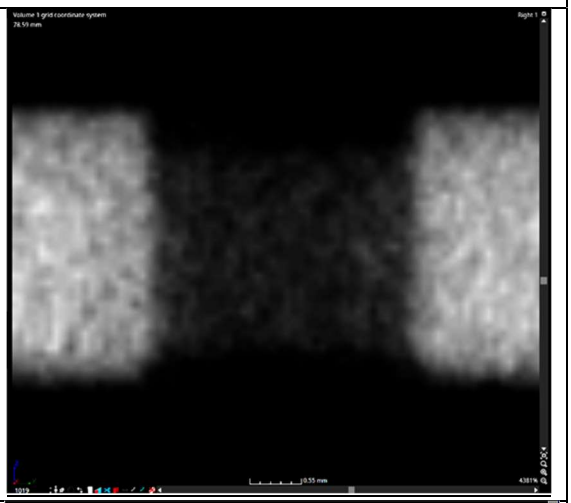
1S 0.125 ID	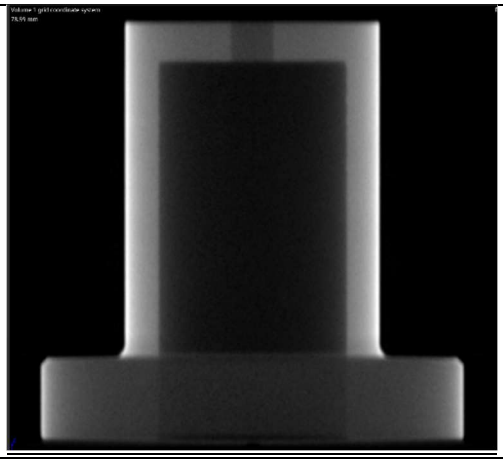	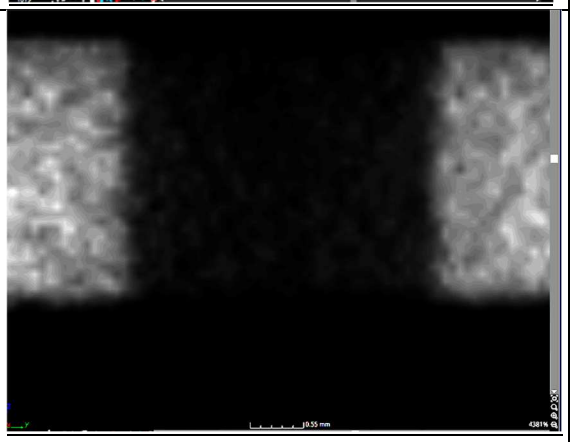

Appendix 5: Counterbore Study

This study focused on evaluating nozzles with a counterbore For this study 3 nozzles were tested with varying length to diameter ratio. The dimensions for these nozzles are shown below in Figure 59, with L*ID being the length adjusted for the different length ratios.

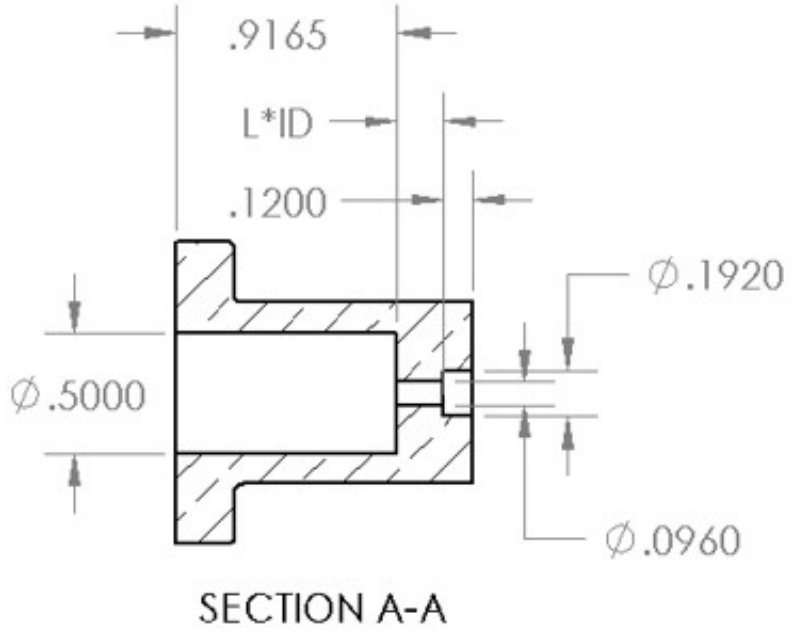

Figure 59: Counterbore Nozzle Diagram

These nozzles were manufactured using traditional means on a lathe rather than using EDM as was done for the other nozzles in this thesis. The nozzles were all tested over a range of pressure ratios from 0.2-0.68. Additionally, each PR was tested for the same 12 temperatures studied in the rest of this thesis. The results of this study can be found in the regime map below in Figure 60.

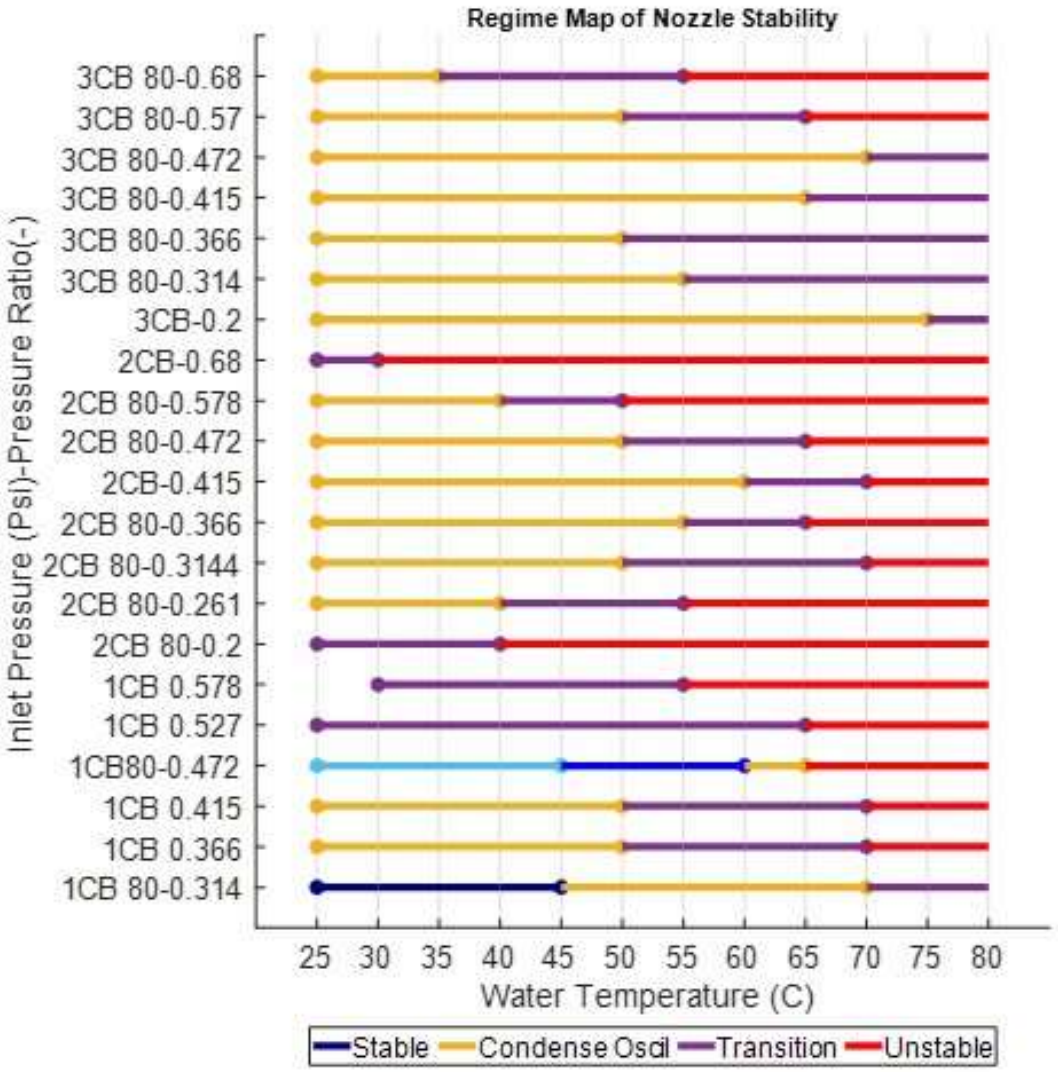

Figure 60: Regime Maps for Experimental Counterbore Results

Based on the results in Figure 60 it appears that adding a counterbore for the 1 and 2 LD nozzles negatively affects the performance whereas with the 3 LD nozzle it improves the performance at higher pressure ratios. These experimental results were compared to the simulated flow, where the geometry of each nozzle was based on the x ray scans shown in Table 5. The CFD results are shown in Figure 60. Additionally, the Mach number along the centerline is plotted below in Figure 62.

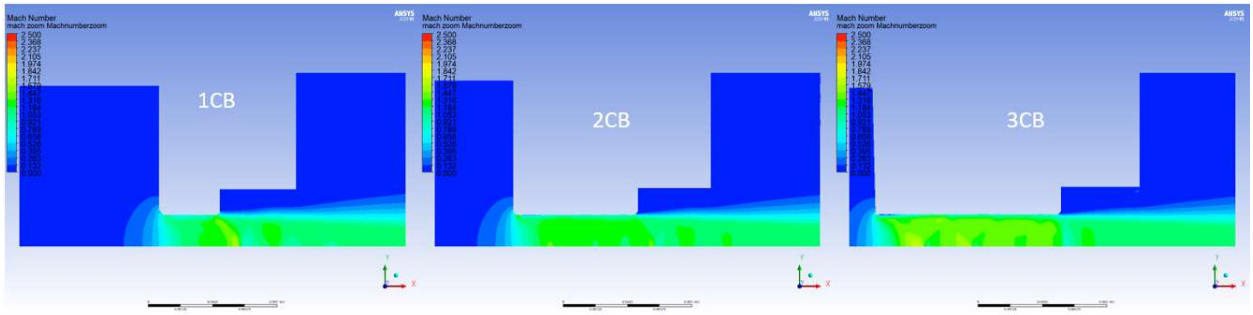

Figure 61: CFD Examples at 0.48 PR for each Nozzle

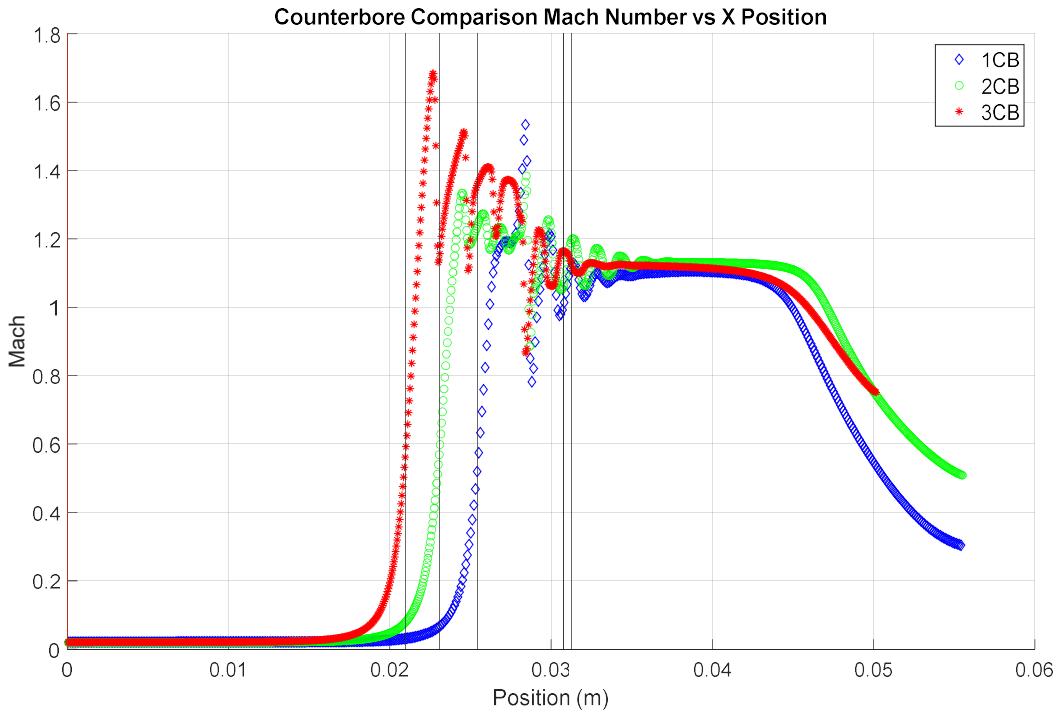

Figure 62: Mach Number vs X position for Counterbore nozzles at 0.48 PR

Based on the previous studies it would be expected that the shock would be furthest downstream for the most stable nozzle, but these two figures go against that notion suggesting that for the counterbore nozzles the model is not capable of predicting the flow. This could be for multiple reasons including the inability for the model in this thesis to account for pressure

changes due to the condensation front. It is believed that based on the videos taken that condensation does occur inside the counterbore section and would require a more advanced simulation to account for. Finally, all these nozzles were scanned using X ray and the geometry and the details of any defects are detailed below in Table 5.

Table 5: Xray Scans for Counterbore Nozzles

Nozzle	**Nozzle Features**	**Nozzle Scans**	**Zoomed In**
1CB	Slight chamfer at the inlet and first outlet (before counterbore)	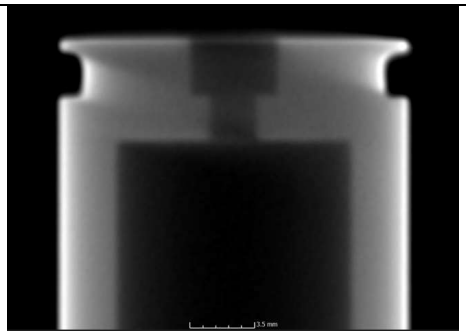	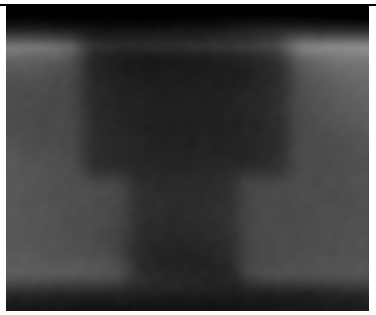
2CB	Slight chamfer at the inlet and first outlet (before counterbore)	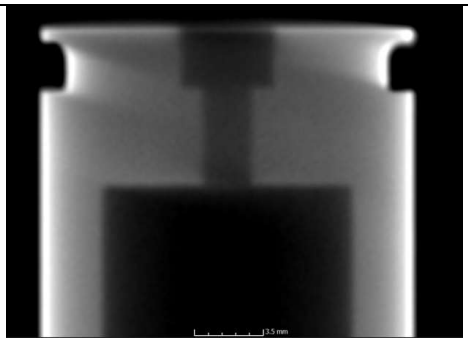	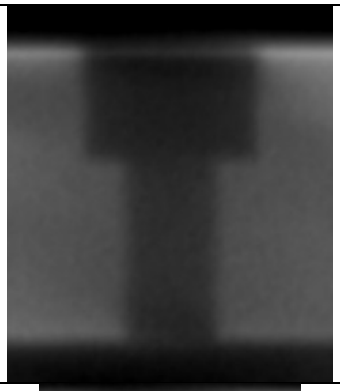
3CB	Slight chamfer at the inlet and first outlet (before counterbore)